Pontificia Universidad Javeriana de Bogotá en cotutela internacional con el Institut National Polytechnique de Toulouse- LAPLACE

Tesis Doctoral

Decentralized and Adaptive Selective Harmonic Elimination Strategies for the Control of Multilevel Converters

Estrategias Descentralizadas y Adaptativas para la Eliminación Selectiva de Armónicos en el Control de Convertidores Multinivel

Desarrollada por:

Miguel Emilio Vivert Del Pino

Directores:

- Rafael Díez, Ph.D., Pontificia Universidad Javeriana, Bogotá (Colombia)
- Diego Patiño, Ph.D., Pontificia Universidad Javeriana, Bogotá (Colombia)
- Marc Cousineau, Ph.D., Institut National Polytechnique de Toulouse-LAPLACE (Francia)

Co-director:

- Philippe Ladoux, Ph.D., Institut National Polytechnique de Toulouse-LAPLACE (Francia)

Jurados:

- Eric Labouré, Profesor GeePs - CentraleSupelec (Francia)
- Eduardo Mojica, Profesor Universidad Nacional de Colombia (Colombia)
- Margarita Narducci, Profesora Pontificia Universidad Javeriana (Colombia)
- Fredy Ruíz, Profesor Politecnico di Milano (Italia)

THÈSE

En vue de l'obtention du

DOCTORAT DE L'UNIVERSITÉ DE TOULOUSE

Délivré par l'Institut National Polytechnique de Toulouse

Cotutelle internationale : Université pontificale Javeriana

Présentée et soutenue par

Miguel VIVERT

Le 23 mars 2020

Élimination Sélective Adaptative des Harmoniques et Stratégies Décentralisées de Contrôle des Convertisseurs Multi-niveaux

Ecole doctorale : **GEET - Génie Electrique Electronique et Télécommunications : du système au nanosystème**

Spécialité : **Génie Electrique**

Unité de recherche :
LAPLACE - Laboratoire PLAsma et Conversion d'Énergie - CNRS-UPS-INPT

Thèse dirigée par
Marc COUSINEAU et Rafael Díez Medina

Jury

M. Eduardo MOJICA, Rapporteur
M. Eric LABOURÉ, Rapporteur
Mme Margarita NARDUCCI, Examinatrice
M. Fredy RUÍZ, Examinateur
M. Marc COUSINEAU, Directeur de thèse
M. Rafael DÍEZ, Directeur de thèse
M. Philippe LADOUX, Co-directeur de thèse
M. Diego PATIÑO, Co-directeur de thèse

Université Fédérale

Toulouse Midi-Pyrénées

Acknowledgement

Abstract

The research proposes some improvements in the efficiency, the robustness, the balancing of the cells and the fault tolerance ability of the Multicellular Converters. This work is divided into two stages. The fist stage proposes a control method for multicellular converters for balancing the cell variables, regulating the output variable and giving to the converter the ability to insert or remove cells during operation. The controller is composed of three sections, a balancing controller, a global regulator, and a bypass system. The balancing controller compares the cell variable with the cell variable of the neighbors and compensates for the error with a classical controller. The global regulator is a classical controller that regulates the output variable with the desired reference and the bypass system allows to skip a cell when the cell is not available. This control is implemented in the flying-capacitor multilevel converter and a cascaded full-bridge multilevel converter. In the flying-capacitor multilevel converter, the objective is to balances the cell voltages and to regulate the output current. The controller decouples the cell voltages and the output variable completely, allowing that disturbances in the cell variable do not disturb the global variable and vice vera. Simulation and experimental tests validate the performances of the theory of control method in this topology. In the cascaded full-bridge multilevel converter the objective is to balance the output voltage of the Full-Bridges and to regulate the output current of the converter. In this case, the controller unties the output variable from the cell variables, while the cell variable depends on the balancing controller that balances the cell variables and the global regulator that fixes the trajectory of the cell voltages. Results developed in simulation and experimentations validates the control method in the cascaded full-bridge multilevel converter, having good responses in all the tests.

The other contribution of the research corresponds to a control law for any symmetric Multilevel inverter modulated by a Selective Harmonic Elimination strategy. Typically, when a low frequency modulation strategy is implemented, there is no feedback for adjusting the switching angles, because of the complexity of the math process. The design of this controller is based on the obtention of a polynomial equation system and its conversion to its Groebner Basis of the system. To find the roots of the polynomial system, obtained by the Groebner basis conversion, an adaptation of the Newton Raphson method is implemented, emulating a virtual dynamical system. Furthermore, a PI controller is implemented to compensate for the error between the sensed harmonics and the harmonic reference when a disturbance is produced. This controller is validated in simulation and experimentation, disturbing some parameter, presenting good responses in all the tests

Resumen

Este trabajo propone mejoras en la eficiencia, robustez, balance de las celdas y tolerancia a fallas de los convertidores multicelulares. La investigación está dividida en dos secciones. La primera parte de este trabajo propone una ley de control para convertidores multicelulares que balancea un de las variables de las celdas, regula la variable de salida y brinda al convertidor la habilidad de insertar o remover células mientras el sistema está en funcionamiento. La estrategia de control está compuesta de tres partes, un control de balanceo de las variables celulares, un regulador de salida y un sistema de derivación. El control de balance compara una variable de una célula con la variable de las celdas vecinas y compensa el error con un control clásico. El regulador de salida es un control clásico que compara la variable de salida con una referencia y el sistema de derivación permite omitir la célula cuando esta no está disponible. Este control se implementa en dos convertidores, el convertidor de capacitores flotantes y convertidor de puentes H en cascada. En el convertidor de capacitores flotantes el objetivo es balancear los voltajes de las células y regular la corriente salida. El controlador desacopla completamente los voltajes de las células de la corriente de salida. Esto produce que una perturbación en los voltajes de las células no afecte la corriente de salida y viceversa. Simulaciones y pruebas experimentales validan la veracidad de la teoría en este convertidor. Acerca de la implementación del control en el convertidor de puentes H en cascada, el objetivo es balancear los voltajes de salida de los puentes H (variable de la célula) y regular la corriente de salida. En este caso el control desliga la corriente de salida de las variables celulares, mientras que las variables celulares, depende del control de balance, y del regulador de salida quien fija la trayectoria de las variables de las células. Los resultados desarrollados en simulación y experimentación validan la teoría, obteniendo buenos desempeños en todas las pruebas.

La segunda contribución de este trabajo es un control para inversores multinivel modulado mediante la eliminación selectiva de armónicas, que es una técnica de modulación a baja frecuencia. Normalmente técnicas de modulación a baja frecuencia no tiene realimentacion debido a la complejidad matemática para ajustar los ángulos de conmutación en tiempo real. El diseño de este controlador se basa en la obtención de un modelo polinómico y su conversión en sus bases de Groebner. Para obtener las soluciones de este sistema convertido a las bases de Groebner, una variante del método de Newton Raphson es propuesta, convirtiendo este sistema estático en un sistema dinámico virtual. Además, un control PI es implementado para compensar las variaciones entre las armónicas de referencias y las armónicas sensadas. Este control es validado con pruebas en simulación y experimentación, insertando carga al sistema y perturbando los voltajes de entrada, obteniendo buen desempeño en todas las pruebas.

Résumé

La recherche propose quelques améliorations de l'efficacité, de la robustesse, de l'équilibrage des cellules et de la capacité de tolérance aux pannes des convertisseurs multicellulaires. Ce travail est divisé en deux étapes. La première étape propose une méthode de contrôle des convertisseurs multicellulaires pour équilibrer les variables de cellule, réguler la variable de sortie et donner au convertisseur la possibilité d'insérer ou de retirer des cellules pendant le fonctionnement. Le contrôleur est composé de trois sections, un contrôleur d'équilibrage, un régulateur global et un système de dérivation. Le contrôleur d'équilibrage compare la variable de cellule avec la variable de cellule des voisins et compense l'erreur avec un contrôleur classique. Le régulateur global est un contrôleur classique qui régule la variable de sortie avec la référence souhaitée, et le système de bypass permet de sauter une cellule lorsque la cellule n'est pas disponible. Cette commande est implémentée dans le convertisseur multiniveau à condensateur volant et un convertisseur multiniveau en pont complet en cascade. Dans le convertisseur multiniveau à condensateur volant, l'objectif est d'équilibrer les tensions des cellules et de réguler le courant de sortie. Le contrôleur dissocie complètement les tensions de cellule et la variable de sortie, ce qui permet que les perturbations dans la variable de cellule ne perturbent pas la variable globale et vice-versa. Des tests de simulation et expérimentaux valident les performances de la théorie de la méthode de contrôle dans cette topologie. Dans le convertisseur multiniveau à pont complet en cascade, l'objectif est d'équilibrer la tension de sortie des ponts complets et de réguler le courant de sortie du convertisseur. Dans ce cas, le contrôleur délie la variable de sortie des variables de cellule. En revanche, la variable de cellule dépend du contrôleur d'équilibrage qui équilibre les variables de cellule et du régulateur global qui fixe la trajectoire des tensions de cellule. Les résultats développés en simulation et expérimentations valident la méthode de contrôle dans le convertisseur multiniveau à pont complet en cascade, ayant de bonnes réponses dans tous les tests. L'autre contribution de la recherche correspond à une loi de contrôle pour tout onduleur multiniveau symétrique modulé par une stratégie d'élimination harmonique sélective. En règle générale, lorsqu'une stratégie de modulation à basse fréquence est mise en œuvre, il n'y a pas de rétroaction pour ajuster les angles de commutation en raison de la complexité du processus mathématique. La conception de ce contrôleur est basée sur l'obtention d'un système d'équations polynomiales et sa conversion en sa base Groebner du système. Pour trouver les racines du système polynomial, obtenues par la conversion de base Groebner, une adaptation de la méthode Newton Raphson est implémentée, émulant un système dynamique virtuel. De plus, un contrôleur PI est implémenté pour compenser l'erreur entre les harmoniques détectées et la référence harmonique lorsqu'une perturbation est produite. Ce contrôleur est validé en simulation et expérimentation, perturbant certains paramètres, présentant de bonnes réponses dans tous les tests

Contents

7

List of Figures

List of Tables

Chapter 1

Introduction

In the last decades, the power electronics have been used in several applications, such as energy conversion and transmission, electrical traction and storage systems. In all of these cases, the power converters have a key role, converting the energy of the source into a suitable one for the load. There are many types of power converters according to the application as: step up, step down, DC/AC or AC/DC converters.

Power converters consist mainly of passive elements, such as inductors and capacitors, and a set of switching devices such as MOSFETs, IGBTs, GTOs, Diodes, SCRs [1, 2]. For low and medium voltage applications, MOSFETs and IGBTs are relatively fast and offer the advantages of controlling the turning ON and turning OFF of devices. While SCRs can be used for high voltage and high power, with the disadvantage that turns them off might be complicated. Concerning to GTOs, they are straightforward to turn ON and OFF. In addition, they support high voltage and high power. However, both GTOs and SCRs have a relatively slow switching time of around hundreds of microseconds, making them inappropriate for high-frequency applications.

Another solution for high power/voltage management is the use of Multi-Cellular Converters (MCC). The idea of MCCs is to *"divide and rule"*. These converters consist of an arrangement of several cells connected in parallel, in series or in cascaded, which allows distributing the voltage or current at the input or the output. There are many types of MCCs, such as the Flying Capacitor Multilevel Converter (FCMC), where the input voltage is distributed among the cell voltages, Cascaded Full Bridge Multilevel Converter (CFBMC), where the total output voltage is distributed in the output voltage of each Full Bridge (FB), Multiphase Buck Converter where the output current is the sum of the leg currents. In all these cases the energy is distributed among the cells, allowing the use of low or medium power devices for high power applications. This fact is a great advantage because normally low power devices are faster and more efficient than high power ones. High current MOSFETs are usually slower than low current MOSFETs, producing high switching losses. While high voltage MOSFETs have higher internal resistance than low voltage MOSFETs, increasing the conductive losses. Therefore, MCCs allow managing high power conversion with low power and fast switching devices. Besides, over the years, the size of Multi-Cellular converters has been significantly reduced due to the reduction of input/output ripples thanks to increase of apparent frequency, reduction of losses leading to shrink of cooling systems, increasing power density.

Another feature of the multicellular converters is that it is possible to implement a high-frequency modulation strategy that increases the output frequency, either for DC/AC or DC/DC converters, reducing the size of the output filter. Furthermore for

DC/AC converters, it is possible to implement multicellular converters using either high or low-frequency modulation strategies. Low-frequency modulation strategies allow reducing the THD or eliminating the most relevant harmonics.

MCCs offer many advantages, however, there are a lot of challenges to be solved for these topologies. One of them is the ability to balance one variable of the cells according to the application. In FCMC it is very useful that the cell voltages are equalized. This produces that the supplied power is distributed equally in all the cells. Furthermore, it produces a suitable ripple output voltage [3–5]. In the case of Multiphase Buck, balancing the leg current produces a suitable distribution of the output current of the system [6]. For the case of CFBMC, it is possible to balance the output voltages of each FB for maintaining equalized the power delivered by each FB [7–10], or if the sources are batteries, to balance the input current of each FB to maintain well balanced the charging or discharging of the batteries. Furthermore, it is possible to balance the State Of Charge (SOC) of the batteries. All these cell-variables balancing strategies can turn very complicated if the number of cells increases significantly.

Another challenge for Multicellular converters is the ability to change the number of cells during operation. This challenge is addressed because the modular structure of these converters provides redundancy and allows for the design of a system that reconfigures the number of cells during operation. This means that if one or more cells fail, these cells can be removed while the system is in operation. Besides, with this reconfiguration capability, a cell can be inserted during operation to increase the power capability or leads to improve the global efficiency of the system. In [3, 8, 11] the proposed controllers allow insertion and removal cells during operation and present interesting results.

Another challenge is the ability to control a large number of variables, because if the number of cells increases, the number of variables to be controlled also increases. Therefore, the control method to keep stable the system can be very complex in some cases. In [3, 8, 11] the theory indicates that these controllers can be implemented in a large number of cells.

The last challenge that is taken into account in this work is the implementation of a control method for the low frequency modulation strategy of multilevel inverters (MIs) that regulates the output voltage if disturbances occur at the sources. The main advantage of low-frequency modulation strategies is that the efficiency of the inverter increases significantly. These strategies may have different objectives such as minimizing THD [12, 13] or eliminating some harmonics [14, 15] by switching a finite number of times per period. The main problem with these strategies is the complexity of finding the switching angles. Therefore, these angles are often obtained off-line. However, if there is a disturbance at the input sources, the switching angles must be recalculated. These calculations can be highly complex to develop in real-time and may take excessive processing time.

This work proposes a first solution for balancing the cell variables and regulating an output variable. Furthermore, the proposed solution has the ability to insert or remove cells during operation. This is carried out by a decentralized control method for a wide

range of MCCs able to regulate the output of the MCC, to balance any number of cell variables and to implement a reconfiguration system for changing the number of cells.

Furthermore, this work also proposes a second solution for controlling the switching angles in a low-frequency modulation strategy that adjusts the angles when a disturbance in the input sources is produced.

This work is presented as follows: Chapter two of this manuscript presents an overview of the most popular topologies of the multicellular converters and the most used modulation techniques for these converters. Furthermore, the chapter introduces the most used control techniques to regulate the output of the MCCs, balance the cell variables of different topologies and describes some reconfiguration methods that allow a fault tolerance ability in some converters. Additionally, the chapter explains the most relevant low-frequency modulation strategies and some solving methods for finding the switching angles. Finally, some control techniques for low-frequency modulation strategy is presented, showing their advantages and drawbacks.

In the third chapter a decentralized control method for several MCC topologies is proposed which regulates the output, balances the cell variables and gives to the converter a reconfiguration ability, being able to insert or remove cells during operation. This control method is validated, using two different topologies, an FCMC and a CFBMC. Simulation and experimental results in both converters are also presented, showing good performance in all the cases.

The fourth chapter presents an in-depth study of the behavior of the harmonics, according to the switching angles and based on this study a control method for adjusting in real-time the switching angles when the input sources change. This theory is validated in simulation and experimentation, presenting good performance in all the tests. Finally, the fifth chapter presents the conclusion of all the research and also the future works.

1.1   Research proposal

The introduction shows that MCCs present many advantages due to its modular structure, such as the capability to manage high voltage or high power. However, considering its complexity, there are performance characteristics that are not completely developed yet, as the balancing of the cell variables, fault tolerance and the capability of insertion or removing cells during the operation. Furthermore, also, due to the modular structure, some issues can be minimized as the power losses in the cells, that for Multilevel Inverter can be the implementation of a low-frequency modulation strategy. However, the complexity of the solving process makes difficult to find the solution, when the parameters of the Inverter change. Based on these performance characteristics and issues there are two proposals in this research:

The first one is the design of a decentralized controller for a wide range of Multicellular Converter that balances the same variable of each cell and controls the output variable, with the capability to insert or remove a cell during the operation, auto-

balancing the system, improving the robustness and implementing a fault tolerance system. The results of it, are validated by simulation and experimentation in two different MCCs, balancing different cell variables, inserting and removing cells, and disturbing parameters.

The second proposal is addressed to the efficiency of a Multilevel Inverter, using low-frequency modulation strategies, and it is the design of a controller for Selective Harmonic Elimination (SHE) strategy, adjusting the angles when a disturbance is produced. The theory of the control is generalized for any symmetric Multilevel Inverter of N positives levels and it will be validated by simulation and experimentation in one symmetric Multilevel Inverter, disturbing the input voltage and changing the load.

1.2   General Objective

The main objective of this research is to improve the performance, the efficiency of Multicellular Converters, taking advantage of its modular structure, making the system more flexible and tolerable to faults, increasing the robustness and balancing the power on each cell according to the application.

1.3   Specific Objectives

Concerning the control strategies developed and proposed in the thesis, the specific objectives are:

- To propose a generalized structure of a decentralized controller to be implemented in a wide range of Multi-Cell Converter, balancing the same variable of each cell, controlling a specific output variable and having the ability to insert or remove cells.

- To design similar decentralized controllers for different applications in two Multi-Cell Converters based on the proposed generalized structure.

- To design a control law for Selective Harmonic Elimination Modulation Strategy implemented in any Symmetric Multilevel Inverter, able to compensates the disturbances produced by the input voltages and load changes, recalculating the switching angles in real-time.

- To validate the designed controllers by simulation and experimentation, disturbing parameters.

Chapter 2

Literature Review

This chapter introduces and presents the topologies of some MCCs, in which the proposed control strategies will be implemented. Furthermore, this chapter presents also the most known modulation techniques used in these converters. Finally, an overview of previous works developed for controlling the MCCs, for high/low frequency modulation strategies is presented.

2.1 Topologies of Multicellular Converters

Multicellular converters are made of several cells, each cell is formed of switching devices, passive elements such as inductors and capacitors, and in some cases local power supplies. There are several topologies of MCCs, as Fig. 2.1 shows.
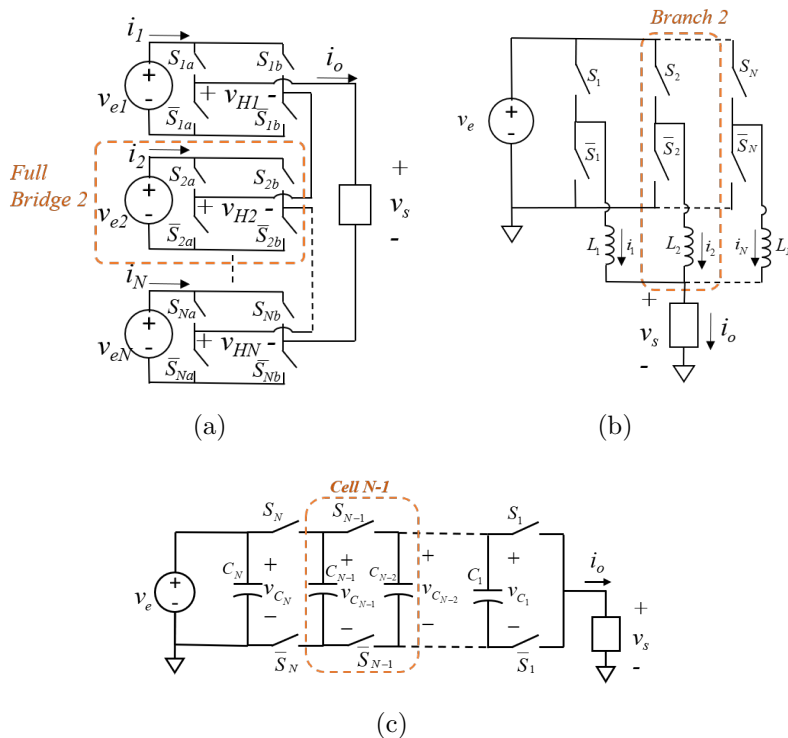
Figure 2.1: Different Topologies of Multilevel Converters. (a) Cascaded Full Bridge Multilevel Converter, (b) Multiphase Buck Converter, (c) Flying-Capacitor Multilevel Converter

Fig. 2.1 shows the three topologies that are detailed in this work that are: Multiphase buck [6, 11, 16], Flying-Capacitor Multilevel Converter [3–5, 17, 18], and Cascaded Full Bridge Multilevel Converter [19–22].

2.1.1 Cascaded Full Bridge Multilevel Converter

Fig. 2.1(a) shows the schematic of a Cascaded Full Bridge Multilevel Converter, where each cell is a Full Bridge (FB), and is composed of two legs of switching devices fed by an input voltage source v_{ek}. $S_{k\nu}$ and $\overline{S_{k\nu}}$ are the switches, where $\overline{S_{k\nu}}$ receives the opposite control signal of $S_{k\nu}$, and ν represents the branch, a and b for the left and right leg respectively. In some cases, there is an input LC filter between the input source and the FB, for smoothing the input current.

Furthermore, it can be observed in Fig. 2.1(a) that the cells are connected in serial, in which v_s is the sum of all the output voltages of the FBs, v_{Hk}. These topologies are widely useful to generate high output voltage if there are several low voltage sources such as solar panels or batteries. Based on Fig. 2.1(a), table 2.1 shows the state of each FB (v_{Hk}) according to the position of the switches.

Table 2.1: v_{ek} vs S_{ka}, S_{kb}

S_{ka}	S_{kb}	v_{Hk}
0	0	0
0	1	$-v_{ek}$
1	0	v_{ek}
1	1	0

According to Table 2.1, if one FB is present, 3 voltage levels are available. $(-v_{ek}, \ 0, \ v_{ek})$, producing positive and negative voltages. For that reason this topology is mostly used for DC/AC. Fig. 2.2 shows v_{Hk} according to the position of S_{ka} and S_{kb}.
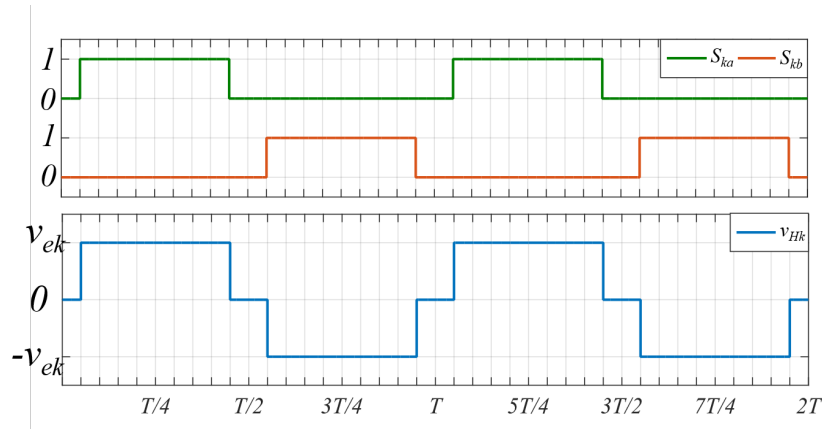
Figure 2.2: Waveform of the output of a FB converter

CFBMC can be classified according to the ratio between the input sources in [23]: Cascaded Equal Multilevel Inverter (CEMI), where $v_{e1} = v_{e2} = \cdots = v_{eN} = v_e$ [20, 22], producing voltage from $-Nv_e$ to Nv_e passing by 0, meaning $2N + 1$ levels, Unary Hybrid Multilevel Inverter (UHMI), where $v_{ek} = kv_e$, producing a maximum voltage of $\frac{N(N+1)}{2}v_e$ and generating $(N+1)^2 - N$ levels, Binary Multilevel Inverter (BHMI) where $v_{ek} = 2^{k-1}v_e$ [24, 25], having a maximum voltage level of $(2^N - 1)v_e$ producing $2^{N+1} - 1$ levels, and Trinary Hybrid Multilevel Inverter (THMI), where $v_{ek} = 3^{k-1}v_e$ with a $v_{s_{max}} = \frac{1}{2}(3^N - 1)v_e$ and 3^N levels [26–29]. It can be inferred that one advantage of having different input voltages on the input sources is to produce more levels per FB [23]. THMI is the topology that produces the most levels, l, per number of FBs, N, as [29, 30] demonstrates. References [26, 27, 29] explain in more detail the principle of THMI. Knowing that each FB can generate 3 levels, Fig. 2.3(a) shows the waveform of the output voltage of a CEMI with 2 FBs and Fig. 2.3(b) shows the waveform of the output voltage of a THMI with 2 FBs.
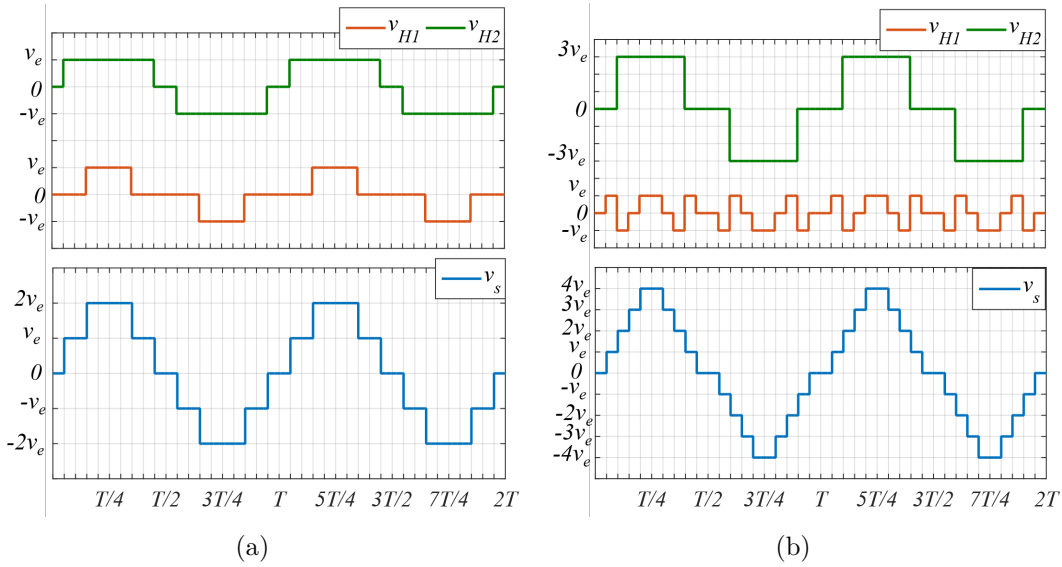
Figure 2.3: Output waveform of Cascadeds Full Bridge Multilevel Inverters (a) Cascaded Equal Multilevel Inverter, (b) Trinary Hybrid Multilevel Inverter

Fig. 2.3 shows the 5 voltage levels in the CEMI and the 9 voltage levels in THMI, validating that THMI presents more levels per FB than CEMI. However, THMI is more complex to modulate than CEMI. In the following section, some modulation techniques are explained, for these two topologies. Cascaded Equal Multilevel Inverter is the most used CFBMCs, because of its straightforwardness to modulate and its availability to balance the power in each FB without affecting the value of the step voltage.

2.1.2 Flying-Capacitor Multilevel Converter

According to Fig. 2.1(c), the Flying-Capacitor Multilevel Converter is made of cells that have a pair of switching devices and a capacitor [3–5, 17, 18]. The cells are connected in cascade, meaning that the input of the $k + 1^{th}$ cell supplies the kth cell and the input sources, v_e, feeds the Nth cell, while the output of the first cell is shorted. It is possible to define a cell-voltage as the difference of the adjacent capacitor voltages $v_k = v_{Ck} - v_{Ck-1}$, leading to the sum of all the cell-voltages is equal to the input voltage. If S_k is OFF-state, the voltage across the switch is v_k, otherwise 0. This topology is commonly used when there are high input voltages and low/medium output voltage such as train applications [4, 5]. In this topology, the kth capacitor is charged and discharged according to the position of S_k and S_{k+1}. Table 2.2 shows the behavior of the current capacitor according to the position of its adjacent switching devices

Table 2.2: Current through the kth capacitor

S_{k+1}	S_k	i_{Ck}
0	0	0
0	1	$-i_o$
1	0	i_o
1	1	0

Notice that when the switch S_k is ON, the capacitor is discharged and while S_{k+1} is ON, C_k is charged. Table 2.3 shows the behavior of the output voltage v_s of the FCMC when N=3.

Table 2.3: v_o vs S_1, S_2, S_3

S_3	S_2	S_1	v_o as v_{Ck}	v_o as v_k
0	0	0	0	0
0	0	1	v_{C1}	v_1
0	1	0	$v_{C2} - v_{C1}$	v_2
0	1	1	v_{C2}	$v_2 + v_1$
1	0	0	$v_{C3} - v_{C2}$	v_3
1	0	1	$v_{C3} - v_{C2} + v_{C1}$	$v_3 + v_1$
1	1	0	$v_{C3} - v_{C1}$	$v_3 + v_2$
1	1	1	v_{C3}	$v_3 + v_2 + v_1$

Fig. 2.4 shows the output voltage v_s when the switches are closed 50 % of the period T_s and the pulse of the switch S_k is delayed T_s/N from the switch S_{k-1}.
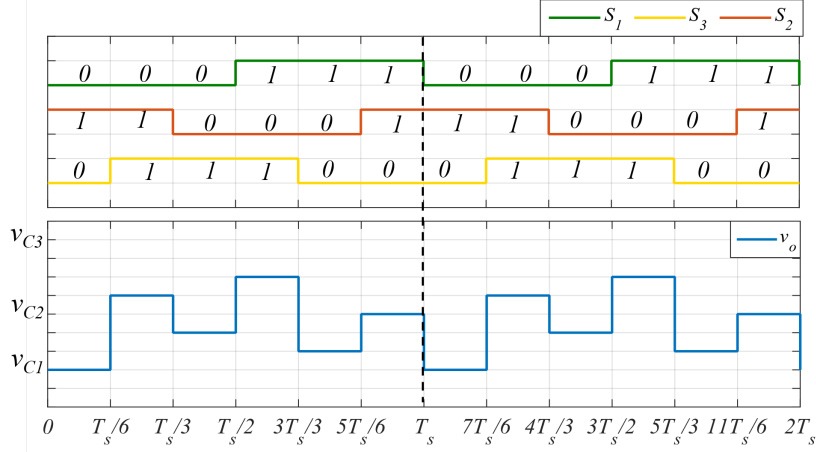
Figure 2.4: Waveform of v_o and S_1, S_2, S_3

Notice that the apparent output frequency is equal to the switching frequency multiplied by the number of cells (in this case three). However, each step voltage is different. Furthermore, according to Fig. 2.4, S_3 has to sustain a higher voltage than S_2 and S_2 sustain a higher voltage than S_1. These effects can be minimized if $v_{Ck} = \dfrac{kv_e}{N}$. In that case, all the switches sustain the same voltage, $v_k = v_e/N$. Additionally, the step voltages of v_s are identical, v_e/N. Therefore, it is possible to conclude that balancing the cell-voltages two advantages are obtained: The switches have to sustain the same voltage and the ripple of the output voltage is minimized. In the next sections, a summarize of the modulation strategies for obtaining this balancing effect is developed and the appropriate controllers to balance the cell-voltages are detailed.

2.1.3 Multiphase Buck Converter

According to Fig. 2.1(b), a Multiphase Buck is composed of N half-FBs connected in parallel, whose the switching-node is connected to an inductor. The inductors of the legs are connected to a load, producing that the sum of the leg currents, i_k, is equal to the output current i_o. This topology is very useful when it is necessary to produce high output current with low or medium input voltage [6, 11, 16]. According to Fig. 2.1(b) if one leg is analyzed, it is a buck converter. Hence, if v_s is constant:

Table 2.4: k^{th} current vs the S_k

S_k	$\dfrac{di_k}{dt}$
1	$(v_e - v_s)\dfrac{1}{L}$
0	$-v_s\dfrac{1}{L}$

According to table 2.4, Fig. 2.5 shows the waveform of i_k if the current at the end of the period is the same as the beginning of the period.
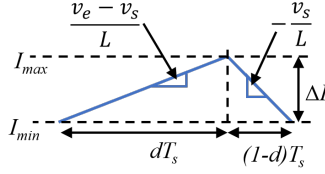
Figure 2.5: Waveform of the leg current in one period of switching

where T_s is the switching period and d is the duty-cycle (percentage of the period in which S_k is in ON-state). According to Fig. 2.5, the peak-to-peak amplitude of the current waveform in Continue-Current-Mode of the current is:

$$\Delta I = dT_s \frac{v_e - v_s}{L}$$
$$-\Delta I = (1 - d)T_s \frac{v_s}{L}$$

(2.1)

Obtaining that $d = \dfrac{v_s}{v_e}$ for remaining the same value of the current at the end and the beginning of the period. Remaining that the output current i_o is the sum of all the leg currents. Fig. 2.6 shows the waveform of the leg current and the output current of the system, where $N = 3$ and the switching time of S_2 and S_3 are delayed $T_s/3$ and $2T_s/3$ from the switching time of S_1 respectively. In [6, 16] develop a Multiphase Buck Converter for different applications. Furthermore, in chapter 3 a brief explanation of the model of a Multiphase Buck is introduced. The next section explains some modulation strategies for all the topologies described in this section.
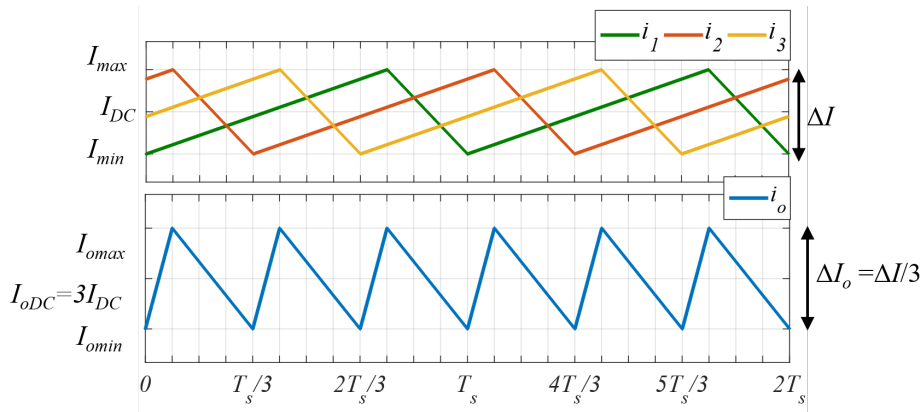
Figure 2.6: Leg currents and output current of a Multiphase Buck Converter with 3 legs

2.2 Modulation Strategies for MCCs

There exist many modulation strategies for Multicellular Converters [14, 27, 31, 32], especially for Multilevel Inverters. This section explains the most relevant strategies and the ones used in this research. Modulation strategies can be classified in low and high-frequency techniques. Low-frequency modulation strategies are commonly used for DC/AC converters, while high-frequency strategies are used for DC/DC, DC/AC of AC/DC converters.

2.2.1 High-frequency Modulation Strategies

One of the most used high-frequency modulation strategies for power converters is the Pulse Width Modulation (PWM), which is used for 2 levels DC/DC converters. Based on this technique, other modulation techniques are designed for DC/ACs and MCCs. PWM modulation has as output a binary signal, v_{pwm}, and has as inputs a triangular or sawtooth signal, v_{tri}, called the carrier, and a DC value, v_m, where:

$$v_{pwm} = \begin{cases} 0 & ; v_{tri} > v_m \\ 1 & ; v_{tri} \geq v_m \end{cases} \tag{2.2}$$

Fig. 2.7 shows the waveform of v_{pwm}, v_m and v_{tri}:
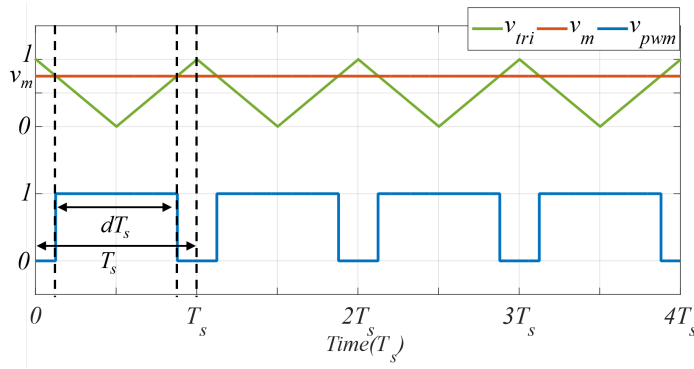
Figure 2.7:   Waveform of v_{pwm}, v_m, v_{tri}, using PWM

where T_s is the period and d is the percentage of the period which v_{pwm} is equal to 1. d is also called the duty cycle, because it corresponds to the percentage of the period in which the switching device is ON.

Based on PWM techniques, some modulation methods for different application are proposed. One of them is the Sinusoidal PWM (SPWM) [1, 32], that consists in a PWM where v_m is a sinusoidal wave. SPWM can be bipolar or unipolar SPWM. Bipolar SPWM [1, 2] is a strategy in which according to Fig. 2.1(a), S_{ka} is modulated by d_{ka} and $S_{kb} = \overline{S_{ka}}$. Producing only two available levels, v_{ek} and $-v_{ek}$, with no level

in 0 V. Fig 2.8 shows v_{Hk}, employing bipolar SPWM with $v_m = \dfrac{A}{2}\sin(\omega t) + \dfrac{1}{2}$, where A=0.8, $\omega = \dfrac{2\pi}{T}$ and T is the period of v_m.
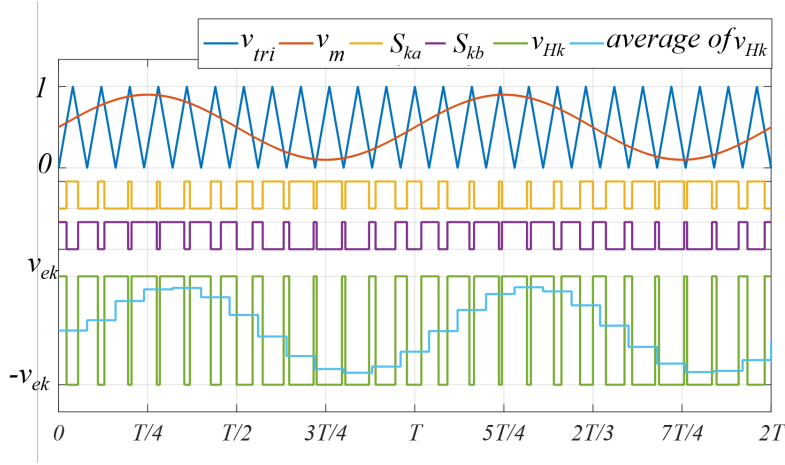
Figure 2.8: Bipolar SPWM

Notice that the waveform generated by the average of v_{Hk} in one switching period T_s is close to a sine wave. Furthermore, as Fig. 2.8 shows, v_{Hk} presents only two values, $-v_{ek}$, v_{ek}, it generates that the RMS value of v_{Hk} is v_e and the fundamental component, v_1, is approximately Av_{ek}. Hence, the Total Harmonic Distortion of this modulation is:

$$THD = \sqrt{\left(\frac{v_{RMS}}{v_{1_{RMS}}}\right)^2 - 1}$$

$$THD = \sqrt{\left(\frac{v_{ek}}{\frac{Av_{ek}}{\sqrt{2}}}\right)^2 - 1} \tag{2.3}$$

$$THD = \sqrt{\frac{2}{A^2} - 1}$$

$$THD = 145.77\%$$

Eq. (2.3) shows that bipolar modulation presents a high THD. Furthermore, (2.3) allows inferring that bipolar modulation has always a THD higher than 100 %, excepting overmodulation cases ($|v_m - 0.5| > 0.5$). For validating this statement, Fig. 2.9 presents the Fourier analysis of v_{Hk}, using bipolar SPWM
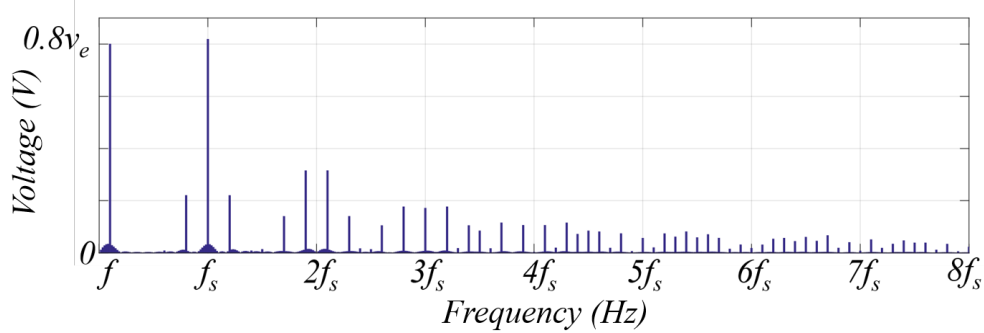
Figure 2.9: Fourier analysis of v_{Hk} using bipolar SPWM

Where $f_s = \dfrac{1}{T_s}$ and $f = \dfrac{1}{T}$. Fourier analysis shows that the component at f_s is higher than the fundamental component at f. For that reason the THD is higher than the 100 %.

Unipolar SPWM techique is a PWM strategy where the duty cycle of S_{ka} is $d_{ka} = v_m$ and the duty cycle of S_{kb} is $d_{kb} = 1 - d_{ka}$. Fig. 2.10 shows the waveform of v_s, using this modulation with the same v_m used in bipolar modulation.
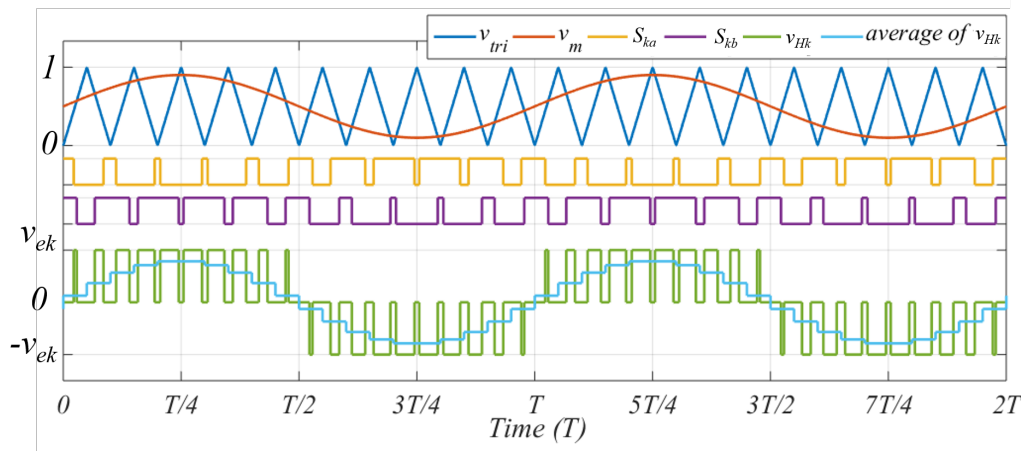
Figure 2.10: Unipolar SPWM

Notice that the frequency of v_{Hk} is twice of the carriers and there are 3 levels ($\pm v_{ek}$ and 0). The THD of v_{Hk} for unipolar SPWM is 77.37%. Fig. 2.11 shows the Fourier analysis of unipolar SPWM. Notice that the Fourier components corresponding to the odd multiples of f_s are removed, validating the considerable reduction of the THD.
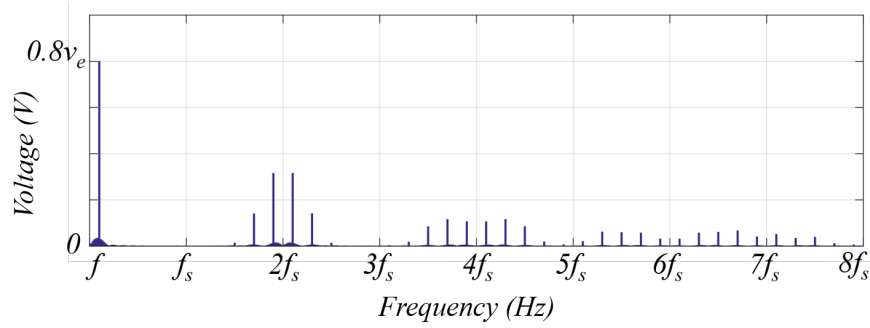
Figure 2.11: Fourier Analysis of unipolar SPWM

Unipolar SPWM Strategy is the most used modulation strategy for inverters using only one FB and it is the base for some modulation strategies of multilevel inverters.

There are many high-frequency modulation strategies for MCCs, the most popular are the multicarrier PWM modulation strategies, where each cell has its carrier. The most known multicarrier PWMs are Level-Shifted Multicarrier PWM (LSPWM) and Phase-Shifted Multicarrier PWM (PSPWM). In LSPWM the carrier of the kth cell is shifted one level upper of the previous cell carrier. Fig. 2.12 shows a LSPWM applied to a FCMC of 3 cells where the capacitor voltages are well balanced, meaning that $v_k = \dfrac{v_e}{N}$.
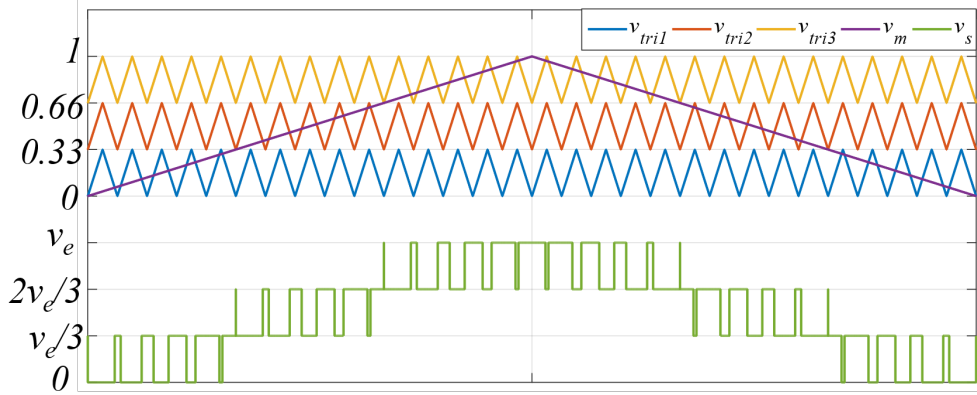
Figure 2.12: Level-shifted multicarrier PWM applied for a FCMC

Notice that the switching frequency of v_s is the same as the carrier one, with v_s switching between two adjacent levels. This fact reduces the Fourier component at f_s. For the case of symmetric CFBMC with the same input voltages, each leg of the FBs has his carrier. Fig. 2.13 shows the carriers of the switching devices and the output voltage v_s with 3 FBs.
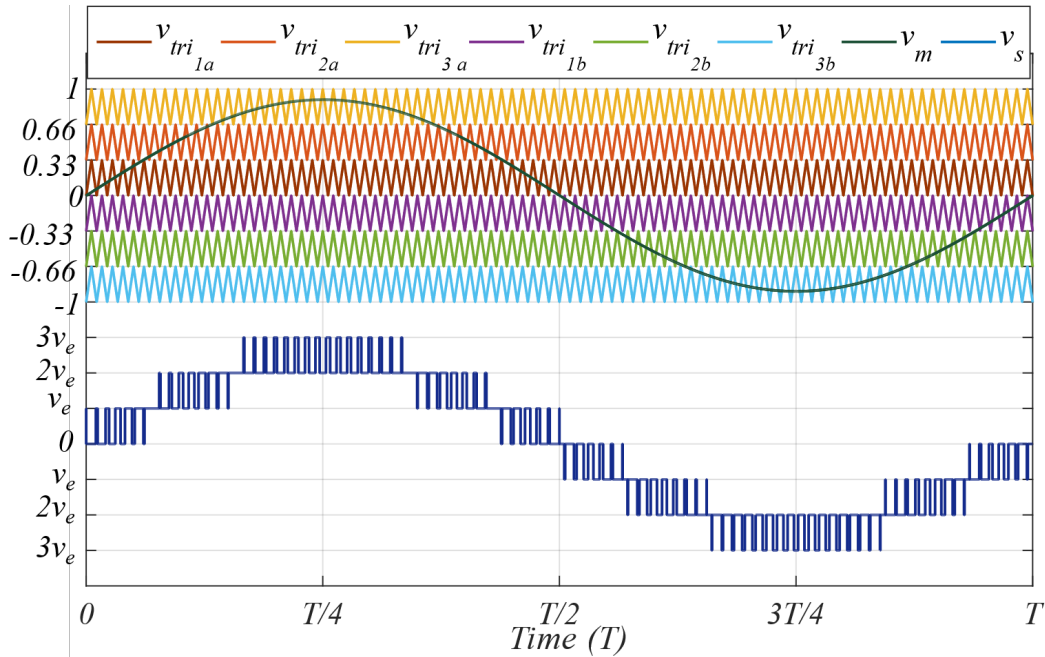
Figure 2.13: Level-shifted multicarrier PWM for a Inverter

Notice that the switching frequency of v_s is the same as the frequency of the carriers, with the advantage that the switching steps of v_s is only one voltage level. To highlight the benefits of this modulation, Fig. 2.14 shows the Fourier analysis of v_s with this modulation strategy.
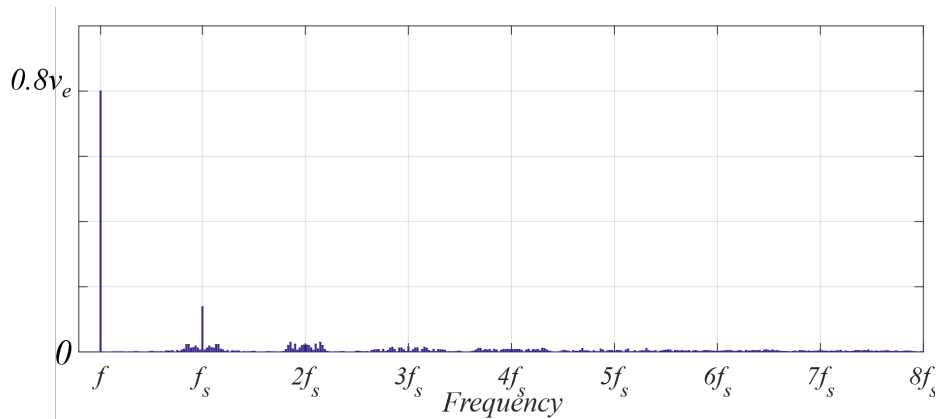
Figure 2.14: Fourier Analysis of a Level-shifted Multilevel PWM applied to a Inverter

Notice that the component at f_s is reduced considerably, compared to the bipolar modulation. Additionally, the THD of v_s is 24.34 %. This fact validates the benefits of this strategy. There are some improved modulations of this strategy as Phase Opposition Disposition (POD) or Alternative Phase Opposition Disposition (APOD) [33, 34].

The other Multicarrier Modulation Strategy is Phase-shifted Multicarrier Modulation Strategies [22, 35], where each cell is modulated by PWM and the carrier of the kth cell is shifted in phase $\phi = 360\left(\frac{k-1}{N}\right)^{\circ}$. Fig. 2.15 shows the waveform of v_s of a FCMC of 3 cells using this strategy when the cells are well balanced.
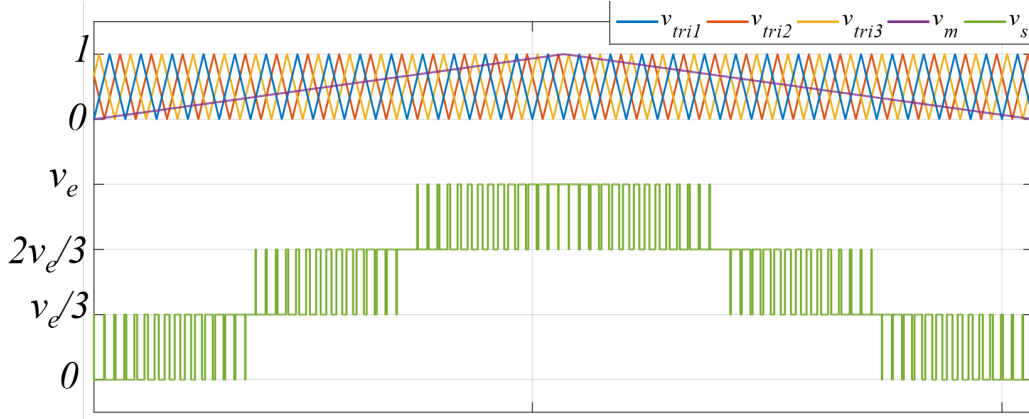
Figure 2.15: v_s of a FCMC modulated by Phase-shifted Multicarrier PWM

Notice that the frequency of v_s is increased three times respect to the frequency of the carrier, it is mean that the harmonic components are shifted to higher frequencies, allowing a reduction of the inductance and the capacitance of the output filter. For the case of Multilevel Inverters, to modulate with this strategy, $v_{tri_{(k+1)}}$ is shifted $\phi = 180\left(\frac{k-1}{N}\right)^{\circ}$ of v_{tri_k}. Fig. 2.16 shows the results produced by a unipolar phase-shifted multicarrier SPWM.
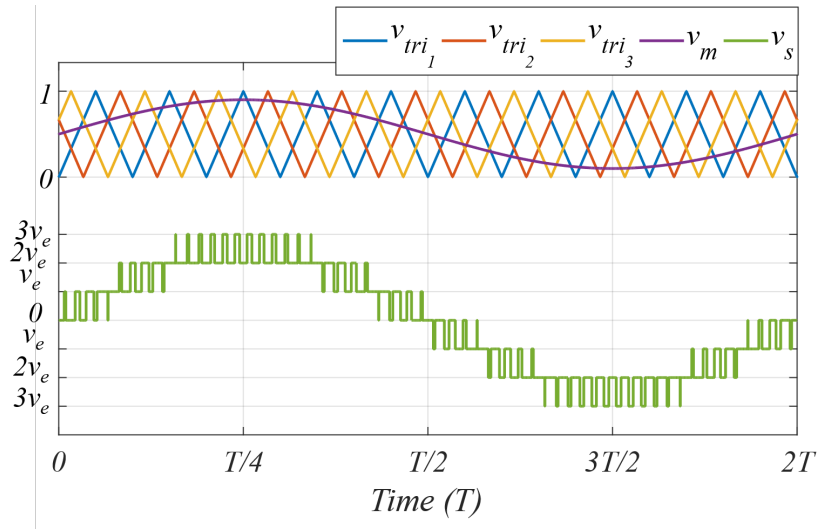
Figure 2.16: v_s of a CFBMC modulated by a Phase-shifted Multicarrier SPWM

Notice that the switching frequency of v_s is considerably higher than the frequency of the carriers. Fig. 2.17 shows the Fourier analysis of this modulation.
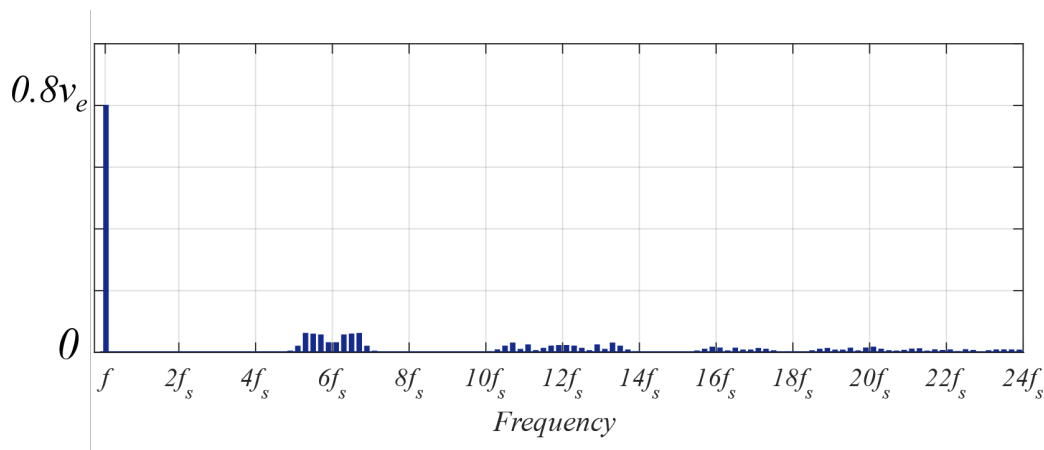
Figure 2.17: Fourier Anlysis of v_s of a CFBMC modulated by a Phase-shifted Multi-carrier SPWM

Fig. 2.17 shows that the Fourier components are shifted to frequencies 6 times higher than the carrier frequency (three times because there are three FBs and two times because it is a unipolar modulation strategy). There are other kinds of multicarrier modulation strategies where a third harmonic is injected or where v_m has a trapezoidal shape. All these modulation strategies are suitable for symmetric MCCs and are not adequate for asymmetric inverters such as THMI. References [26, 27, 36] propose modulation strategies for asymmetric inverter topologies.

2.2.2 Low Frequency Modulation Strategies

Low frequency modulation strategies are the other techniques implemented in multilevel inverters. These techniques are based on turning ON and OFF the switching devices a finite number of times during one period, minimizing the THD [12, 13], or eliminating the most significant harmonics [14, 15, 37]. The main advantage of these techniques is the low switching losses due to the few numbers of switchings for the same power transistor during a period of the modulating signal. Then, it is possible to use slower power devices, which normally support more voltage than the faster ones, allowing them to work with higher voltages. The main issue of these strategies is the complexity in the math computations because the process to find the switching angles are either based on a minimization problem [12] or it is necessary to solve complexes trigonometric system equations by iteration methods [38].

Fig. 2.18 shows the waveform of the output using low frequency modulation strategies, using a CFBMC where each FB changes once per quarter of the period.

The objective of low frequency modulation strategies is to find the switching angles that minimize the THD or minimize or eliminate the most significant harmonics.
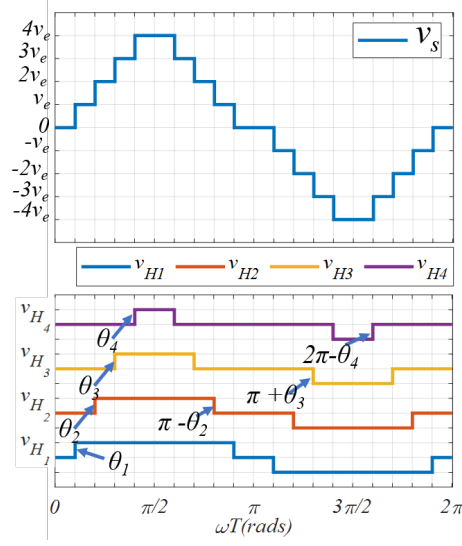
Figure 2.18: Waveform of v_s with low frequency modulation strategy

According to appendix A, the fundamental component of the Fourier analysis when all the sources are identical is:

$$h_1 = \sum_{k=1}^{N} \frac{4v_e}{\pi} \cos(\theta_k) \tag{2.4}$$

And the RMS voltage is:

$$
\begin{aligned}
v_{RMS}^2 =& \frac{2}{\pi} \left(v_e^2 \left(\theta_2 - \theta 1\right) + (2v_e)^2 \left(\theta_3 - \theta_2\right) + (3v_e)^2 \left(\theta_4 - \theta_3\right) + \cdots \right. \\
& \left. + ((N-1)\,v_e)^2 \left(\theta_N - \theta_{N-1}\right) + (Nv_e)^2 \left(\frac{\pi}{2} - \theta_N\right) \right) \\
v_{RMS}^2 =& \frac{2v_e^2}{\pi} \left(-\theta_1 - 3\theta_2 - 5\theta_3 - \cdots - (2N-1)\theta_N + N^2 \frac{\pi}{2} \right) \\
v_{RMS} =& v_e \sqrt{N^2 - \frac{2}{\pi} \sum_{k=1}^{N} (2k-1)\,\theta_k}
\end{aligned}
\tag{2.5}
$$

Hence, the cost function to be minimized is the difference between the square of the RMS value of v_s and the RMS of the fundamental component, constrained to a desired fundamental component, h_1^*

$$
\begin{aligned}
&\min_{\theta_1 \cdots \theta_N} \quad v_e^2 \left(1 - \frac{2}{\pi} \sum_{k=1}^{N} (2k-1)\,\theta_k \right) - \frac{h_1^{*2}}{2} \\
&\text{subject to} \ \sum_{k=1}^{N} \frac{4v_e}{\pi} \cos(\theta_k) - h_1^*
\end{aligned}
\tag{2.6}
$$

There exist many optimization methods that solve this problem as numerical techniques and search methods as genetic algorithms or swarm particles [39]. The other relevant low frequency modulation technique which this chapter explains corresponds to a Selective Harmonic Elimination (SHE), in which the objective is to fix a desired fundamental component and to eliminate some desired harmonics. For that reason, it is necessary to express the waveform of Fig. 2.18, as the sum of its Fourier components, as follows:

$$v_{H_k} = \sum_{m=1}^{\infty} (b_{km} \sin(m\omega t) + a_{km} \cos(m\omega t)) \tag{2.7}$$

Appendix A describes the values of the mth harmonic produced by the kth FB as:

$$b_{km} = \begin{cases} \dfrac{4v_e}{m\pi} \cos(m\theta_k) & ; \quad m \ is \ odd \\ 0 & ; \quad m \ is \ even \end{cases} \tag{2.8}$$

$$a_{km} = 0$$

Hence the output voltage, v_s, expressed as its Fourier components is:

$$v_s = \sum_{k=1}^{N} v_{H_k} \qquad\qquad k = \{1, \cdots, N\} \tag{2.9a}$$

$$v_s = \sum_{k=1}^{N} \sum_{m=1}^{\infty} (b_{km} \sin(m\omega t) + a_{km} \cos(m\omega t)) k = \{1, \cdots N\}, m = \{1, 3, \cdots\} \tag{2.9b}$$

$$v_s = \sum_{i=1}^{N} \sum_{m=1}^{\infty} \frac{4v_e}{m\pi} \cos(m\theta_k) \sin(m\omega t) \qquad k = \{1, \cdots N\}, m = \{1, 3 \cdots\} \tag{2.9c}$$

$$v_s = \sum_{m=1}^{\infty} \left(\frac{4v_e}{m\pi} \underbrace{\sum_{k=1}^{N} (\cos(m\theta_k))}_{h_m} \sin(m\omega t) \right) \qquad k = \{1, \cdots N\}, m = \{1, 3 \cdots\} \tag{2.9d}$$

Hence, the mth harmonic, h_m, is:

$$h_m = \frac{4v_e}{m\pi} \sum_{k=1}^{N} (\cos(m\theta_k)) \tag{2.10}$$

Hence, if there are N switching angles, it is possible to generate a system equation from

(2.10) replacing m to a desired values:

$$h_{m_1} = \frac{4v_e}{m_1\pi} \sum_{k=1}^{N} (\cos(m_1\theta_k))$$

$$h_{m_2} = \frac{4v_e}{m_2\pi} \sum_{k=1}^{N} (\cos(m_2\theta_k)) \qquad (2.11)$$

$$h_{m_N} = \frac{4v_e}{m_N\pi} \sum_{k=1}^{N} (\cos(m_N\theta_k))$$

where h_{m_k} is the value adjusted for the m_k^{th} harmonic. Hence, it possible to adjust the fundamental component and to eliminate $N-1$ desired harmonics, replacing $m_1 = 1$, $h_{m_1} = h_1^*$, $h_{m_k} = 0$ for the harmonics to be eliminated. There are many methods to solve this system equation such as numeric methods as Newton Raphson [38] or minimization techniques [40], or search methods as genetic algorithms or Swarm Particle or General Pattern Search [14, 37, 41]. However, if the initial conditions are not suitable, the methods may not find the solution, and there is no manner to know if the system has no feasible solution.

Furthermore, they can take excessive time to be implemented in real-time. Finally, there are algebraic methods that find all the set of solutions of the system equation [15, 42–44], without initial condition. [15, 43, 44] convert the trigonometric system equation to a polynomial system, based on $\cos(n\theta) = T_n(\cos(\theta))$. In [42] the polynomial system equation is solved based on that the system corresponds to a symmetric polynomial, and in [15, 43] a conversion to its Groebner Basis is implemented, uncoupling the system equation. Groebner Basis is explained in detail in [43, 45]. In [44] a unification of [43] and [42] are developed. These methods allow also to know if the solutions are feasible. However, the main problem of these methods is the complexity of the solving process in real-time, because, the roots of the polynomial system equation must be found in real-time, taking into account the disturbances in the input voltages, or designing a feedback system that compensates the disturbances. For that reason, most of these methods find the solution with pre-processing techniques. Nevertheless, if a disturbance in the input voltages is produced, there is no manner to readjust the angles for canceling the harmonics with the new appropriate values. One solution to solve this issue is to embed a look-at-table in the processor. However, if a robust system is required it is necessary to use a look-at-table with a lot of information, that may overload the processor. Another solution is to implement a control law to this modulation strategy as [40, 46] propose, using the Jacobian of the harmonics for implementing a linear controller. However, if a disturbance in the input voltage is too high this control strategy using on-the-fly updated values might make the system unstable. As conclusion, low frequency modulation strategies are very efficient and can be implemented in symmetric inverters. However, the complexity of the equations is an issue and does not allow an online computation implementation. Moreover, if a disturbance occurs in the inverters, the time required to update the switching angles can introduce excessive delays and make the system unstable.

2.2.3 Control techniques for Multilevel Converters

In MCCs there are many objectives to achieve, as balancing the cell-variable (CV), regulating a global variable (GV), having fault tolerance ability, minimizing or equalizing the step voltage size in asymmetric inverters, suitable start-up, etc. In some cases, these objectives are achieved with a right modulation strategy such as happen in [26, 27], where generating a piece-wise function for each switching device, the equalized step size is achieved in a THMI. In other cases, as in a Flying-Capacitor Multilevel Converter, adding some extra circuits in the hardware [47] balances the cell-variables and also produces a soft start-up. In the case of THMI, a right modulation produces a right step size as shown in [26, 27, 36], minimizing the ripple of the current, improving the acquisition of this signal to control.

Most of MCCs present an input filter in the input of the system for smoothing the input current, generating oscillations in the input voltages. This fact disturbs the output variable and in some cases unbalances the cell-variable. For that reason, a balancing controller is necessary to maintain balanced the desired cell-variables. Furthermore, an output global regulator is necessary for maintaining the desired references if the load or the input voltage change. To regulate the output global variable, there exist several types of controllers that in some cases are designed for a two-level converter but can be generalized to MCCs. Reference [48, 49] proposes a backstepping controller for a FB inverter working as a stand-alone or grid-tied mode. The backstepping controller consists of a Recursive Lyapunov Controls, ensuring the stability of the variables by stages. In [50] an Adaptive Sliding Mode Controller (SMC) is implemented for an inverter working either as isolated or grid-tied mode, controlling the output voltage or current respectively. SMCs are also applied in a Flying-Capacitor Multilevel Converter presenting a good response. Either back-stepping and SMC controllers have the advantage that they use the nonlinear model of the converter and have a nonlinear control law, improving the robustness and the performance. SMCs are based on a sliding surface, which is a function of the states of variables equalized to zero and presents two stages, a continuous stage, and a switching stage. When the function of the state of variables is out from the sliding surface, the switching action acts. The main issue of SMCs is the chattering effect, produced by the switching part, which consists of high-frequency oscillations in the system. Chattering effect is increased in the Multicellular converters, especially in asymmetric inverters. In [51] a variation of SMC is proposed where no switching stage is present, having a tolerable operating region, where the stability is not ensured. However, this region can be reduced to a range that can be acceptable. This controller is validated in [26], implementing it in a THMI in grid-tied mode, having good experimental and simulation results, disturbing the input voltages and changing the phase and amplitude of the current reference.

Other controllers very interesting that are used in power converters are the predictive control or MPC, which produces a horizon of events. Based on this horizon, a control law is designed, minimizing a cost function that is related to the error of the variables to be controlled and the variation of the input. These controllers take into account the

physical restrictions as the bounds of the inputs or the maximum tolerable error.

To balance the cell-variables there exist many interesting balancing controllers designed either for CFBMC, FCMC or Multiphase Buck. In [52] a reference for each cell-variable is generated and a predictive controller is synthesized. The main issue of generating a reference to each cell-variable is that if a disturbance in any parameters is produced, or if a cell is inserted or removed, the references of each CV could have to be recalculated as happen in the Flying-Capacitor Multilevel Converter when the input voltage changes. In [7, 10], another strategy for balancing of cell-variables is proposed for CEMI, comparing the local cell variable to the neighbors. These techniques are based on a drop controller, emulating the converter to a Thevenin circuit, in which the output impedance of each FB is compared with its neighbors. There exist other balancing controllers the FBs as [9]. For the Multiphase Buck, an Adaptive Voltage Positioning (AVP) control method is designed in [6, 11, 16]. This controller allows regulating the output voltage and balancing the leg currents. To balance the leg currents, each current is compared to the neighboring currents, and to regulate the output voltage, a drop control is implemented. For the Flying-Capacitor Multilevel Converter, in [3] a decentralized local controller is proposed, which consists of three stages: balancing the CVs, regulating the output current and a bypass circuit used to manage a reconfiguration order. A similar control method is implemented in [8], for a CFBMC in a grid-tied mode, balancing the output voltage of the FBs and controlling the output current. [3, 8] are based on this thesis.

About the control for low frequency modulation strategies, in [40, 46] a linear control is proposed for a SHE, finding the switching angles offline, and using a Tailor approximation of the harmonics.

$$\mathbf{H} = \left(\left. \frac{\partial \mathbf{H}}{\partial \mathbf{\Theta}} \right|_{(\mathbf{H_o}, \mathbf{Z_o})} \right) (\mathbf{\Theta} - \mathbf{\Theta_o}) + \mathbf{H_o} \qquad (2.12)$$

Where $\mathbf{H_o}$ are the operating point values of the harmonics that are controlled, and $\mathbf{\Theta_o}$ are the operating point values of the switching angles. Based on (2.10) a PI controller is implemented. This control works well if small disturbances are produced. However, if a high disturbance occurs, the controller can turn the system unstable.

Chapter 3

Decentralized controller for a Multi Cell Converter

Most of the time, multicellular converters require to implement a specific control loop to balance either the inductor current for the parallel topologies or the capacitor voltages for the serial ones. There exist many types of balancing methods depending on the types of converter topology addressed [3, 6–11, 16]. However, the complexity increases when the number of cells increases. Moreover, several methods exist also to regulate the GV of the MCC. Nevertheless, it is possible that when it is necessary to control other variables like balancing CVs, the action of each controller can disturb the other loops and affects the stability.

This chapter presents a control strategy that can be implemented in a wide range of symmetric MCCs of N levels. As mentioned in the introduction, MCC is composed of an arrangement of cells that can be connected in parallel or series. Furthermore, several state-variables, i.e. the CVs and the GV, are linked together depending on the topology of the MCC. The proposed control strategy allows to balance one of the CVs, depending on the application and to regulate a Global Variable with the desired reference. Furthermore, this control strategy introduces a bypass system that allows the user to insert or remove very easily an active cell of the converter during operation, giving the opportunity to manage the fault tolerance concern in a more straightforward manner. Before introducing the decentralized control concept, an overview of the several MCC topologies is presented and their similarities in terms of state-variables (i.e. energy storage) local and global are discussed and highlighted.

3.1 Model of three Topologies of Multicellular Converters

To have a general idea of the similarities and the differences of multicellular converters, this section describes the model of three topologies of MCCs, which are the Flying-Capacitor Multilevel Converter, The cascaded Full-Bridge Multilevel Converter, and the Multiphase Buck converter.

3.1.1 Model of the flying-Capacitor Multilevel Converter

This section models a CFBMC connected to a Inductive- resistive load, as Fig. 3.1 shows:
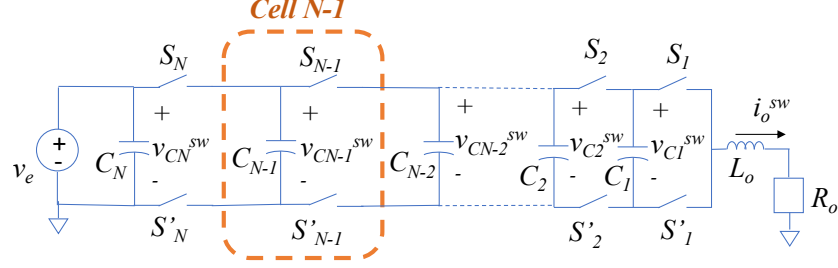
Figure 3.1: Schematic of a Flying-Capacitor Multilevel Converter

where S'_k is the opposite control signal of S_k. According to Fig. 3.1 the current through the capacitors flows as mentioned in Fig. 3.2
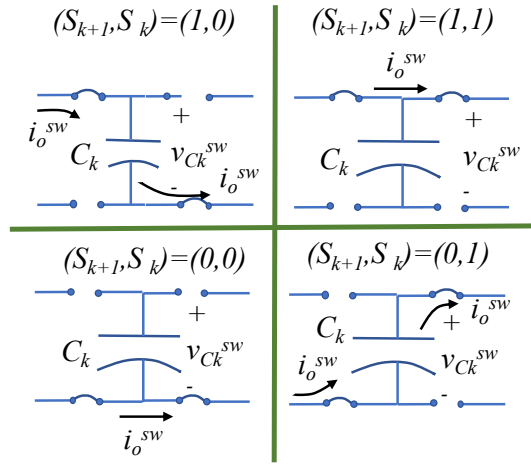
Figure 3.2: Current flowing through the flying-capacitor

Based on Fig. 3.2, the switching dynamic model of the capacitor voltages are:

$$\dot{v}^{sw}_{C_k} = \frac{i^{sw}_o}{C_k}(S_{k+1} - S_k) \qquad ;k = \{1 \quad 2 \quad \cdots \quad N-1\} \tag{3.1a}$$

$$\dot{v}^{sw}_{C_N} = \dot{v}_e \tag{3.1b}$$

Considering the values of the capacitor voltages, the expression of the output current (i^{sw}_o) can be obtained based on the topology shown in Fig. 3.1:

$$
\begin{aligned}
L_o\dot{i}^{sw}_o &= S_1\left(v^{sw}_{C_1} - v^{sw}_{C_0}\right) + S_2\left(v^{sw}_{C_2} - v^{sw}_{C_1}\right) + S_3\left(v^{sw}_{C_3} - v^{sw}_{C_2}\right) + \cdots + S_N\left(v^{sw}_{C_N} - v^{sw}_{C_{N-1}}\right) \\
&\quad - R_o i^{sw}_o \\
L_o\dot{i}_o^{\ sw} &= \sum_{k=1}^{N} S_k\left(v^{sw}_{C_k} - v^{sw}_{C_{k-1}}\right) + S_1 v^{sw}_{C_1} - R_o i_o
\end{aligned}
\tag{3.2}
$$

where $v_{C0} = 0$. In order to obtain the average model, lets define $\phi(t)$ as the moving average from t to $t + T_{sw}$ of $\phi^{sw}(t)$:

$$\phi(t) = \frac{1}{T_{sw}} \int_t^{t+T_{sw}} \phi^{sw}(\tau)d\tau \tag{3.3}$$

Hence, applying the moving average to (3.1), the average model becomes:

$$\dot{v}_{C_k} = \frac{i_o}{C_k}(d_{k+1} - d_k) \qquad ;k = \left\{1 \quad 2 \quad \cdots \quad N-1\right\} \tag{3.4a}$$

$$\dot{v}_{C_N} = \dot{v}_e \tag{3.4b}$$

And the average model of (3.2) is:

$$L_o \dot{i}_o = \sum_{k=1}^N d_k \left(v_{C_k} - v_{C_{k-1}}\right) - R_o i_o \tag{3.5}$$

where d_k is the average of the switching state S_k, that also corresponds to the duty-cycle of S_k.

Expressing (3.4) and (3.5) in a matrix form, it follows:

$$\dot{\mathbf{V}}_\mathbf{C} = i_o \mathbf{C}^{-1} \mathbf{A_o} \mathbf{D} + \mathbf{E}\dot{v}_e \tag{3.6a}$$

$$\dot{i}_o = \frac{1}{L_o} \mathbf{D}^T \mathbf{T_V} \mathbf{V_C} - \frac{R_o}{L_o} i_o \tag{3.6b}$$

where $\mathbf{V_C} = \begin{bmatrix} v_{C_1} & v_{C_2} & \cdots & v_{C_N} \end{bmatrix}^T$; $\mathbf{D} = \begin{bmatrix} d_1 & d_2 & \cdots & d_N \end{bmatrix}^T$; $\mathbf{E} = \begin{bmatrix} 0 & \cdots & 0 & 1 \end{bmatrix}^T$

$$\mathbf{C} = \begin{bmatrix} C_1 & \cdots & 0 & 0 \\ \vdots & \ddots & \vdots & \vdots \\ 0 & \cdots & C_{N-1} & 0 \\ 0 & \cdots & 0 & C_N \end{bmatrix} ; \mathbf{A_o} = \begin{bmatrix} -1 & 1 & \cdots & 0 \\ 0 & \ddots & \ddots & \vdots \\ \vdots & \ddots & -1 & 1 \\ 0 & \cdots & 0 & 0 \end{bmatrix} ; \mathbf{T_V} = \begin{bmatrix} 1 & 0 & \cdots & 0 \\ -1 & 1 & \ddots & \vdots \\ \vdots & \ddots & \ddots & 0 \\ 0 & \cdots & -1 & 1 \end{bmatrix}$$

Defining $\mathbf{C} = C_o \boldsymbol{\Gamma}$, where $C_o = C_N$ and

$$\boldsymbol{\Gamma} = \begin{bmatrix} \gamma_1 & \cdots & 0 & 0 \\ \vdots & \ddots & \vdots & \vdots \\ 0 & \cdots & \gamma_{N-1} & 0 \\ 0 & \cdots & 0 & 1 \end{bmatrix}$$

and $\gamma_k = \dfrac{C_k}{C_N}$. Rearranging the equations it follows:

$$\dot{\mathbf{V}}_\mathbf{C} = \frac{i_o}{C_o} \boldsymbol{\Gamma}^{-1} \mathbf{A_o} \mathbf{D} + \mathbf{E}\dot{v}_e \tag{3.7a}$$

$$\dot{i}_o = \frac{1}{L_o} \mathbf{D}^T \mathbf{T_V} \mathbf{V_C} - \frac{R_o}{L_o} i_o \tag{3.7b}$$

In order to apply the decentralized control method to balance the CVs, it is necessary to perform a change of variable, replacing the capacitor voltages in the previous equation by the cell-voltages, v_k, defined as the difference of the adjacent capacitor voltages of the cells. Therefore, the kth cell-voltage is described as:

$$v_k = v_{C_k} - v_{C_{k-1}} \quad ; k = \left\{ 1 \quad 2 \quad \cdots \quad N \right\} \tag{3.8}$$

Expressing the cell-voltages as a matrix form:

$$\mathbf{V} = \mathbf{T_V} \mathbf{V_C} \tag{3.9}$$

Obtaining the derivative of $\mathbf{V}$ respect to the time it follows:

$$\dot{\mathbf{V}} = \mathbf{T_V} \dot{\mathbf{V}}_\mathbf{C} \tag{3.10}$$

Replacing by (3.7a)

$$\dot{\mathbf{V}} = \frac{i_o}{C_o} \underbrace{\mathbf{T_V} \boldsymbol{\Gamma}^{-1} \mathbf{A_o}}_{\mathbf{A_T}} \mathbf{D} + \dot{v}_e \mathbf{T_V} \mathbf{E} \, \mathbf{E} \tag{3.11}$$

where

$$\mathbf{A_T} = \begin{bmatrix} -\dfrac{1}{\gamma_1} & \dfrac{1}{\gamma_1} & 0 & \cdots & 0 & 0 \\[2mm] \dfrac{1}{\gamma_1} & -\left(\dfrac{1}{\gamma_1} + \dfrac{1}{\gamma_2}\right) & -\dfrac{1}{\gamma_2} & 0 & \ddots & \vdots \\[2mm] 0 & -\dfrac{1}{\gamma_2} & -\left(\dfrac{1}{\gamma_2} + \dfrac{1}{\gamma_3}\right) & \ddots & \ddots & 0 \\[2mm] \vdots & \ddots & \ddots & \ddots & -\dfrac{1}{\gamma_{N-2}} & 0 \\[2mm] 0 & \cdots & 0 & \dfrac{1}{\gamma_{N-2}} & -\left(\dfrac{1}{\gamma_{N-2}} + \dfrac{1}{\gamma_{N-1}}\right) & \dfrac{1}{\gamma_{N-1}} \\[2mm] 0 & 0 & \cdots & 0 & \dfrac{1}{\gamma_{N-1}} & -\dfrac{1}{\gamma_{N-1}} \end{bmatrix}$$

Notice in $\mathbf{A_T}$ that the sum of the elements of each column and row are equal to 0, meaning that $\mathbf{A_T}$ is a graph, according to [53, 54]

Inserting (3.9) in (3.6b), it follows:

$$\dot{i}_o = \frac{1}{L_o} \mathbf{D}^T \mathbf{V} - \frac{R_o}{L_o} i_o \tag{3.12}$$

Finally, according to (3.11) and (3.12), the the average model expressed with the cell-voltage variable of the FCMC is:

$$\begin{bmatrix} \dot{\mathbf{V}} \\ \dot{i}_o \end{bmatrix} = \begin{bmatrix} \dfrac{i_o}{C_o}\mathbf{A_T}\mathbf{D} + \mathbf{E}\dot{v}_e \\ \dfrac{1}{L_o}\mathbf{D}^T\mathbf{V} - \dfrac{R_o}{L_o}i_o \end{bmatrix} \tag{3.13}$$

Based on (3.13), it is possible to represent the converter behavior with the following equivalent circuit :
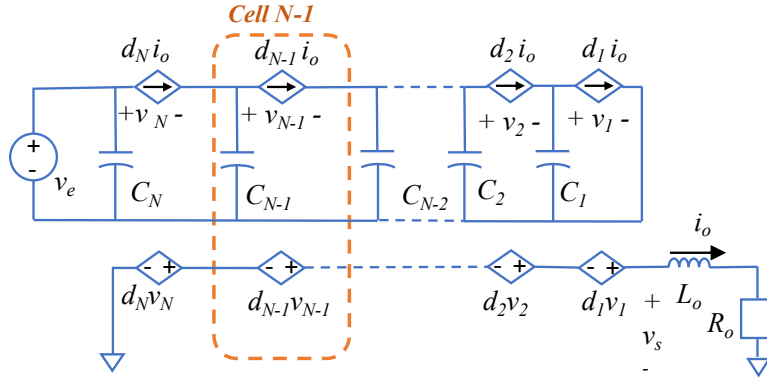
Figure 3.3: Equivalent circuit of the Flying-Capacitor Multilevel Converter

According to Fig. 3.3, it can be observed that:

$$\sum_{k=1}^{N} v_k = v_e \tag{3.14}$$

Expressed as a matrix form, means:

$$\mathbf{V_1}^T\mathbf{V} = v_e \tag{3.15}$$

where $\mathbf{V_1} = \begin{bmatrix} 1 & 1 & \cdots & 1 \end{bmatrix}^T$. Furthermore, Fig. 3.3 shows a strong link between the output current and cell-voltages. Fig. 3.4 shows more clearly the link between the cell-voltage and the output current:
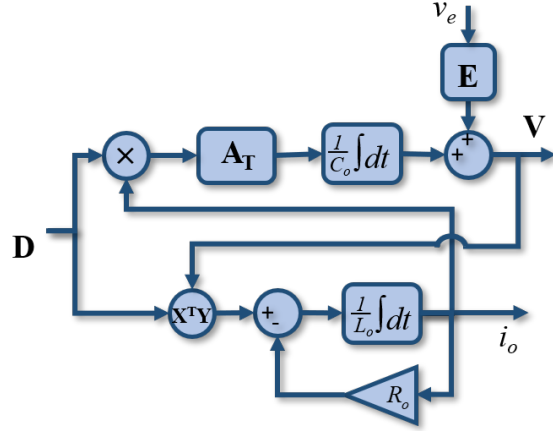
Figure 3.4: Block diagram of the equivalent model of the flying capacitor

In order to apply the decentralized control method, it is necessary to linearize the average model. Hence, Defining the small and the DC value:

$$
\begin{aligned}
\mathbf{V} &= \bar{\mathbf{V}} + \hat{\mathbf{V}} & \mathbf{D} &= \bar{\mathbf{D}} + \hat{\mathbf{D}} \\
i_o &= \bar{i}_o + \hat{i}_o & v_e &= \bar{v}_e + \hat{v}_e
\end{aligned}
\tag{3.16}
$$

the small signal model is:

$$
\begin{bmatrix} \dot{\hat{\mathbf{V}}} \\[2mm] \dot{\hat{i}}_o \end{bmatrix} = \begin{bmatrix} \dfrac{\bar{i}_o}{C_o}\mathbf{A_T}\hat{\mathbf{D}} + \dfrac{\hat{i}_o}{C_o}\mathbf{A_T}\bar{\mathbf{D}} + \mathbf{E}\dot{\hat{v}}_e \\[4mm] \dfrac{1}{L_o}\bar{\mathbf{D}}^T\hat{\mathbf{V}} + \dfrac{1}{L_o}\hat{\mathbf{D}}^T\bar{\mathbf{V}} - \dfrac{R_o}{L_o}\hat{i}_o \end{bmatrix}
\tag{3.17}
$$

With the DC equations is:

$$
0 = \frac{\bar{i}_o}{C_o}\mathbf{A_T}\bar{\mathbf{D}}
\tag{3.18a}
$$

$$
0 = \bar{\mathbf{D}}^T\bar{\mathbf{V}} - R_o\bar{i}_o
\tag{3.18b}
$$

Solving (3.18a):

$$
\bar{d}_1 = \bar{d}_2 = \cdots = \bar{d}_N = \bar{d}
\tag{3.19}
$$

where $\bar{d}$ is the average value of the duty-cycle applied to all the cells. Expressed as a matrix form, it follows:

$$
\bar{\mathbf{D}} = \bar{d}\mathbf{V_1}
\tag{3.20}
$$

Replacing (3.20) in (3.18b):

$$
0 = \bar{d}\mathbf{V_1}^T\bar{\mathbf{V}} - R_o\bar{i}_o
\tag{3.21}
$$

Taking into account that (3.15) is also valid for DC and small signals, it follows:

$$\bar{d} = \frac{R_o \bar{i}_o}{\bar{v}_e} \tag{3.22}$$

As it is mentioned at the beginning of this work, one the objective is to balance the cell-voltages, Hence:

$$\bar{v}_1 = \bar{v}_2 = \cdots = \bar{v}_N = \bar{v} \tag{3.23}$$

where $\bar{v}$ is the average value of all the cell-voltages. Expressing as a matrix form, it follows:

$$\overline{\mathbf{V}} = \bar{v}\mathbf{V_1} \tag{3.24}$$

Based on (3.15), it follows:

$$\bar{v}_e = \mathbf{V_1}^T \overline{\mathbf{V}} \tag{3.25a}$$

$$\bar{v}_e = \bar{v}\mathbf{V_1}^T\mathbf{V_1}^{\nearrow N} \tag{3.25b}$$

$$\bar{v} = \frac{\bar{v}_e}{N} \tag{3.25c}$$

Inserting all the obtained average values in the small signal model described in (3.17) it follows:

$$\begin{bmatrix} \dot{\hat{\mathbf{V}}} \\[2mm] \dot{\hat{i}}_o \end{bmatrix} = \begin{bmatrix} \dfrac{\bar{i}_o}{C_o}\mathbf{A_T}\hat{\mathbf{D}} + \bar{d}\dfrac{\hat{i}_o}{C_o}\mathbf{A_T}\mathbf{V_1}^{\nearrow \mathbf{0}} + \mathbf{E}\hat{v}_e \\[4mm] \bar{d}\dfrac{1}{L_o}\mathbf{V_1}^T\hat{\mathbf{V}}^{\nearrow \hat{v}_e} \dfrac{\bar{v}_e}{N}\dfrac{1}{L_o}\hat{\mathbf{D}}^T\mathbf{V_1} - \dfrac{R_o}{L_o}\hat{i}_o \end{bmatrix} \tag{3.26}$$

Expressing (3.26) in a LAPLACE domain:

$$\begin{bmatrix} \mathbf{V}(s) \\[2mm] I_o(s) \end{bmatrix} = \begin{bmatrix} \dfrac{\bar{i}_o}{C_o s}\mathbf{A_T}\mathbf{D}(s) + \mathbf{E}V_e(s) \\[4mm] \dfrac{1}{L_o s + R_o}\left(\dfrac{\bar{v}_e}{N}\mathbf{V_1}^T\mathbf{D}(s) + \bar{d}V_e(s) \right) \end{bmatrix} \tag{3.27}$$

Notice that according to (3.27), both $\mathbf{V}(s)$ and $I_o(s)$ are affected by disturbances in $V_e(s)$. Furthermore, both cell-voltages and output current depend on the small signal of the duty-cycles. However, cell-voltage and output current do not affect each other. Fig. 3.5 shows a block diagram of the small-signal model of the converter. Notice that the variables are decoupled. However, both depend on the duty-cycle. The cell-voltage depends on the duty-cycles of the neighbors and the duty-cycle of its cell, while the output current depends on the sum of the duty-cycles.
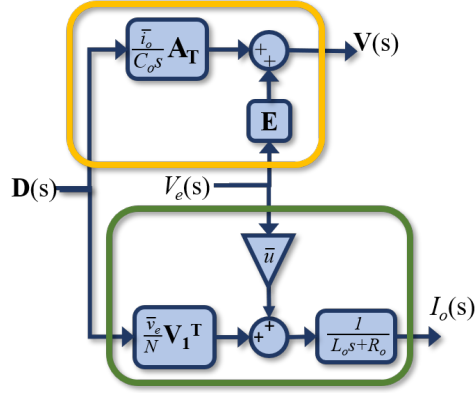
Figure 3.5: Block Diagram of the small signal model of the converter

In order to have a better understanding of the system, Fig. 3.6 shows the equivalent circuit of the small signal model.
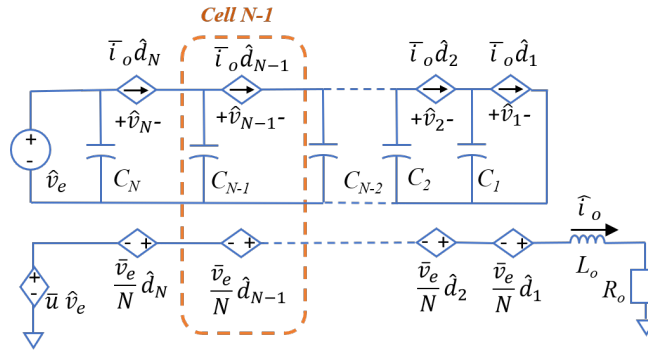
Figure 3.6: Equivalent circuit of the small signal model of the flying-capacitor multilevel converter

It can be observed that in the circuit, that just the duty cycles affect the cell-voltages and the output current without correlation between them.

The next topology that is modeled is the cascaded Full-Bridge Multilevel Converter.

3.1.2 Model of the cascaded Full-Bridge Multilevel Converter

The System is composed of N Full-Bridges, supplied by independent voltage sources $v_{e1}, v_{e2}, ..v_{eN}$, where v_{ek} has a nominal value equals to v_e. Each FB has an input filter required to smooth the current delivered by the voltage sources. Indeed, with the input voltage sources used Lithium-ion batteries, the current they deliver need to not change too fast. There exist many advantages for using CFBMC as the reduction of the output filter because of the increment of the apparent output frequency and also the $2N + 1$ levels obtained at the output of the converter thanks to the N cascaded full-bridges, reducing the THD. In this work, the CFBMC is connected to an output inductance and a resistive load as shown in Fig. 3.7.
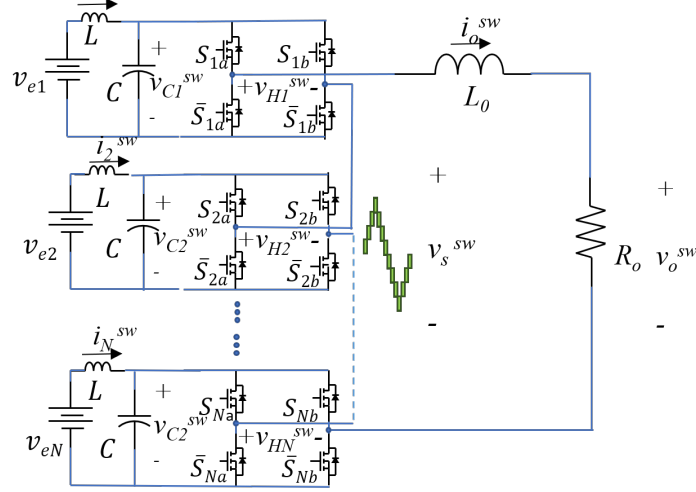
Figure 3.7: Cascaded Full-Bridge Multilevel Converter of N levels

Where $S_{k\nu}$ and $\overline{S_{k\nu}}$ are the switches of the inverter. $\overline{S_{k\nu}}$ receives the opposite control signals of $S_{k\nu}$. $k = \{1, 2, \cdots, N\}$ and represents the cell. $\nu = \{a, b\}$ represents the branch, a for the left and b for the right branch. To increase the apparent frequency of the voltage ripple at the output, v_s, a phase shift multi-carrier SPWM modulation strategy is used for this work. It allows the implementation of a small output inductance or the minimization of the ripple of the output current. This modulation strategy shifts the carrier of the kth Full-Bridge (FB_k) $\dfrac{180}{N}(k-1)°$. Reference [26, 27] shows the simulation and experimental results in open-loop of this modulation strategy, implemented in two prototypes, one made of G_aN and the other made of S_i power transistors. The objective of this topology is to balance the power supplied by each FB and to regulate the output current. For modeling the converter, Fig. 3.8 illustrates the kth FB of the converter, according to the different states of the switches.
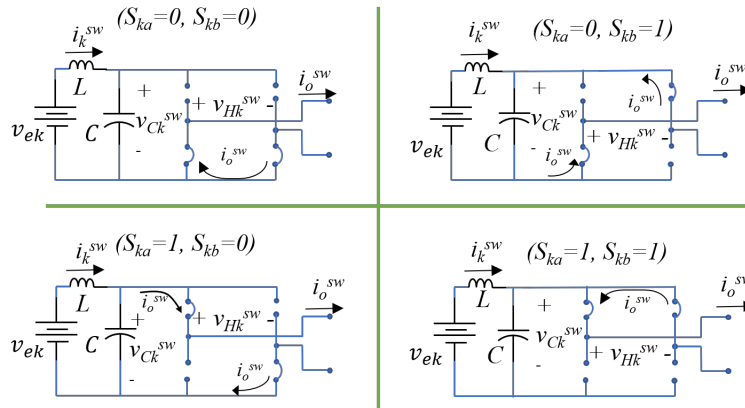
Figure 3.8: One cell of the Cascaded Full-Bridge Multilevel Converter.

Based on Fig. 3.8 the switching model of the capacitor voltage v_{Ck}, the input current i_k and the output voltage fo the FB, v_{Hk}, is:

$$L\dot{i}_k^{sw} = v_{ek} - Ri_k^{sw} - v_{Ck}^{sw}$$
$$C\dot{v}_{Ck}^{sw} = i_k^{sw} - (S_{ka} - S_{kb})\,i_o^{sw} \tag{3.28}$$

$$v_{Hk}^{sw} = (S_{ka} - S_{kb})\,v_{Ck}^{sw}$$

Analogously to (3.28) and according to 3.7 the switching dynamical model of the output current, i_o^{sw}, and the output voltage, v_s^{sw}, are:

$$L_o \dot{i}_o^{sw} = v_s^{sw} - R_s i_o^{sw} - R_o i_o^{sw} \tag{3.29a}$$

$$v_s^{sw} = \sum_{k=1}^{N} v_{Hk}^{sw} \tag{3.29b}$$

where R is the DC Resistance (DCR) of L and $R_s = 2NR_{DS} + R_{L_o}$. R_{L_o} is the DCR of L_o and R_{DS} is the Drain Source ON resistance of the switching devices $S_{k\nu}$. Inserting (3.29b) in (3.29a) it follows:

$$L_o \dot{i}_o^{sw} = \sum_{k=1}^{N} v_{Hk}^{sw} - R_s i_o^{sw} - R_o i_o^{sw} \tag{3.30}$$

Obtaining the average model of (3.28) and (3.30), based on the moving average defined in (3.3), it follows:

$$L\dot{i}_k = v_{ek} - v_{Ck} - Ri_k \tag{3.31a}$$
$$C\dot{v}_{Ck} = i_k - (d_{ka} - d_{kb})\,i_o \tag{3.31b}$$

$$L_o \dot{i}_o = \sum_{k=1}^{N} v_{Hk} - R_s i_o - R_o i_o \tag{3.31c}$$

$$v_{Hk} = (d_{ka} - d_{kb})\,v_{Ck} \tag{3.31d}$$

where $d\_k\nu$ represents the duty-cycle of the switch $S_{k\nu}$.

Defining d_k as:

$$d_k = d_{ka} - d_{kb} \tag{3.32}$$

which $-1 < d_k < 1$. Hence, replacing (3.32) in (3.31)

$$L\dot{i}_k = v_{ek} - v_{Ck} - Ri_k \tag{3.33a}$$
$$C\dot{v}_{Ck} = i_k - d_k i_o \tag{3.33b}$$

$$L_o \dot{i}_o = \sum_{k=1}^{N} v_{Hk} - R_s i_o - R_o i_o \tag{3.33c}$$

$$v_{Hk} = d_k v_{Ck} \tag{3.33d}$$

Expressing as a matrix form it follows:

$$L\dot{\mathbf{I}} = \mathbf{V_e} - \mathbf{V_C} - R\mathbf{I} \tag{3.34a}$$

$$C\dot{\mathbf{V}}_{\mathbf{C}} = \mathbf{I} - i_o\mathbf{D} \tag{3.34b}$$

$$L_o\dot{i}_o = \mathbf{D}^T\mathbf{V_C} - R_s i_o - R_o i_o \tag{3.34c}$$

$$\mathbf{V_H} = \mathbf{D} \odot \mathbf{V_C} \tag{3.34d}$$

Where $\mathbf{I} = \begin{bmatrix} i_1 & i_2 & \cdots & i_N \end{bmatrix}^T$, $\mathbf{V_C} = \begin{bmatrix} v_{C1} & v_{C2} & \cdots & v_{CN} \end{bmatrix}^T$, $\mathbf{V_e} = \begin{bmatrix} v_{e1} & v_{e2} & \cdots & v_{eN} \end{bmatrix}^T$, $\mathbf{D} = \begin{bmatrix} d_1 & d_2 & \cdots & d_N \end{bmatrix}^T$, $\mathbf{V_H} = \begin{bmatrix} v_{H1} & v_{H2} & \cdots & v_{HN} \end{bmatrix}^T$,

and $\odot$ represents the Hadmard product [55, 56], that is the product point to point of the vectors involved. Eq. (3.34) corresponds to the average dynamic model of a CFBMC. Based on (3.34), the equivalent circuit of the average model is:
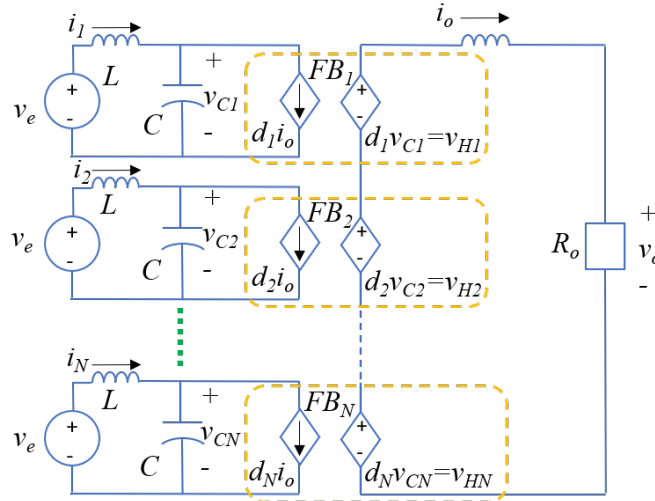
Figure 3.9: Equivalent Circuit of a CFBMC

Fig. 3.9 shows the link between each FB and the output current. Furthermore, it can be observed the contribution of each FB. Additionally, it is possible to infer that the output current of each FB is the same, i_o. Hence, if all the output voltage of the FBs are balanced, the output power is also balanced. For that reason, the CV to be balanced in this topology is v_{Hk}. Fig. 3.10 shows the block diagram of the system.

Notice the link existing between the CV, $\mathbf{V_H}$, and the GV, i_o. It can be seen that i_o affects $\mathbf{V_H}$ and vice versa. In order to design the controller, it is necessary to linearize the model. However, because of this converter can be used either as an inverter or as a DC/DC converter, the common linearization around an operation point is not suitable. Another linearization method is to apply a DQ transform and then linearize around the operation point. Nevertheless, DQ transform, generates 2 output currents, direct and quadrature currents and the control method that is going to be proposed manage only
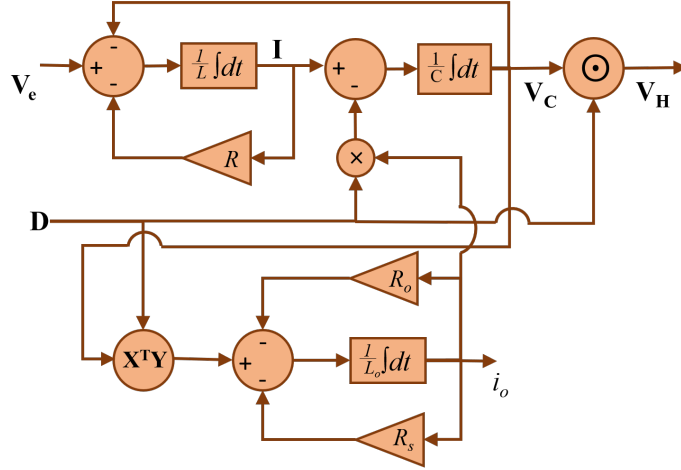
Figure 3.10: Block Diagram of a CFBMC.

GV. For that reason, the linear model implemented in this research is the one used in [26, 51], which consists in define $\delta_{v_{Ck}}$ as the oscillation voltage in the capacitor where:

$$\delta_{v_{Ck}} = L\dot{i}_k - Ri_k \tag{3.35}$$

With:

$$v_{C_k} = v_{ek} + \delta_{v_{Ck}} \tag{3.36}$$

Taking into account that in this topology all the input sources have the same value, $v_{e1} = v_{e2} = \cdots = v_{eN} = v_e$. Inserting (3.36) in (3.33a) and (3.33b), it follows:

$$L_o\dot{i}_o = \sum_{k=1}^{N} d_k v_e + \sum_{k=1}^{N} d_k \delta_{v_{Ck}} - R_s i_o - R_o i_o \tag{3.37a}$$

$$v_{Hk} = d_k v_e + d_k \delta_{v_{Ck}} \tag{3.37b}$$

According to [26, 51], if all the inputs d_k are bounded and periodic, $\delta_{v_{Ck}}$ can be defined as a bounded and periodic disturbance. Defining $\delta_{v_{Hk}}$ as:

$$\delta_{v_{Hk}} = \delta_{V_{Ck}} d_k \tag{3.38}$$

and replacing (3.38) in (3.37) it follows

$$L_o\dot{i}_o = \sum_{k=1}^{N} d_k v_e + \sum_{k=1}^{N} \delta_{v_{Hk}} - (R_s + R_o) i_o \tag{3.39a}$$

$$v_{Hk} = d_k v_e + \delta_{v_{Hk}} \tag{3.39b}$$

It can be observed that (3.39) corresponds to a linear model, where $\delta_{v_{Hk}}$ represents the oscillation produced by the kth input filter as a disturbance. It has to mention that because of $\delta_{V_{Ck}}$ and d_k are bounded, $\delta_{v_{Hk}}$ is also bounded.

Eq. (3.40) shows the linear model as a matrix form:

$$L_o \dot{i}_o = v_e \mathbf{V_1}^T \mathbf{D} + \mathbf{V_1}^T \mathbf{\Delta_{V_H}} - (R_s + R_o)\,i_o \tag{3.40a}$$

$$\mathbf{V_H} = v_e \mathbf{D} + \mathbf{\Delta_{V_H}} \tag{3.40b}$$

Converting the model in the LAPLACE domain it follows:

$$I_o(s) = \frac{1}{L_o s + (R_o + R_s)}\left(v_e \mathbf{V_1}^T \mathbf{D}(s) + \mathbf{V_1}^T \mathbf{\Delta_{V_H}}(s)\right) \tag{3.41a}$$

$$\mathbf{V_H}(s) = v_e \mathbf{D}(s) + \mathbf{\Delta_{V_H}}(s) \tag{3.41b}$$

Notice that the output current depends on the sum of the duty-cycles, while the output voltage of the FBs depends on the duty-cycle of it cell. (3.41) can be also expressed as:

$$I_o(s) = \frac{1}{L_o s + (R_o + R_s)}\mathbf{V_H}(s) \tag{3.42a}$$

$$\mathbf{V_H}(s) = v_e \mathbf{D}(s) + \mathbf{\Delta_{V_H}}(s) \tag{3.42b}$$

Notice that in this case the output current depends on the sum of the output voltage of the FBs. Either (3.41) or (3.42) represent the linear model of a CFBMC, able to work as a DC/DC converter and as an inverter. Fig. 3.11 shows the equivalent circuit of the system.
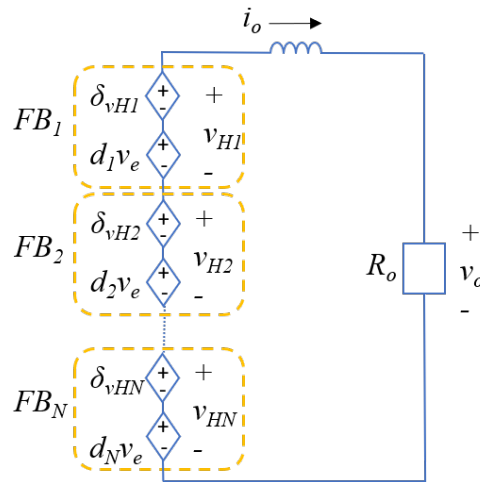
Figure 3.11: Equivalent circuit of the linear model
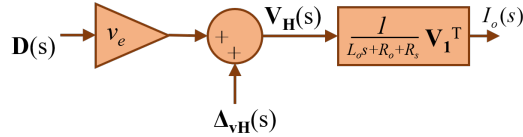
Figure 3.12: Block Diagram of the Linear model

In Fig. 3.11 it can be seen the contribution of each cell to the system and also how do they affect the output current. Fig. 3.12 shows a block diagram of the proposed linear model.

The next topology modeled correspond to the Multiphase Buck

3.1.3 Model of the Multi-Phase Buck Converter

This topology is composed of an arrangement of several branches connected in parallel, fed by one source voltage. Each branch is composed of half FB, which in the middle point is connected to an inductance. The output of each branch is connected in parallel and connected to a LC load. Fig. 3.13 presents to topology.
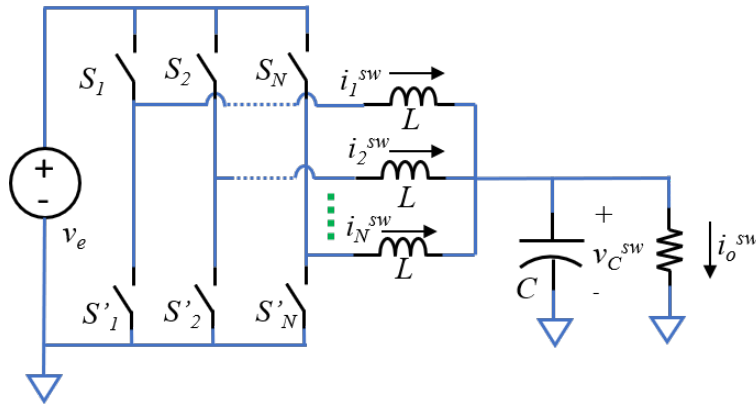
Figure 3.13: Multi-Phase Buck Converter

Where S'_k receives the opposite control signal of S_k, for $k = 1, 2, \cdots N$. The objective of this converter is to balance the currents through the inductances and to regulate the output voltage which corresponds to the voltage of the capacitor. This converter is modulated with a phase-shifted multi-carrier PWM modulation. Therefore, the carrier of the kth branch is shifted $\dfrac{360}{N}(k-1)$. According to Fig. 3.13, the voltage of the inductance of the kth branch follows:
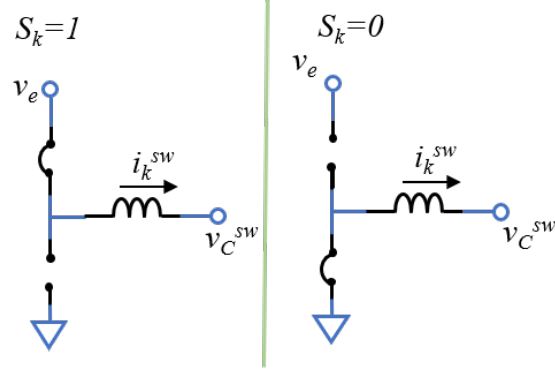
Figure 3.14: States of the Multi-Phase Buck Converter

Hence, the switching dynamical model of the current of the inductance of the kth branch is:

$$L\dot{i}_k^{sw} = v_e S_k - v_C^{sw} - R i_k^{sw} \tag{3.43}$$

where R is the DCR of the inductances of the branches. According to Fig. 3.13, the model of the voltage of the capacitor, v_C^{sw} is:

$$C\dot{v}_C^{sw} = \sum_{k=1}^{N} i_k^{sw} - \frac{v_C^{sw}}{R_o} \tag{3.44}$$

Obtaining the moving average of (3.43) and (3.44), it follows:

$$L\dot{i}_k = v_e d_k - v_C - R_s i_k$$
$$C\dot{v}_C = \sum_{k=1}^{N} i_k - \frac{v_C}{R_o} \tag{3.45}$$

where d_k is the duty-cycle of S_k. Expressing (3.45) as a matrix form

$$L\dot{\mathbf{I}} = v_e \mathbf{D} - v_C \mathbf{V_1} - R\mathbf{I}$$
$$C\dot{v}_C = \mathbf{V_1}^T \mathbf{I} - \frac{v_C}{R_o} \tag{3.46}$$

Fig. 3.15 presents the equivalent circuit of the the model described in (3.45)
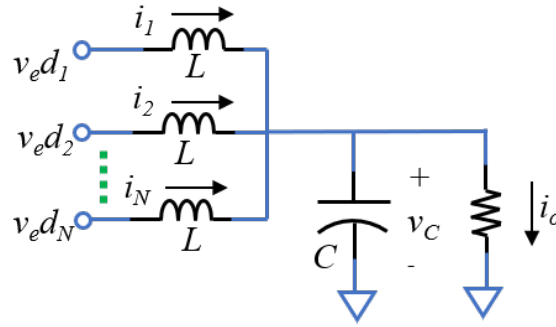
Figure 3.15: Equivalent circuit of the model of the Multi-Phase Buck Converter

It can be seen in (3.46), that the system is already linear. Hence, there is no necessary to linearize the model. Therefore, converting the model to a LAPLACE domain, it follows:

$$\mathbf{I}(s) = \frac{1}{(Ls + R)} \left(v_e \mathbf{D}(s) - V_C(s) \mathbf{V_1} \right)$$

$$V_C(s) = \frac{R_o}{(R_o Cs + 1)} \mathbf{V_1}^T \mathbf{I}$$

(3.47)

Based on (3.47), Fig. 3.16 shows the block diagram of the model:
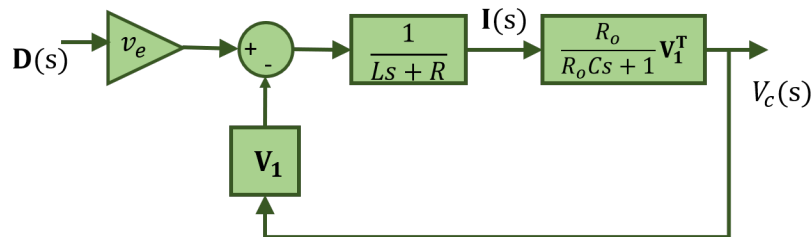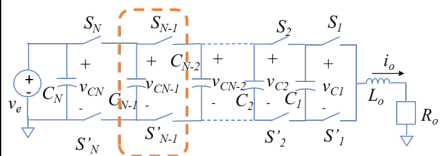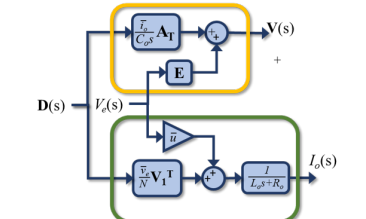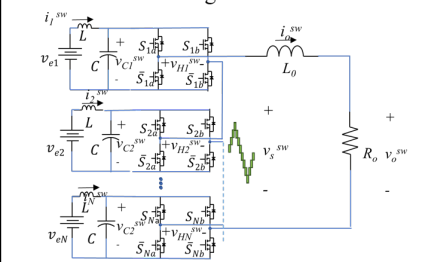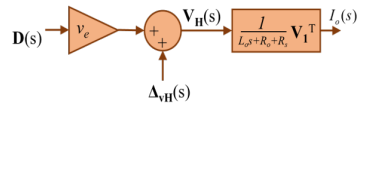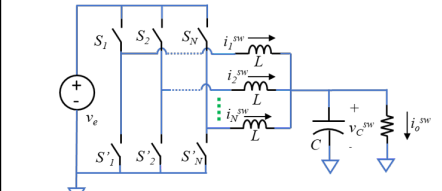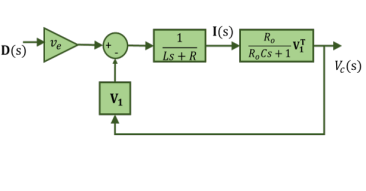
Figure 3.16: Block diagram of the Multi-Phase Buck Converter

It can be observed that the branch currents depend on the duty-cycle of its cell, while the output voltage depends on the sum of the branch currents. Based on the model of the three converters, it is possible to propose a model that involves these topologies. The next section summarizes the main aspects of the models of these topologies and proposes a generalized model.

3.2 General Model of the studied topologies

In order to present the decentralized control strategy which has been implemented with success on two different MCC topologies. To introduce this strategy using a general model of MCC is proposed. It should be noted that it is not mandatory to use the general model in practice. Table 3.1 shows the main aspects of the topologies:

Table 3.1: Summarize of the three analyzed converter

Topology	Model	Aspects
Flying-Capacitor Multilevel Converter		• CVs depend on the difference of the duty cycle of it cell and the duty cycle of its neighbors • GV depends on the sum of the duty cycles of the cells
Cascaded Full-Bridge Multilevel Converter		• CVs depend on the duty cycle of it cell • GV depends on the sum of the duty cycle or on the sum of the cell variables
Multi-Phase Buck Multilevel Converter		• CVs depend on the duty cycle of it cell and depends on the global variable • GV depends on the sum of the current of the branches

To obtain a model for the CVs, that involves these three topologies it has to take into account the three models. According to table 3.1, the model of the CV of the FCMC, receives the difference of the duty-cycles of the neigbors and the duty-cycle of its cell. For the case of the Nth cell, it receives the differences of the duty-cycle between its cell the the cell $N-1$, and in the case of the first cell, the CV depends on the difference of the duty-cycle of it cell and the cell 2. The model of the CVs of the CBBMC, receives the duty-cycle of its cell and the model of the CVs of the Multiphase Buck, receives the duty-cycle of it cell and also receives the GV. Fig. 3.17 presents a block diagram of the model of the CVs of the three topologies.
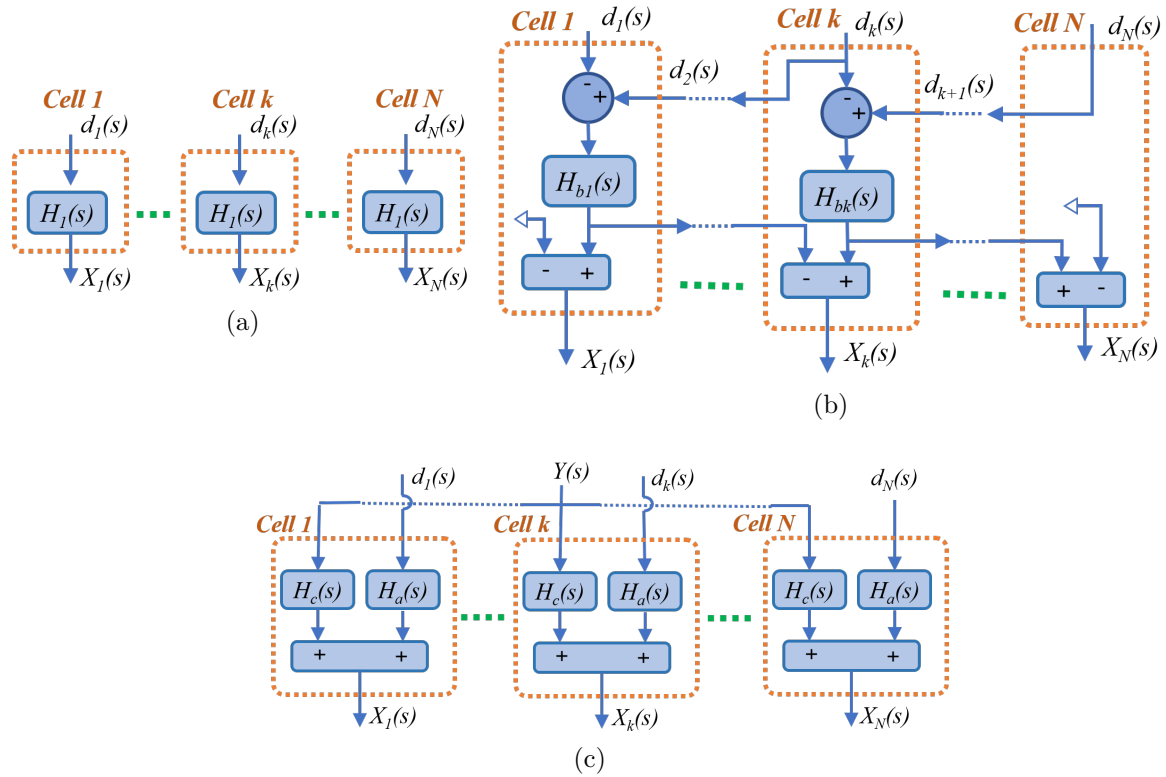
Figure 3.17: Cell structures

Based on these models, it is possible to proposes a general CV model, combining the three CV models, as Fig. 3.18 shows.
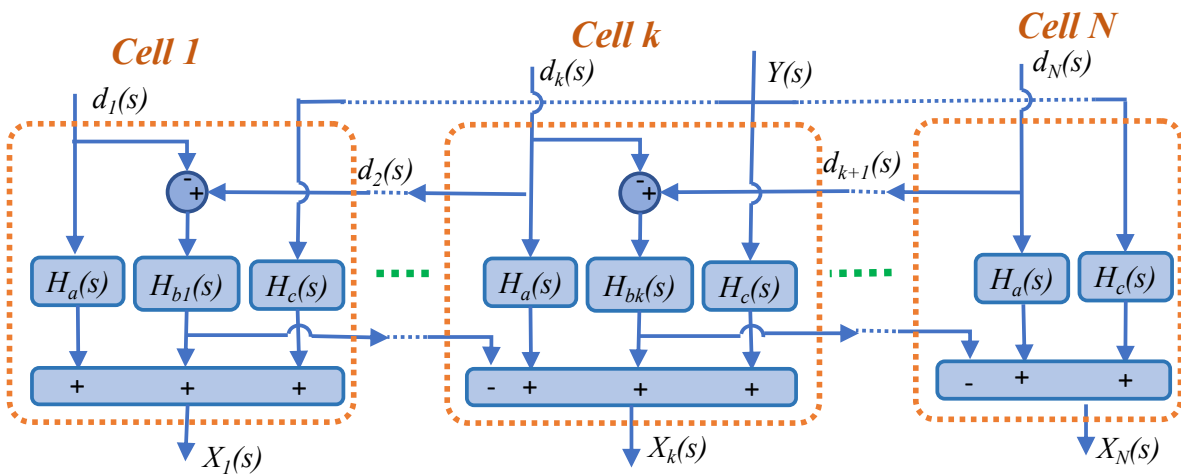
Figure 3.18: General model of the cell-variable

According to Fig. 3.18

$$X_1(s) = H_a(s)d_k(s) + H_{b1}(s)\left(d_2(s) - d_1(s)\right)$$
$$+ H_c(s)Y(s)$$

$$X_k(s) = H_a(s)d_k(s) + H_{bk}(s)\left(d_{k+1}(s) - d_k(s)\right)$$
$$- H_{bk-1}k\left(d_k - d_{k-1}\right) + H_c(s)Y(s) \quad , \; k = \{2, \, 3, \cdots, N\} \tag{3.48}$$

$$X_N(s) = H_c(s)Y(s) + H_a(s)d_N(s)$$
$$+ H_{bN-1}(s)\left(d_N(s) - d_{N-1}(s)\right)$$

Expressing as a matrix form, it follows:

$$\mathbf{X}(s) = \left(H_a(s)\mathbb{I} + \mathbf{H_B}(s)\right)\mathbf{D}(s) + H_c(s)Y(s)\mathbf{V_1} \tag{3.49}$$

where $\mathbf{X}(s) = \begin{bmatrix} X_1(s) & X_2(s) & \cdots & X_N(s) \end{bmatrix}^T$, $\mathbb{I}$ is the identity matrix of N dimension and

$$\mathbf{H_B}(s) = \begin{bmatrix} -H_{b1}(s) & H_{b1}(s) & 0 & \cdots & 0 \\ H_{b1}(s) & -(H_{b1}(s) + H_{b2}(s)) & H_{b2}(s) & \ddots & \vdots \\ 0 & H_{b2}(s) & \ddots & \ddots & 0 \\ \vdots & \ddots & \ddots & -(H_{bN-2}(s) + H_{bN-1}(s)) & H_{bN-1}(s) \\ 0 & \cdots & 0 & H_{bN-1}(s) & -H_{bN-1}(s) \end{bmatrix}$$

It has to mention that according to [53, 54], $-\mathbf{H_B}(s)$ represents the Laplacian matrix of a graph because the sum of the elements of each row is equal to 0, as same as the sum of the elements of each column, producing one eigenvalue equals to 0 and the other ones all greater than 0 or all lower than 0. This information must be taken into account for balancing the CV. Table 3.2 shows the expressions of $H_a(s)$, $\mathbf{H_B}$ and $H_c(s)$ according to the topology.

Table 3.2: Transfer functions of the model of the CVs according to the topology

Topology	$H_a(s)$	$\mathbf{H_B}(s)$	$H_c(s)$
Flying-Capacitor Multilevel Converter	0	$\dfrac{\bar{i_o}}{s}\mathbf{A_T}$	0
Cacaded Full-Bridge Multilevel Converter	v_e	0	0
Multi-Phase Buck Converter	$\dfrac{v_e}{Ls+R}$	0	$-\dfrac{1}{Ls+R}$

Analogously with the CVs, to model the GV it has to take into account the three models. Based on table 3.1, the GV model of the FCMC depends on the sum of the duty-cycles, while the GV model of the Multi-phase Buck depends on the sum of the CVs. The GV model of the CFBMC has two options, which can depend on the sum of the CVs or the sum of the duty-cycles. Fig. 3.19 describes the model of the GV of these topologies.
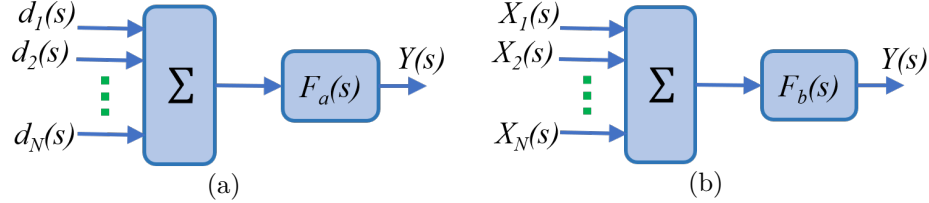
Figure 3.19: Models of the GVs of the converters

Hence, the GV of the CFBMC, $I_o(s)$, is modeled as 3.39, the GV of the Multi-Phase Buck, $V_c(s)$, is modeled as 3.19(b) while the GV of the FBMC, $I_o(s)$ can be modeled by both. Combining the two models, it follows:
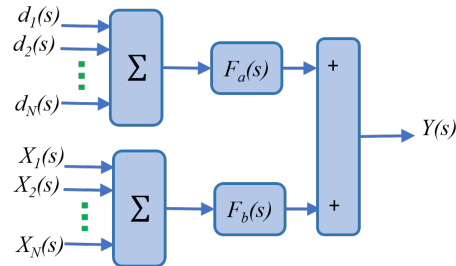
Figure 3.20: General model of the global variable

According to 3.20 the general model of the GV is:

$$Y(s) = F_a(s)\sum_{k=1}^{N} d_k(s) + F_b(s)\sum_{k=1}^{N} X_k(s) \qquad (3.50)$$

expressing as a matrix form:

$$Y(s) = F_a(s)\mathbf{V_1}^T\mathbf{D}(s) + F_b(s)\mathbf{V_1}^T\mathbf{X}(s) \tag{3.51}$$

Table shows the value of $H_a(s)$, $\mathbf{H_B}$ and $H_c(s)$ according to the topology.

Table 3.3: Transfer Functions of the model of the GV according to the topology

Topology	$F_a(s)$	$F_b(s)$
Flying-Capacitor Multilevel Converter	$\dfrac{\overline{v}_e}{L_o + R_o}$	0
Cacaded Full-Bridge Multilevel Converter	v_e	0
Multi-Phase Buck Converter	0	$\dfrac{R_o}{R_o LC + 1}$

Eq. (3.49) and (3.51) shows the proposed generalized models of the CV and the GV respectively. Now, inserting (3.49) in (3.51) and leaving $Y(s)$ expressed only as a function of $\mathbf{D}(s)$ it follows:

$$Y(s) = \underbrace{F_a(s)\mathbf{V_1}^T\mathbf{D}(s) + F_b(s)H_a(s)\mathbf{V_1}^T\mathbf{D}(s)}_{M_1(s)} + \underbrace{F_b(s)\mathbf{V_1}^T\mathbf{H_B}(s)\mathbf{D}(s)}_{M_2(s)}$$
$$+ \underbrace{F_b(s)H_c(s)\mathbf{V_1}^T\mathbf{V_1}Y(s)}_{M_3(s)} \tag{3.52}$$

$M_2(s)$ can be expressed as its transposed. Hence:

$$M_2(s) = F_b(s)H_c(s)\mathbf{D}^T(s)\mathbf{H_B}^T\mathbf{V_1} \tag{3.53}$$

$\mathbf{H_B}(s)^T\mathbf{V_1}$ corresponds to the sum of the elements to each row of $\mathbf{H_B}(s)^T$, meaning the sums of the the elements of each column of $\mathbf{H_B}(s)$ which are equals to 0. Hence, $\mathbf{H_B}^T\mathbf{V_1} = \mathbf{0}$, where $\mathbf{0} = \begin{bmatrix} 0 & 0 & \dots & 0 \end{bmatrix}^T$. Consequently $M_2(s) = 0$.

$M_3(s)$ presents a dot product of $\mathbf{V_1}$, producing that $M_3(s) = NF_b(s)H_c(s)$.

Based on the simplifications explained before, it follows:

$$Y(s) = \left(F_a(s) + F_b(s)H_a(s) \right) \mathbf{V_1}^T\mathbf{D}(s) + NF_b(s)H_c(s)Y(s) \tag{3.54}$$

Solving $Y(s)$:

$$Y(s) = \underbrace{\frac{F_a(s) + F_b(s)H_a(s)}{1 - NF_b(s)H_c(s)}}_{G_{GV}(s)}\mathbf{V_1}^T\mathbf{D}(s) \tag{3.55}$$

Notice that (3.55) represents $Y(s)$ only as a function of the sum of the inputs. It means that for $Y(s)$ the action of the difference between neighbors is canceled. $G_{GV}(s)$ is the transfer function of the GV model.

In order to obtain the model of the CV, (3.55) is inserted in (3.49):

$$\mathbf{X}(s) = \left(\underbrace{H_a(s)\mathbb{I}}_{\substack{contribution \\ of \\ itself}} + \underbrace{\mathbf{H_B}(s)}_{\substack{contribution \\ of \\ neighbors}} + \underbrace{H_c(s)\frac{F_a(s) + F_b(s)H_a(s)}{1 - NF_b(s)H_c(s)}\mathbf{V_1}\mathbf{V_1}^T}_{contribution\ of\ the\ output\ variable} \right) \mathbf{D}(s) \quad (3.56)$$

$$\underbrace{}_{\mathbf{G_{CV}}(s)}$$

It can clearly observed the contribution of the duty cycle of it cell, the contribution of the duty cycle of the neighbors cells and the contribution of the GV, that is a function of the sum of all the duty cycles. $G_{CV}(s)$ is the transfer function of the CV model.

Eq. (3.55) and (3.56) represent the proposed linear model of any symmetric MCC. Fig. 3.21 shows the sensitized block diagram of (3.55) and (3.56).
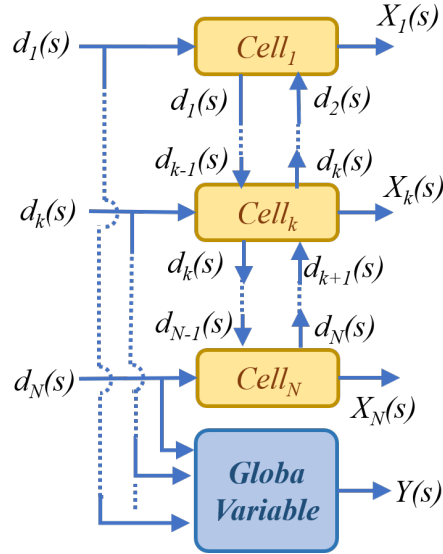
Figure 3.21: Synthesized model of a Symmetric MCC

Based on this general model the decentralized control method is proposed.

3.3 Design of the decentralized control method

The proposed control strategy, presented here, corresponds to a decentralized control method that can be used for any type of MCC topology that can be modeled as (3.55)

and (3.56). Fig. 3.22 shows the diagram of the three studied MCCs with the control method to be designed
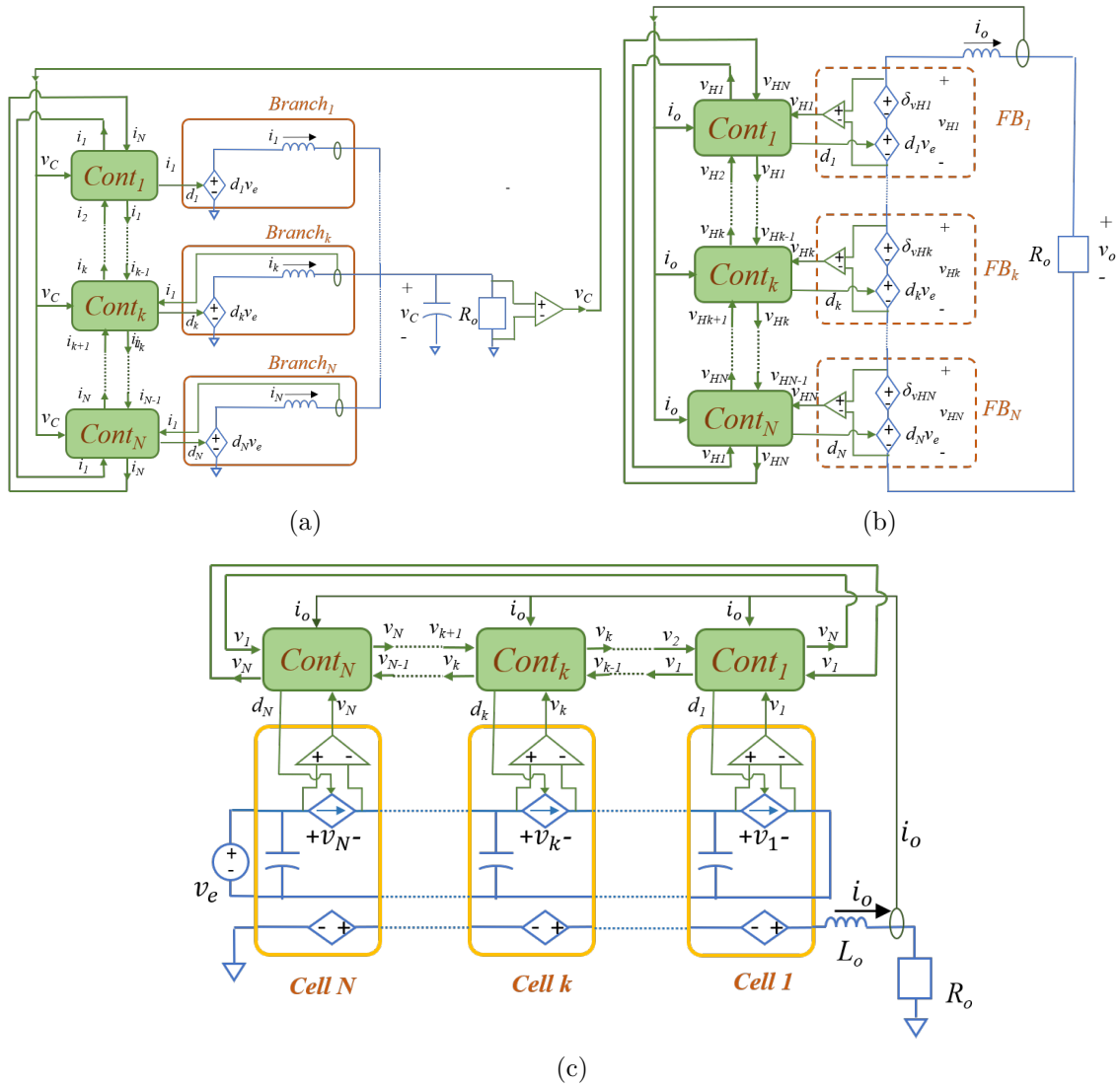
Figure 3.22: Control strategy with the studied topologies. (a) Control Method with the Multi-Phase Buck, (b) Control Method with the Cascaded Full-Bridge Multilevel Converter, (c) Control method with the Flying-Capacitor Multilevel Converter

This control method has to implement three main functions which are: To balance the CVs, to regulate the GV and to give a straightforward ability to insert or remove cells during operation. Fig. 3.23 shows a block diagram of the synthesized model of the MCC model with the proposed decentralized controller.
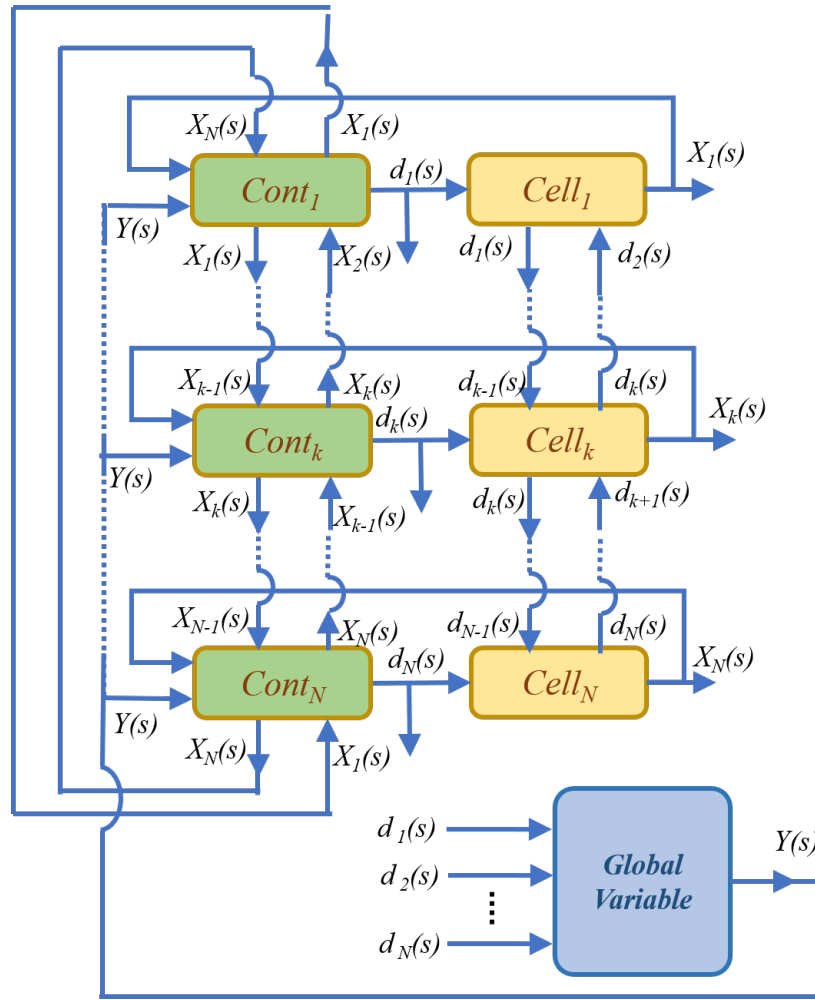
Figure 3.23: Block diagram of the synthesized model of the MCC with the decentralized controller

As Fig. 3.23 shows, the control receives its CV, the CVs of its neighbors and GV for being regulated. For the case of the cell 1 the controller receives the CV from the cell 2 and the cell N, while the cell N receives the CV from the cell $N-1$ and the cell 1, closing the circular chain. The control method is composed of three stages: The bypass system, the balancing controller and the GV regulator. Fig. 3.24 shows a block diagram of the proposed control method.
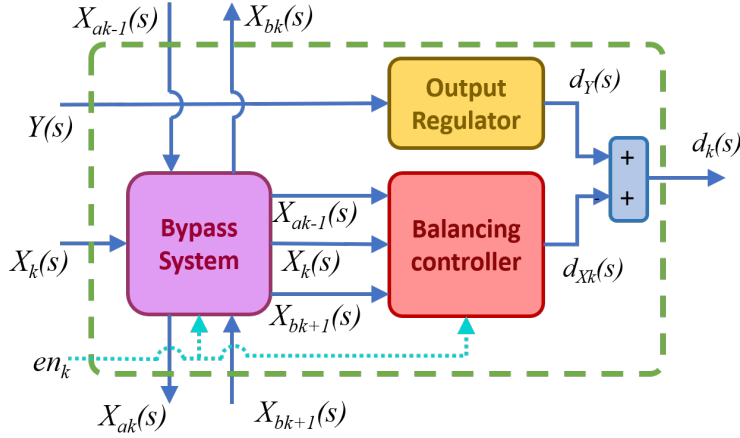
Figure 3.24: Block diagram of the local controller

The bypass system provides the MCC the ability to work if a cell is inserted or removed without being interrupted. This capability allows the converter to manage the number of active cells during operation; to increase the available power during operation, increasing the cell number for instance or to reconfigure the topology in case of fault occurrence. Fig. 3.25 shows the block diagram of the bypass system
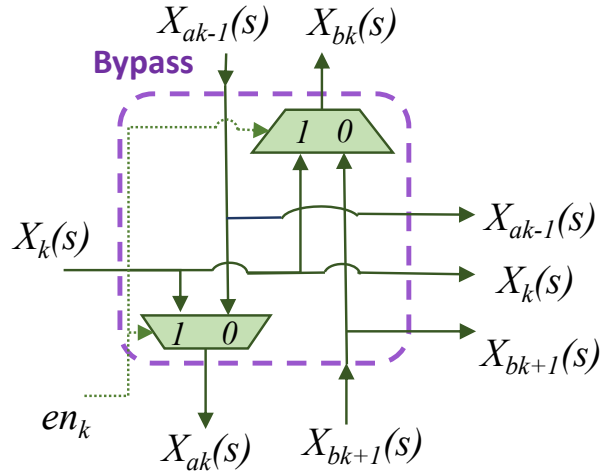
Figure 3.25: Structure of the Bypass System

According to Fig. 3.25 the bypass system of the kth cell depends on an enable signal en_k, where if the $en_k = 1$, the cell is active and the bypass system sends to its neighbors the value of its own cell-variable ($X_k(s)$). If $en_k = 0$, the cell is not available and the bypass system sends the to the cell $k+1$, the value received by the cell $k-1$. Similarly, the bypass system sends to the cell $k-1$ the value received by the cell $k+1$. According to Fig. 3.23, for cells 1 and N, the controller closes the circular chain sending $X_N(s)$ to cell 1 and $X_1(s)$ to cell N. Eq. 3.57 shows as an analytic function the bypass system

operation.

$$\begin{bmatrix} X_{a_k} \\ X_{b_k} \end{bmatrix} = \begin{cases} \begin{bmatrix} X_k \\ X_k \end{bmatrix} ; en_k = 1 \\ \begin{bmatrix} X_{a_{k-1}} \\ X_{b_{k+1}} \end{bmatrix} ; en_k = 0 \end{cases} \tag{3.57}$$

The next stage of the control method is the balancing controller, that compares the cell-variables sent from the neighbors with the local cell-variable. Then, this error is canceled using a local controller. Fig. 3.26 shows the block diagram of the balancing control.
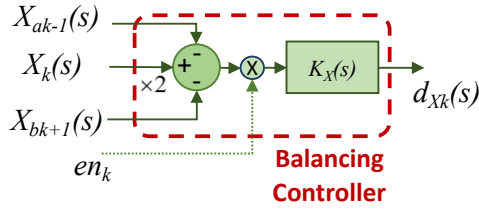
Figure 3.26: Block Diagram of the Balancing Controller

According to Fig. 3.26, if all the N cells are available:

$$d_{X_k}(s) = \begin{cases} K_X(s)\left(2X_1(s) - X_2(s) - X_N(s)\right) \\ K_X(s)\left(2X_k(s) - X_{k+1}(s) - X_{k-1}(s)\right) & ; k = \{2 \quad 3 \quad \cdots \quad N-1\} \\ K_X(s)\left(2X_N(s) - X_1(s) - X_{N-1}(s)\right) \end{cases} \tag{3.58}$$

The last stage of the control method corresponds to the GV regulator. Fig. 3.27 shows the block diagram of this stage.
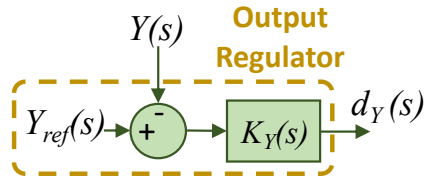
Figure 3.27: Block diagram of the GV regulator

This regulator is a classical one, that compares the output variable with a reference and compensates the error. According to Fig. 3.27, it follows:

$$d_Y(s) = K_Y(s)\left(Y_{ref}(s) - Y(s)\right) \tag{3.59}$$

Based on the three stages, the entire block diagram of the control method is:
Based on Fig. 3.28

$$d_k(s) = d_Y(s) + d_{X_k}(s) \tag{3.60}$$
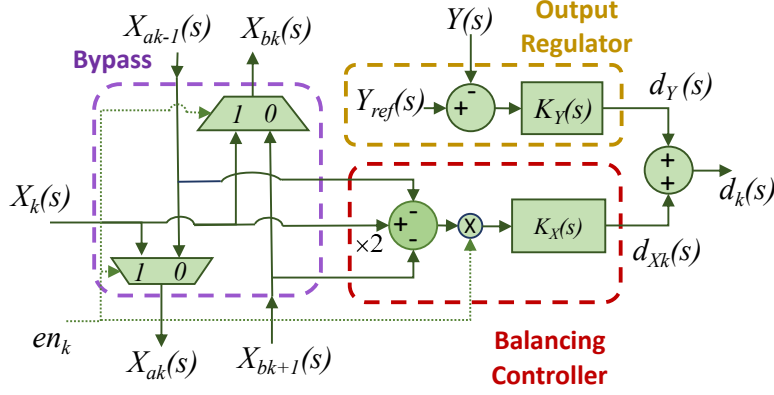
Figure 3.28: Detailed Block Diagram of the Controller

Replacing (3.58) and (3.59) in (3.60) it follows:

$$d_k(s) = K_Y(s)\left(Y_{ref}(s) - Y(s)\right) + K_X(s)\left(2X_k(s) - X_{k+1}(s) - X_{k-1}(s)\right) \qquad (3.61)$$

Equation (3.61) expresses the duty-cycle of each cell. Expressing 3.61 as a matrix form, it follows:

$$\mathbf{D}(s) = K_X(s)\mathbf{D_{iff}}\mathbf{X}(s) + K_Y(s)\left(Y_{ref}(s) - Y(s)\right)\mathbf{V_1} \qquad (3.62)$$

$$\text{where } \mathbf{D_{iff}} = \begin{bmatrix} 2 & -1 & 0 & \dots & -1 \\ -1 & 2 & -1 & \ddots & \vdots \\ 0 & \ddots & \ddots & \ddots & 0 \\ \vdots & \ddots & -1 & 2 & -1 \\ -1 & \dots & 0 & -1 & 2 \end{bmatrix}$$

The matrix $\mathbf{D_{iff}}$ represents the several connections for communication between the N local controllers. Notice that in $\mathbf{D_{iff}}$ the sum of the elements of each column are equals to 0, alike the sum of the elements of each row. It confirms that $\mathbf{D_{iff}}$ is a graphs as matrix $\mathbf{H_B}(s)$.

Equation (3.61) represents the main strategy for any MCC to implement a decentralized balancing controller. In the next section, the controller is inserted into the general model and the closed-loop system is analyzed

3.4   Analysis of the Closed-loop

This section analyzes the generalized model of a MCC with the proposed decentralized control method. This is done, inserting the proposed control law defined in the general model. Fig. 3.29 shows a block diagram of the closed loop.
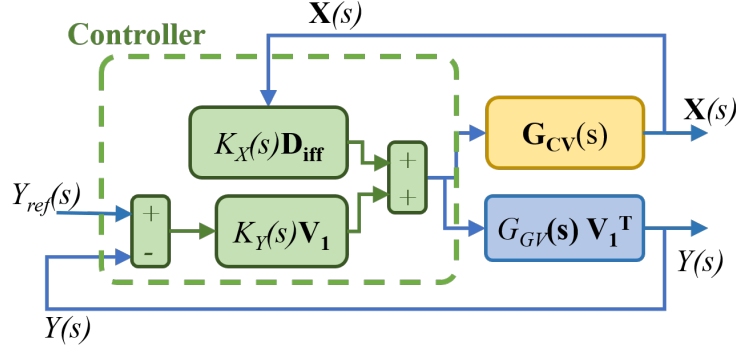
Figure 3.29: Closed-loop diagram of the generalized model

Inserting (3.62) in the GV regulator model of the MCC defined in (3.55) it follows:

$$
\begin{aligned}
Y(s) = & \frac{F_a(s) + F_b(s)H_a(s)}{1 - NF_b(s)H_c(s)} K_X(s) \underbrace{\left(\mathbf{V_1}^T \mathbf{D_{iff}} \mathbf{X}(s)\right)}_{M_4(s)} \\
& + \frac{F_a(s) + F_b(s)H_a(s)}{1 - NF_b(s)H_c(s)} K_Y(s) \left(Y_{ref}(s) - Y(s)\right) \mathbf{V_1}^T \mathbf{V_1}
\end{aligned}
\tag{3.63}
$$

As $M_2(s) = 0$ because of $\mathbf{H_B}(s)$ is a graph, $M_4(s) = 0$ because of $\mathbf{D_{iff}}$ is also a graph and the sum of each of its columns and its rows are equal to 0. Furthermore, $\mathbf{V_1}^T \mathbf{V_1} = N$. Hence, Openning the feedback of $Y(s)$
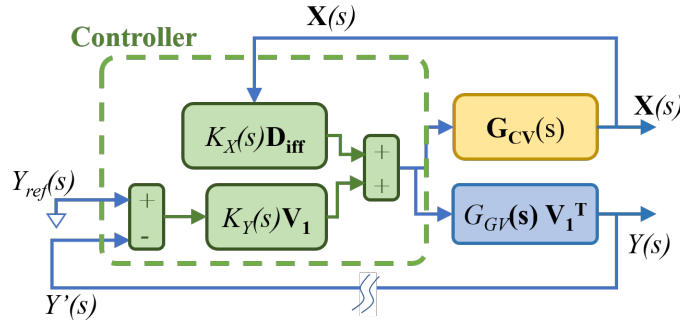
Figure 3.30: Closed-loop diagram of the generalized model, opening the loop of the GV

$$
Y(s) = \underbrace{-NK_Y(s) \left(\frac{F_a(s) + F_b(s)H_a(s)}{1 - NF_b(s)H_c(s)}\right)}_{F_{ol_Y}(s)} \left(Y'(s) - Y_{ref}(s)\right)
\tag{3.64}
$$

where $Y'(s)$ is the sensed variable of $Y(s)$, and $F_{ol_Y}(s)$ represents the open-loop transfer function of the GV regulator. Notice that concerning the GV the contribution of the

balancing controller is canceled, and just depends on the GV regulator. It means that for any differential disturbances produced in the CV, the GV is not affected.

The design of $K_Y(s)$ depends on the transfer functions of the MCC that are linked to the topology of the converter to be controlled.

Analogously as the insertion of the controller to the GV model, (3.65) shows the insertion of the controller to the CV model.

$$
\begin{aligned}
\mathbf{X}(s) =\ & K_X(s)\left(H_a(s)\mathbb{I} + \mathbf{H_B}(s)\right)\mathbf{D_{iff}}\mathbf{X}(s) \\
& + K_X(s)H_c(s)\frac{F_a(s) + F_b(s)H_a(s)}{1 - NF_b(s)H_c(s)}\mathbf{V_1}\mathbf{V_1}^T\mathbf{D_{iff}}\overset{0}{\mathbf{X}(s)} \\
& + K_Y(s)\left(H_a(s)\mathbf{V_1} + \mathbf{H_B}\mathbf{V_1}\right)^0(Y_{ref}(s) - Y(s)) \\
& + K_Y(s)H_c(s)\frac{F_a(s) + F_b(s)H_a(s)}{1 - NF_b(s)H_c(s)}\mathbf{V_1}\mathbf{V_1}^T\mathbf{V_1}^N(Y_{ref}(s) - Y(s))
\end{aligned}
\tag{3.65}
$$

Opening the feedback of $\mathbf{X}(s)$, it follows:
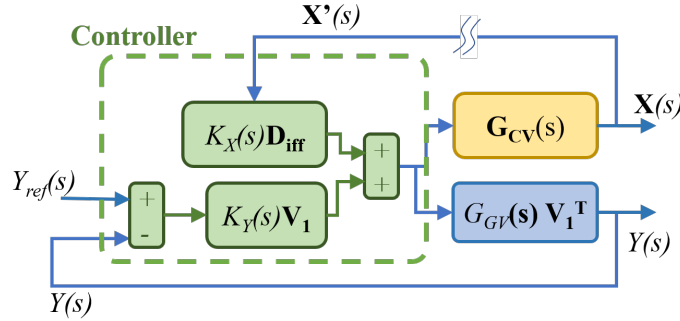
Figure 3.31: Closed-loop diagram of the generalized model, opening the loop of the CVs

Hence, (3.65) leads to:

$$
\begin{aligned}
\mathbf{X}(s) =\ & \underbrace{K_X(s)\left(H_a(s)\mathbb{I} + \mathbf{H_B}(s)\right)\mathbf{D_{iff}}}_{\mathbf{F_{olx}}(s)} \mathbf{X}'(s) \\
& + K_Y(s)\left(H_a(s) + NH_c(s)\frac{F_a(s) + F_b(s)H_a(s)}{1 - NF_b(s)H_c(s)}\right)\mathbf{V_1}\left(Y_{ref}(s) - Y(s)\right)
\end{aligned}
\tag{3.66}
$$

where $\mathbf{X}'(s)$ is the sensed variable of $\mathbf{X}(s)$. Notice that inserting the control law, the CV model depends on the balancing control and the GV regulator. However, the balancing control only compensates the sensed CV ($\mathbf{X}(s)$), while the GV regulator acts over the sensed GV. It is valid to mention that the open-loop transfer function of the CV model ($\mathbf{F_{olx}}(s)$) is a product between a graph ($\mathbf{D_{iff}}$) and a linear combination of

a graph ($\mathbf{H_B}(s)$) and the identity matrix. It is simple to prove that this product is also a graph or a graph multiplied by -1, as Appendix B explains. Because of that, one of its eigenvalues is equal to 0. Graph theory is explained in more details in [53, 54]. Furthermore, graph theory indicates that the steady-state of a dynamical system represented by a graph Laplacian is the average of the initial condition of the states. Hence, according to (3.66) the first part of the controller balances the cells, and the second stage fixes the trajectory of the CVs. Also, it can be seen that it is not necessary that $\mathbf{H_B}(s)$ has the form expressed in (3.49) because all the computations are developed assuming that $\mathbf{H_B}(s)$ is a Laplacian of a graph, without care the form. Consequently, if a MCC has a model represented as a linear combination between an identity matrix and a Laplacian of a graph in the CV model, the proposed control method works.

The design of the balancing controller and its gains are based on the modal response of $\mathbf{F_{olx}}(s)$ that depends on $H_a(s)$ and $\mathbf{H_B}(s)$. These transfer functions are obtained based on the topology of the MCC.

In order to prove this control method, it is applied in the Flying -Capacitor Multilevel Converter and the Cascaded Full-Bridge Multilevel Converter modeled previously.

3.5 Control method applied in the Flying-Capacitor Multilevel Converter

For the FCMC, the CV, $X_k(s)$ corresponds the the cell-voltage, $V_k(s)$ and the GV, $Y(s)$, corresponds to $I_o(s)$, $K_V(s)$ is $K_X(s)$ and $K_{i_o}(s)$ is $K_Y(s)$. Hence, according to (3.61), the control method applied to this topology is described as:

$$d_k(s) = K_V(s)\left(-V_{k-1} + 2V_k(s) - V_{k+1}\right) + K_{i_o}(s)\left(I_{ref}(s) - I'_o(s)\right) \tag{3.67}$$

Expressing the controller as a matrix form:

$$\mathbf{D}(s) = K_V(s)\mathbf{D_{iff}}\mathbf{V} + K_{i_o}(s)\left(I_{ref}(s) - I_o(s)\right)\mathbf{V_1} \tag{3.68}$$

Based on table 3.2, table 3.3, (3.66) and (3.64) the model of the CFBMC with the proposed control method is:

$$\mathbf{V}(s) = \underbrace{K_V(s)\frac{\bar{i}_o}{C_o s}\mathbf{A_T}\mathbf{D_{iff}}}_{\mathbf{F_{olV}}(s)}\mathbf{V}'(s) + \mathbf{E}V_e(s) \tag{3.69a}$$

$$I_o(s) = \underbrace{K_{i_o}(s)\overbrace{\frac{\bar{v}_e}{L_o s + R_o}}^{G(s)}}_{F_{ol_{io}}(s)}\left(I_{ref}(s) - I'_o(s)\right) + \frac{u_o}{L_o s + R_o}V_e(s) \tag{3.69b}$$

Notice that because of $H_a(s)$ and $H_c(s)$ are equal to 0, $K_Y(s)$ does not affect the cell model, decoupling the cell-voltage from the output current. Furthermore, the GV regulator does not affect the cell-voltage. About the output current model, as it is demonstrated in subsection 3.3, the proposed control law decouples the GV from the CV. For these reasons, it is possible to affirm that in the linear model of the Flying-Capacitor Multilevel Converter, the CVs and the GV are completely decoupled between them. Hence, theoretically, a disturbance in CVs does not affect the GV and vice versa. This effect allows the design of the controller $K_{i_o}(s)$ regardless of the behavior of the cell-voltage loop and $K_V(s)$ without caring about the output current loop.

The design of the GV regulator is based on the bode analysis of the open-loop transfer function of the GV ($F_{ol_{i_o}}$), which depends on the topology $G(s)$ and the GV regulator $K_{i_o}(s)$. In this study the proposed controller for the GV is a PI controller. Hence:
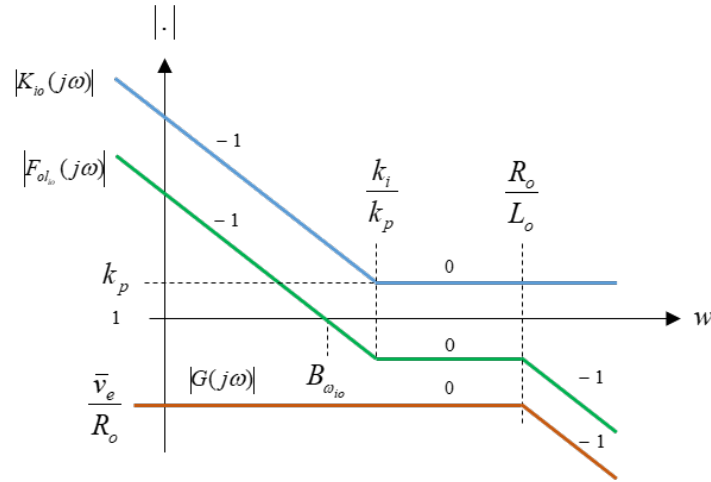
Figure 3.32: Bode diagram of $G(s)$, $K_V(s)$ and $F_{olio}(s)$

Where the $B\omega_{i_o}$ is the bandwidth of the output current loop. Based on the bode diagram:

$$B\omega_{i_o} = \frac{k_i \bar{v}_e}{R_o} \tag{3.70}$$

The bandwidth of the system should be less than 10 times the switching frequency.

3.5.1 Modal Analysis of the Balancing Controller

To synthesizes the balancing controller it is necessary to analyze the modal responses of the open-loop transfer function of the cell-voltages $\mathbf{F_{olv}}(s)$. Hence:

$$\mathbf{F_{olv}}(s) = \frac{\bar{i}_o}{C_o s} K_V(s) \underbrace{\mathbf{A_T D_{iff}}}_{\mathbf{V_{eig} \Lambda V_{eig}^{-1}}} \tag{3.71}$$

where $\mathbf{\Lambda}$ is the Diagonal matrix of $\mathbf{A_T D_{iff}}$. It should be noted that one eigenvalue of $\mathbf{A_T D_{diff}}$ is equal to 0, because it is a Laplacian of a graph

$$\mathbf{\Lambda} = \begin{bmatrix} \lambda_1 & 0 & \dots & 0 \\ 0 & \lambda_2 & \ddots & \vdots \\ \vdots & \ddots & \ddots & 0 \\ 0 & \dots & 0 & \lambda_N \end{bmatrix} ; \lambda_1 = 0 \tag{3.72}$$

Therefore,

$$\mathbf{F_{olv}}(s) = \mathbf{V_{eig}} \underbrace{K_V(s) \frac{\bar{i}_o}{C_o s} \mathbf{\Lambda}}_{\mathbf{\Pi}(s)} \mathbf{V_{eig}^{-1}} \tag{3.73}$$

$\mathbf{\Pi}(s)$ represents the open-loop transfer function of the modal response, defined as:

$$\mathbf{\Pi}(s) = K_V(s) \begin{bmatrix} p_1(s) & 0 & \dots & 0 \\ 0 & p_2(s) & \ddots & \vdots \\ \vdots & \ddots & \ddots & 0 \\ 0 & \dots & 0 & p_N(s) \end{bmatrix} \tag{3.74}$$

and $p_k(s)$ is defined as:

$$p_k(s) = \frac{\bar{i}_o \lambda_k}{C_o s} \tag{3.75}$$

Hence the open-loop transfer function of the kth mode is:

$$F_{olm_k}(s) = K_V(s) p_k(s) \tag{3.76}$$

The controller is designed to ensure stability to all the open-loop transfer functions of the modes, using the bode diagram $p_k(s)$, $K_V(s)$ and $F_{olm_k}(s)$. Because of all the $F_{olm_k}(s)$s present an integrator, the chosen controller could be a Proportional controller. However, due to the resistivity losses in serial and parallel in the capacitors, a PI controller is the best option for $K_V(s)$. Based on (3.69a), $\mathbf{\Pi}(s)$ depends on $\mathbf{A_T}$, that depends on the capacitance values. Hence, the eigenvalues λ_k depend on the value of the capacitor. Based on the eigenvectors and eigenvalues, and taking into account
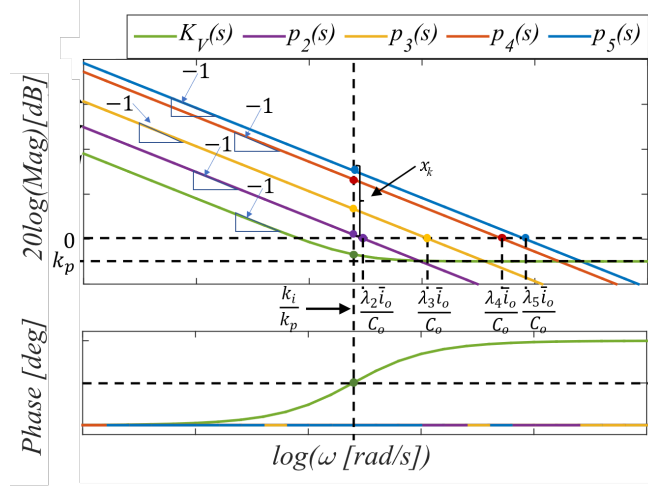
Figure 3.33: Bode diagram of $K_V(s)$ and $p_k(s)$

that the proposed controller is a PI, Fig. 3.33 shows the Bode diagram of the transfer functions $p_k(s)$ for k={2 ... 5} and $K_V(s)$, where $p_1(s) = 0$ because $\lambda_1 = 0$.

The points x_k presented in $|p_k(j\omega)|$, is solved in (3.77), corresponding to the magnitude at $\omega = \dfrac{k_i}{k_p}$, that corresponds to the zero of the PI controller, $K_V(s)$.

$$x_k = \frac{\lambda_k \bar{i}_o k_p}{C_o k_i} \tag{3.77}$$

Knowing the values of x_k, Fig. 3.34 shows the bode diagram of the open-loop transfer function of each mode, $F_{olm_k}(s)$
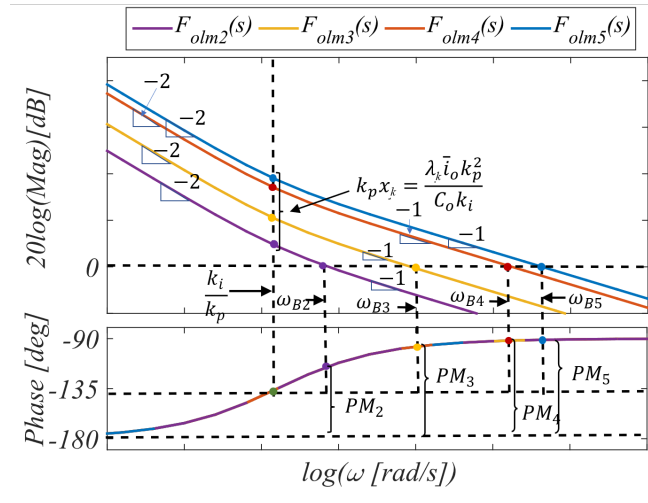
Figure 3.34: Bode diagram of the open-loop transfer functions of the modes

Finally, the proportional gain of the balancing controller is:

$$\frac{\lambda_k \bar{i}_o k_p^2}{C_o k_i} = \frac{\omega_{Bk} k_p}{k_i} \tag{3.78a}$$

$$k_p = \frac{\omega_{Bmax} C_o}{\lambda_{max} \bar{i}_o} \tag{3.78b}$$

where ω_{Bmax} represents the bandwidth of the fastest mode, which corresponds to the highest λ_k, which is λ_{max}. The criterion applied to dimension the gains is that the fastest modal response must have a bandwidth 50 times less than the switching frequency f_{sw}.

$$k_p = \frac{2\pi f_{sw} C_o}{50\lambda_{max} \bar{i}_o} \tag{3.79}$$

It should be mentioned that this analysis is based on the linear model, ensuring the stability around the operation point. However, it is possible to demonstrate that the converter with the control method is stable according to Lyapunov, as shown in Appendix C.

In order to validate the proposed theory for this topology, two cases are analyzed. The first one corresponds to the case when all the values of the capacitance are identical, and the second one consists of a specific arrangement of values of the capacitance adopted in the real prototype.

3.5.2 Results

The results presented in this subsection correspond to the modal analysis of the two cases. Additionally, simulation and experimental results for the second case. Both, simulation and experimental results are provided for three different types of transent responses. The first one corresponds to a disturbance in the load, the second one is a disturbance in the input voltage and the last test describes the insertion of a cell during operation. All the results are developed with the parameters of the real prototype, implemented in the laboratory, described in table 3.4.

Table 3.4: Parameters of the Flying Cap

Parameters	Value
Number of Cells (N)	5
Input Voltage (v_e)	450 V to 3.5 kV
Nominal power	10kW - 50 kW
Switching frequency (fsw)	10 kHz
Capacitance C_o	21 μF
Output inductance L_o)	200 μH
Output Resistance (R_o)	18.75 Ω
Load Current ($\bar{i}_o$)	15 A

3.5.2.1 Modal response of the first case

The first case analyzes the modal respond corresponding to the Flying-Capacitor Multilevel Converter when all the capacitors have the same capacitance, $C_1 = C_2 = \ldots = C_N = C_o$. Hence:

$$\mathbf{A_T D_{iff}} = \begin{bmatrix} -3 & 3 & -1 & 0 & 1 \\ 4 & -6 & 4 & -1 & -1 \\ -1 & 4 & -6 & 4 & -1 \\ -1 & -1 & 4 & -6 & 4 \\ 1 & 0 & -1 & 3 & -3 \end{bmatrix} \tag{3.80}$$

Obtaining the diagonal matrix and the eigenvectors:

$$\mathbf{\Lambda} = \begin{bmatrix} 0 & 0 & 0 & 0 & 0 \\ 0 & -0.59 & 0 & 0 & 0 \\ 0 & 0 & -1.91 & 0 & 0 \\ 0 & 0 & 0 & -8.41 & 0 \\ 0 & 0 & 0 & 0 & -13.09 \end{bmatrix} \tag{3.81a}$$

$$\mathbf{V_{eig}} = \underbrace{\begin{bmatrix} -1.00 \\ -1.00 \\ -1.00 \\ -1.00 \\ -1.00 \end{bmatrix}}_{\mathbf{V_{eig}}(\lambda_1)} \underbrace{\begin{matrix} -1.05 \\ -1.19 \\ 0.00 \\ 1.19 \\ 1.05 \end{matrix}}_{\mathbf{V_{eig}}(\lambda_2)} \underbrace{\begin{matrix} 1.14 \\ -0.44 \\ -1.41 \\ -0.44 \\ 1.14 \end{matrix}}_{\mathbf{V_{eig}}(\lambda_3)} \underbrace{\begin{matrix} 0.89 \\ -1.31 \\ 0.00 \\ 1.31 \\ -0.89 \end{matrix}}_{\mathbf{V_{eig}}(\lambda_4)} \underbrace{\begin{matrix} 0.44 \\ -1.14 \\ 1.41 \\ -1.14 \\ 0.44 \end{matrix}}_{\mathbf{V_{eig}}(\lambda_5)} \tag{3.81b}$$

It can be seen that the eigenvalue related to the common mode is equal to 0. Then, in steady-state, the average values of the cell-voltages are all equals.

Based on these parameters, the gains of the controllers are defined as:

$$k_p = 1.32 \times 10^{-4} V^{-1} \tag{3.82a}$$

$$k_i = 80 V^{-1} s^{-1} \tag{3.82b}$$

Using the computed gains it is possible to validate in simulation the response of each separate mode, initializing the cell voltages with one of the eigenvectors. It produces that only the mode related to this eigenvector acts, observing that the system decreases exponentially as a first order system. Then, it is possible to obtain the time constants of each mode by the simulations, and compare these values with the theoretical ones. The obtention of the time constant in simulation assumes that each mode behaves as a 1st order low-pass filter. Thus, the kth time constant is evaluated at the level $\mathbf{\Delta V_{mod}}(\tau_k) = 63\% \mathbf{V_{eig}}(\lambda_k)$. Next, it is compared to the theoretical value, i.e. $\tau_k = \frac{1}{\omega_{Bk}}$. Fig. shows the simulation of the CV model in closed-loop with the balancing controller, being initialized with the eigenvectors.
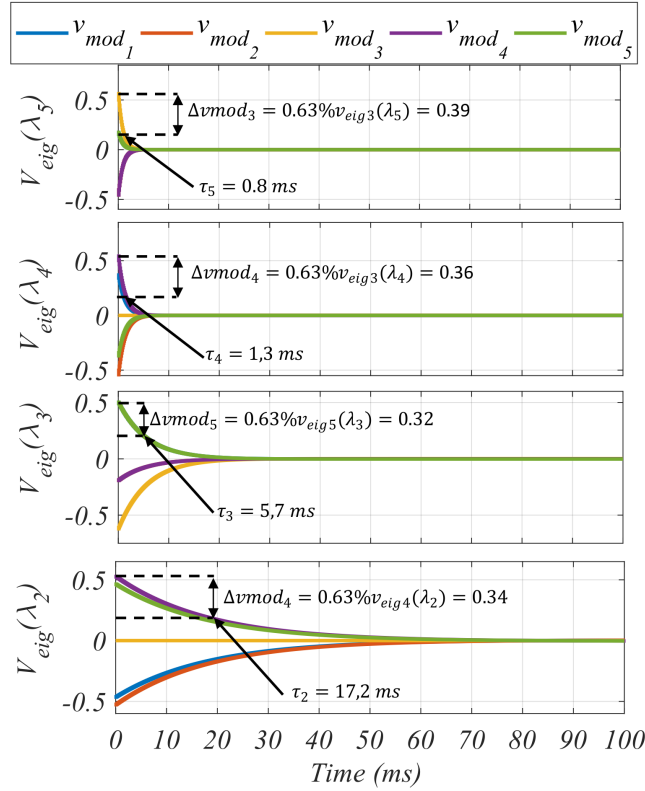
Figure 3.35: Modal response of the FCMC

Notice that, the cell-voltages decreases exponentially. This fact validates that only one mode acts according to the initial condition of the simulation. Table 3.5 shows the comparison between theory and simulation for each mode. Notice that the simulation and theoretical time-constants are very close. This fact demonstrates the relevance of the modal analysis to guarantee both the stability and the prediction of the dynamic responses of the converter. Concerning to the common-mode ($\lambda_1 = 0$), $\tau_1 = \infty$, it means that the v_k never decreases. This fact occurs when all the eigenvector has the same elements, meaning that the system is well balanced.

Table 3.5: Time constants of the first case

τ_k	**Theoretical (ms)**	Simulated (ms)
τ_2	0.81	0.8
τ_3	1.26	1.3
τ_4	5.6	5.7
τ_5	17.86	17.2

3.5.2.2 Modal analysis of the second case

For the second case, the modal response corresponds to a flying-capacitor multilevel converter in which the values of the capacitances are defined as: $C_k = 2C_o$ for $k = \{1, 2, 3\}$ and $C_k = C_o$, for $k = \{4, 5\}$. Therefore, $\mathbf{A_T D_{iff}}$ is:

$$\mathbf{A_T D_{iff}} = \begin{bmatrix} -1.5 & 1.5 & -0.5 & 0.0 & 0.5 \\ 2.0 & -3.0 & 2.0 & -0.5 & -0.5 \\ -0.5 & 2.0 & -3.0 & 2.0 & -0.5 \\ -1.0 & -0.5 & 2.5 & -4.5 & 3.5 \\ 1.0 & 0.0 & -1.0 & 3.0 & -3.0 \end{bmatrix} \tag{3.83}$$

Hence:

$$\mathbf{\Lambda} = \begin{bmatrix} 0 & 0 & 0 & 0 & 0 \\ 0 & -0.31 & 0 & 0 & 0 \\ 0 & 0 & -1.16 & 0 & 0 \\ 0 & 0 & 0 & -5.26 & 0 \\ 0 & 0 & 0 & 0 & -8.27 \end{bmatrix} \tag{3.84a}$$

$$\mathbf{V_{eig}} = \begin{bmatrix} -1.00 & -1.11 & 1.13 & -0.85 & -0.80 \\ -1.00 & -1.16 & -0.59 & 1.59 & 0.42 \\ -1.00 & 0.09 & -1.45 & 0.90 & 0.91 \\ -1.00 & 1.24 & -0.18 & -0.59 & 1.66 \\ -1.00 & 0.94 & 1.10 & 0.75 & -1.10 \end{bmatrix} \tag{3.84b}$$

$$\underbrace{\qquad}_{\mathbf{V_{eig}}(\lambda_1)} \underbrace{\qquad}_{\mathbf{V_{eig}}(\lambda_2)} \underbrace{\qquad}_{\mathbf{V_{eig}}(\lambda_3)} \underbrace{\qquad}_{\mathbf{V_{eig}}(\lambda_4)} \underbrace{\qquad}_{\mathbf{V_{eig}}(\lambda_5)}$$

As in the first case, the first eigenvalue is 0, indicating that only differential unbalances have to be considered in the system, the common-mode value being fixed by the input voltage value. Furthermore, it can be observed that the highest eigenvalue of this case is lower than the highest eigenvalue of the first case. Additionally, the ratio between the highest eigenvalue and the lowest, in this case, is greater than the ratio of those eigenvalues in the first case.

This fact indicates that the time responses are lower than the second case. Based on the diagonal matrix and the parameters of the converter, the controller for this case is defined as:

$$k_p = 2.08 \times 10^{-4} V^{-1} \tag{3.85a}$$

$$k_i = 80 V^{-1} s^{-1} \tag{3.85b}$$

In order to observe the time response of the system with the proposed controller, Fig. 3.36 shows the simulation of the modal response for the second case.
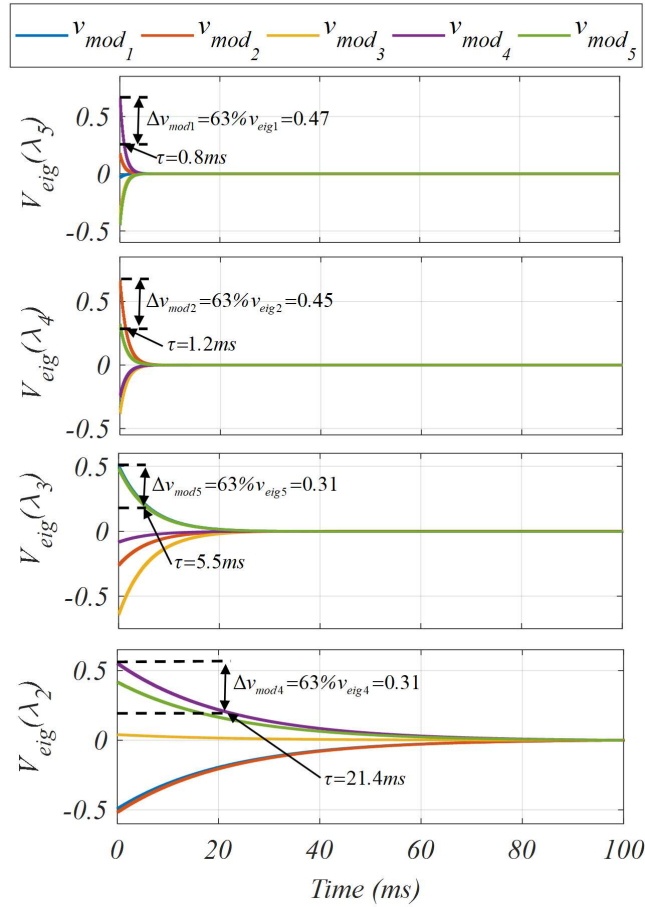
Figure 3.36: Modal response of the FCMC

Table 3.6 shows the comparison between theory and simulation for each mode for the second case. It can be seen the similarity between the simulation and the theoretical time constants. According to (3.81), $\lambda_1 = 0$. Hence, $\tau_1 = \infty$, meaning that the v_ks

Table 3.6: Time constants of the second case

τ_k	Theoretical (ms)	Simulated (ms)
τ_2	0.81	0.8
τ_3	1.27	1.2
τ_4	5.8	5.5
τ_5	21.6	21.4

never decreases. It happen when the initial condition is $\mathbf{V_e ig}(\lambda_1)$, in which all the v_ks have the same initial value. This mean that when the system start well balanced, the system maintain this operating point.

3.5.2.3 Simulation results

The first simulation correspond to the response of the system to a load transient, where the load is changed from 18.75 Ω to 12 Ω whith a reference current $i_{ref} = 12A$. Fig. 3.37 shows the behavior of i_o, v_s, v_{C_k} and v_k (respectively the output current, the output voltage, the capacitor voltages and the cell-voltages) when the disturbance occurs.
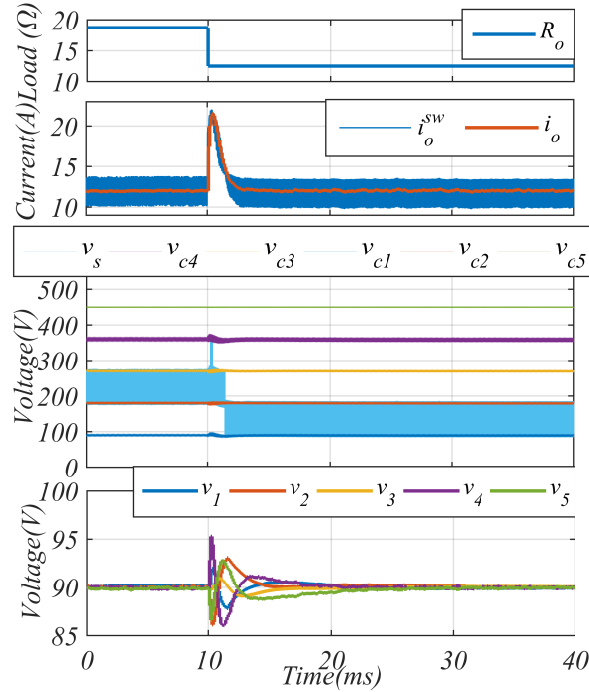
Figure 3.37: simulation results of load transient test

First, it should be noticed in Fig. 3.37 that when the load transient occurs the output current stabilizes in 3 ms, as expected. Moreover, the load step has been chosen so that the output voltage v_s switches between the two levels 270 V and 180 ($R_o = 18.75\Omega$) V, and 180 V and 90 V ($R_o = 12\Omega$), respectively before and after the transient. It can be noted that when the load transient occurs, the capacitor, v_{Ck}, and cell-voltages, v_k, are slightly disturbed. The disturbances on v_{Ck} are less than 2% and v_k has an overshoot of 5 % in the worst case, with a settling-time close to 30 ms. These observations confirm the previous theoretical results indicating the decoupling between the two loops (the cell-voltage balancing and is regulation).

The second simulation corresponds to the converter response to an input voltage step, v_e stepping from 450 V to 500 V. According to the theory, the cell-voltage values increase from 90 V to 100 V. Fig. 3.38 shows the waveform v_s, v_{Ck}, is and v_k. Notices that all the cell-voltages and the capacitor voltages increase 10% as expected and are stabilized in 30 ms as expected. Concerning the waveform of the current i_s, it presents an overshoot and it is stabilized after 5 ms approximately. The signal v_s also presents an overshoot and always switches between the two levels v_{C2} and v_{C3} as expected.
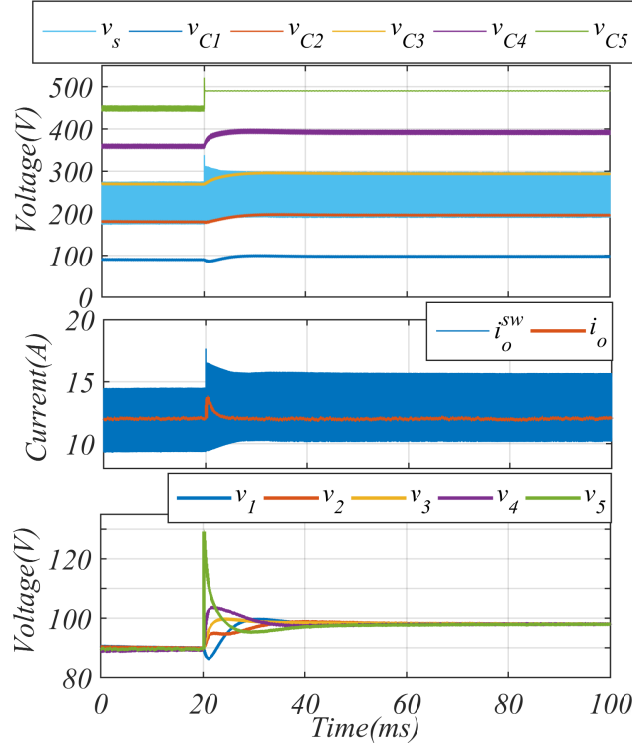
Figure 3.38: Simulation result of input voltage disturbance test

The last simulation corresponds to the insertion of a "sleeping" cell. In order to observe the behavior of the converter during a reconfiguration event, the test is carried out starting the FCMC up with only four active cells (the cells 1, 2, 4 and 5) and one sleeping cell (high-side and low-side transistors of cell 3 in ON-state). During operation, the cell 3 is activated. Fig. 3.39 shows the simulation results of this test. First, the value of the resistive load is chosen so that the output voltage v_s is close to 225 V when the current i_o is regulated to 12 A with an input voltage equals to 450 V. Then, using only four active cells, five voltage levels are available. Due to that, the interleaving of the carriers are designed for five cells, the converter output switches between the three levels 112 V, 225 V, and 337 V and a sub-harmonic current component at the switching frequency is observed when only four cells are activated. After the insertion of cell 3, six voltage levels are now available and well interleaved, then the output can switch only between the two levels 180 V and 270 V. Observing the waveform of the cell-voltages, it should be noted that before the insertion of the cell 3, v_3 is equal to 0 V and the other v_k are close to $v_e/4 = 112.5V$. After the cell insertion, v_3 starts to increase, balancing with the other cell-voltages at $450V/5 = 90V$. The output current i_s is almost not disturbed, validating the decoupling between the cell-voltage balancing and the current regulation loops. It can be observed that v_s switches between the levels v_{C1}, v_{C2} and v_{C3} before the insertion and between v_{C2} and v_{C3} after the cell insertion.
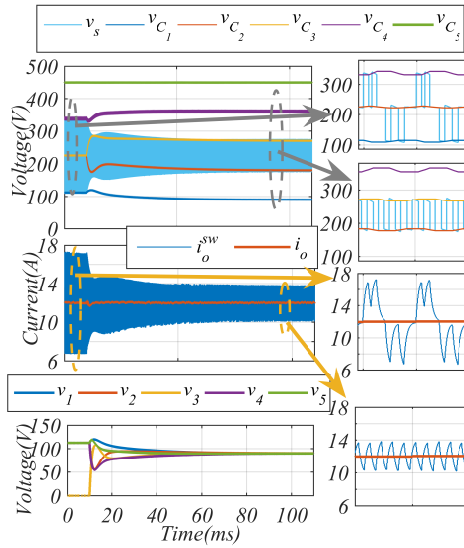
Figure 3.39: Simulation result of the cell insertion test

3.5.2.4 Experimental Results

The experimental results correspond to the same previous analysis and are performed with the same parameters. These experimental tests are developed with a prototype developed in LAPLACE-Lab, explained in [4, 5]. Fig. 3.40 shows the prototype of the flying capacitor converter where the decentralized controller is implemented.
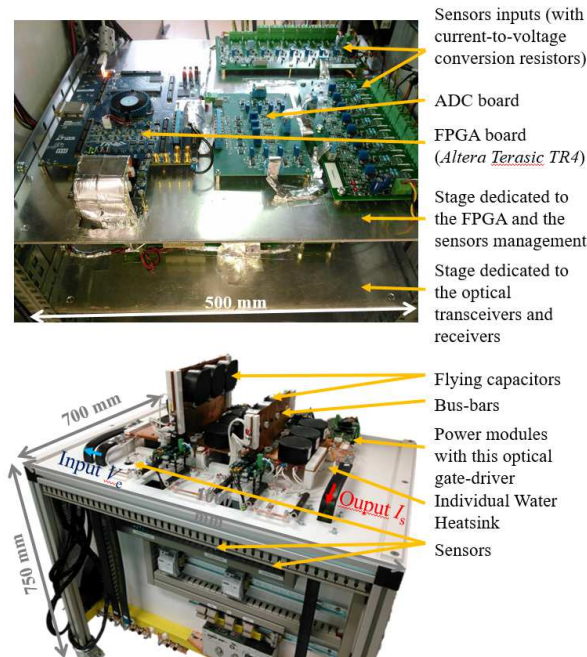
Figure 3.40: Prototype of the Flying-Capacitor Multilevel Converter

Fig. 3.41 shows the results of the load transient response analysis. The current stabilizes in 4 ms approximately, validating the simulation results. This test also shows that the output voltage v_s presents the same waveform as those obtained in simulation, switching between the levels v_{C3} and v_{C2} before the load step and switching between the v_{C2} and v_{C1} after. Furthermore, v_{Ck} and v_k signals stabilizes in 40 ms. Moreover, the disturbances observed on v_k and v_{Ck} signals are very low, validating the expected decoupling between the cell-voltage balancing and the output current is equation loops, as shown previously by the simulation.
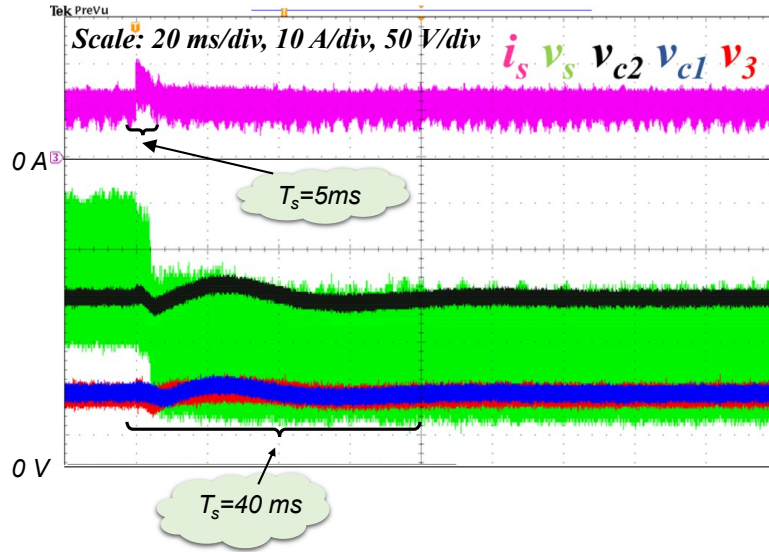
Figure 3.41: Experimental result of the load transient test

The second experimental test corresponds to the change in v_e from 450 V to 500 V. Fig. 3.42 shows the experimental results obtained on the prototype by applying a short transient on the input voltage of the converter (from 450V to 500V in 10 ms). According to the theory $v_{C1} = v_1$, the cell-voltage of cell 1. For that reason, v_3 which is the math channel computing $V_{C3} - V_{C2}$, is compared with v_{C1}. If the cell-voltages are well balanced, these two signals have to be equal. It is observed that when the disturbance occurs, v_{C1} and v_3 stabilize around 100V. Furthermore, the three others the capacitor voltages v_{C2}, v_{C3}, and v_{C4} increase toward the expected voltage levels, showing a strong similarity with the simulation results, stabilizing at the levels 200 V, 300 V, and 400 V, respectively.
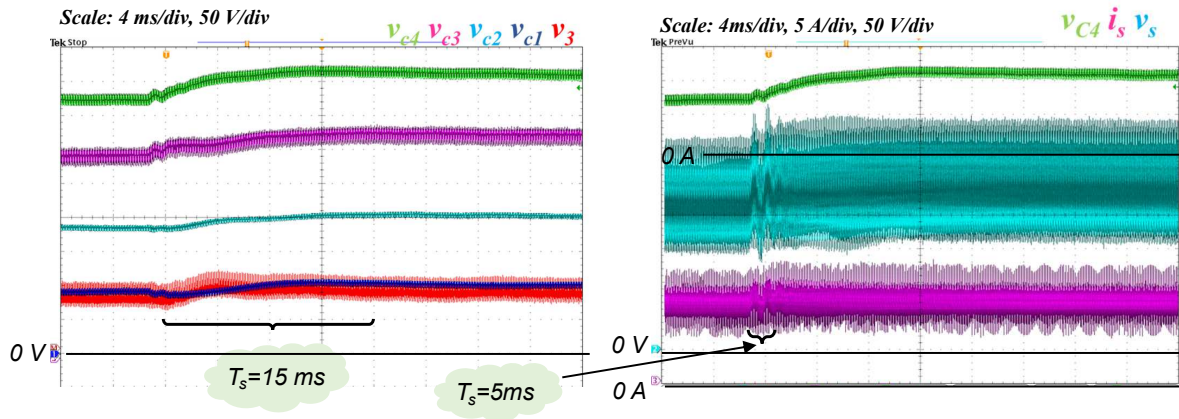
Figure 3.42: Results of the input voltage disturbance test

Fig. 3.43 shows the last experimental test, corresponding to the cell insertion during operation. Notices that the behavior of the cell and capacitor voltages are in concordance with the simulation test. It can be observed that when the cell is inserted, the system is stabilized after 40 ms. Furthermore, when the cell is inserted the ripple of the current changes, while the average does not change.
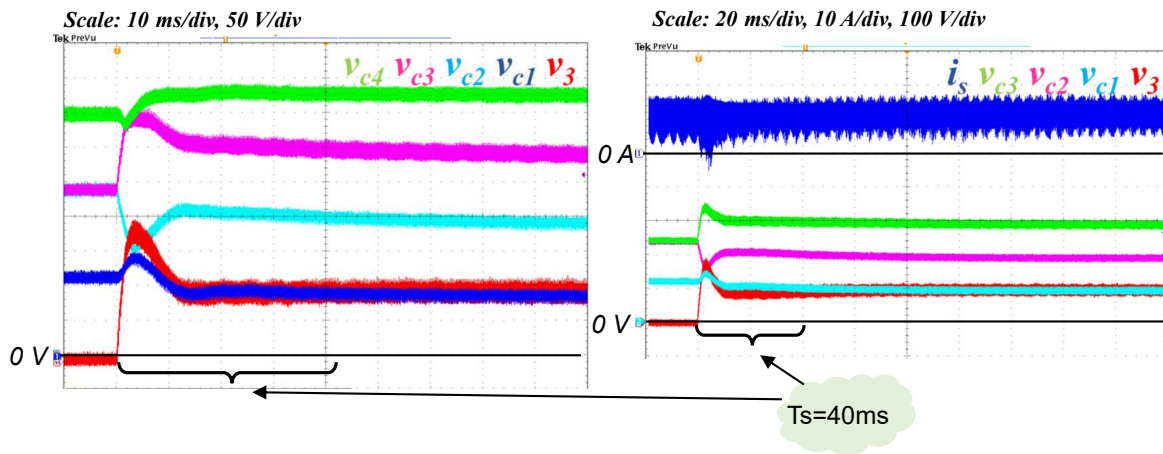
Figure 3.43: Results of the cell insertion test

3.6 Control method applied in the Cascaded Full-Bridge Multilevel Converter

For the case of cascaded Full-Bridge multilevel converter, the GV is the output current, $I_o(s)$ and the CV is the output voltage of the FB, $V_{Hk}(s)$. Hence, the control method for this converter is:

$$d_k(s) = K_{V_H}(s)\left(-V_{H_{k-1}} + 2V_{H_k} - V_{H_{k+1}}\right) + K_{i_o}(s)\left(I_{ref}(s) - I_o(s)\right) \qquad (3.86)$$

where, $K_{V_H}(s)$ and $K_{i_o}(s)$ are $K_X(s)$ and $K_Y(s)$ for this topology respectively. Expressing the controller as a matrix form:

$$\mathbf{D}(s) = K_{V_H}(s)\mathbf{D_{iff}}\mathbf{V'_H} + K_{i_o}(s)\left(I_{ref}(s) - I'_o(s)\right)\mathbf{V_1} \qquad (3.87)$$

According to (3.66), (3.64), table 3.2 and table 3.3, the model for $\mathbf{V_H}(s)$ and $I_o(s)$ with the control method is:

$$\mathbf{V_H}(s) = \underbrace{v_e K_{V_H}(s)\mathbf{D_{iff}}}_{\mathbf{F_{olv_H}}(s)} \mathbf{V'_H}(s) + \underbrace{v_e K_{i_o}(s)\left(I_{ref}(s) - I'_o(s)\right)\mathbf{V_1}}_{Trajectory\ of\ \mathbf{V_H}} + \mathbf{\Delta_{V_H}}(s) \qquad (3.88a)$$

$$I_o(s) = K_{i_o}(s)\underbrace{\overbrace{\frac{Nv_e}{L_o s + R_o + R_s}}^{G(s)}}_{F_{ol_{io}}(s)}\left(I_{ref}(s) - I'_o(s)\right) + \mathbf{V_1}^T\mathbf{\Delta_{V_H}}(s) \qquad (3.88b)$$

Notice that the duty-cycle obtained in each cell is the contribution of the GV regulator computation and the local CV balancing controller, as mentioned in the introduction to the decentralized control principle. It can be realized also that for this case, the decentralized controller decouples the GV from the CVs, as it is described in the theory of section 3.3. Notice also that the GV affects the trajectory of the CVs

The design of the GV regulator is very similar of the GV regulator designed for the FCMC, based on the bode analysis of the open-loop transfer function of the GV ($F_{ol_{io}}$), which depends on $G(s)$ and the GV regulator $K_{i_o}(s)$. In this case, the proposed controller for the GV, is an I controller, $K_{io}(s) = \dfrac{k_i}{s}$, because is the most straightforward controller that satisfies the stability of the system. The gain of the controller is based on the bode diagram presented in Fig. 3.44
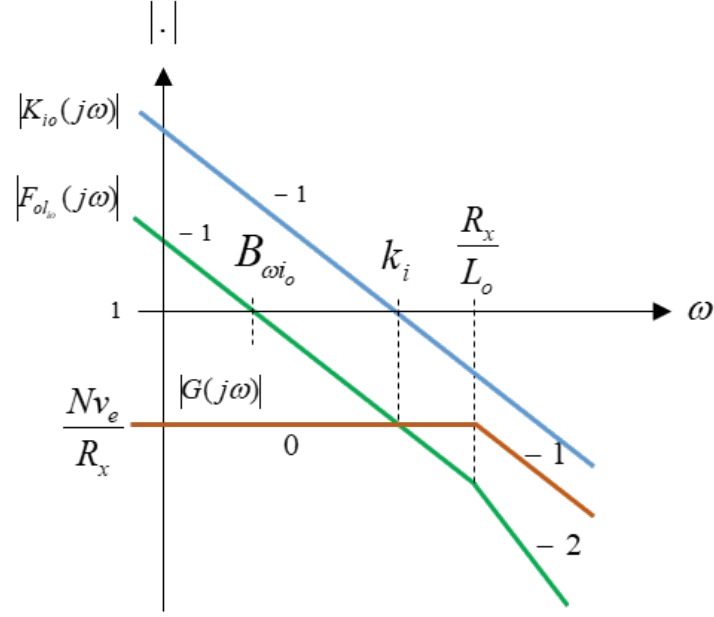
Figure 3.44: Bode diagram of $G(s)$, $K_{VH}(s)$ and $F_{olio}(s)$ of the CFBC

where $R_x = R_o + R_s$. Based on Fig. 3.44 it follows:

$$\frac{k_i N v_e}{R_x} = B_{\omega i_o}$$

$$k_i = \frac{B_{\omega i_o} R_x}{N v_e} \tag{3.89}$$

The criterion employed the bandwidth is that it has to be 10 times less than the switching frequency of the PWM of the MOSFETs.

3.6.1 Modal Analysis of the balancing Controller

As it is developed for the CFBMC, the design of the balancing controller for this converter is also based on its modal response. Hence, decomposing $\mathbf{F_{olV_H}}(s)$ on its modal and diagonal matrix, it follows:

$$\mathbf{F_{olV_H}}(s) = v_e K_{V_H}(s) \underbrace{\mathbf{D_{iff}}}_{\mathbf{V_{eig}} \mathbf{\Lambda} \mathbf{V_{eig}^{-1}}} \tag{3.90}$$

where $\mathbf{\Lambda}$ is the diagonal matrix of $\mathbf{D_{iff}}$ and has the same form of the diagonal matrix defined in (3.72). Therefore,

$$\mathbf{F_{olV_H}}(s) = \mathbf{V_{eig}} \underbrace{K_{VH}(s) v_e \mathbf{\Lambda}}_{\mathbf{\Pi}(s)} \mathbf{V_{eig}^{-1}} \tag{3.91}$$

For this topology the open-loop transfer function of the modal response $\mathbf{\Pi}(s)$ presents the elements of the diagonal ,$p_k(s)$, defined as:

$$p_k(s) = v_e \lambda_k \tag{3.92}$$

Hence, the open-loop transfer function related to the kth mode is:

$$F_{olm_k}(s) = v_e \lambda_k K_{VH}(s) \tag{3.93}$$

It has to mention that $\mathbf{D_{iff}}$ corresponds a circulant matrix $\mathbf{M_C}$, which is described as:

$$\mathbf{M_C} = \begin{bmatrix} c_0 & c_1 & \cdots & c_{N-1} \\ c_{N-1} & c_0 & \ddots & \vdots \\ \vdots & \ddots & \ddots & c_1 \\ c_1 & \cdots & c_{N-1} & c_0 \end{bmatrix} \tag{3.94}$$

Because of $\mathbf{D_{iff}}$ is a circulant matrix, it is possible to obtain a expression of its eigenvalues. According to [57] the eigenvalues of a circulant matrix is:

$$\lambda_k = \sum_{k=1}^{N-1} c_k e^{\frac{2\pi k (k-1)}{N} \hat{i}} \tag{3.95}$$

where $\hat{i} = \sqrt{-1}$. IT can be observed that for the case $\mathbf{D_{iff}}$, the coefficients, c_ks, are:

$$c_k = \begin{cases} 2 & ; k = 0 \\ -1 & ; k = \{1, \quad N-1\} \\ 0 & ; k = \{2 \quad 3 \quad \cdots \quad N-2\} \end{cases} \tag{3.96}$$

Therefore, according to (3.95), the eigenvalues of $\mathbf{D_{iff}}$ are defined as:

$$\lambda_k = c_0 + c_1 e^{\frac{2\pi (k-1)}{N} \hat{i}} + c_{N-1} e^{\frac{2\pi (k-1)(N-1)}{N} \hat{i}}$$

$$\lambda_k = 2 - e^{\frac{2\pi (k-1)}{N} \hat{i}} - e^{2\pi(k-1)\hat{i}} e^{-1\frac{2\pi (k-1)}{N} \hat{i}}$$

$$\lambda_k = 2 - \cos\left(\frac{2\pi (k-1)}{N}\right) - \hat{i} \sin\left(\frac{2\pi (k-1)}{N}\right) - \cos\left(-\frac{2\pi (k-1)}{N}\right) \tag{3.97}$$

$$- \hat{i} \sin\left(-\frac{2\pi (k-1)}{N}\right)$$

$$\lambda_k = 2\left(1 - \cos\left(\frac{2\pi (k-1)}{N}\right)\right)$$

Notice that the first eigenvalue, λ_1, is equal to 0, validating that it also represents the Laplacian of a graph. Furthermore, notice that because of the symmetric proprieties

of the cosine, the kth eigenvalue is equal to the $(N + 2 - k)^{th}$ eigenvalue. Finally, the highest eigenvalue is obtained for $k = \dfrac{N}{2} + 1$, when N is even and $k = \dfrac{N \pm 1}{2} + 1$ when N is odd. The maximum case is produced when N is even, generating a $\lambda_{max} = 4$. The design of the balancing controller is based on the possible maximum eigenvalue, λ_{max} and the minimum eigenvalue, $\lambda_{min} = \lambda_1$, which are $\lambda_{max} = 4$ and $\lambda_{min} = 0$.

$\lambda_{min} = 0$ means that the system presents a pure integrator, that theoretically is stable. However, because of numeric approximations in the implementation, it is possible that the system tent to be unstable after a large lapse. For that reason, the controller selected corresponds to a low pass filter that ensures that the system is not unstable with a pole located at very low frequency. Hence, the proposed controller is:

$$K_{VH}(s) = k_p \left(\frac{k_i}{s + k_i} \right) \tag{3.98}$$

In order to design the parameters of the controller, Fig. 3.45 shows the bode diagram of $K_{VH}(s)$, $p_k(s)$, $f_{olmk}(s)$.
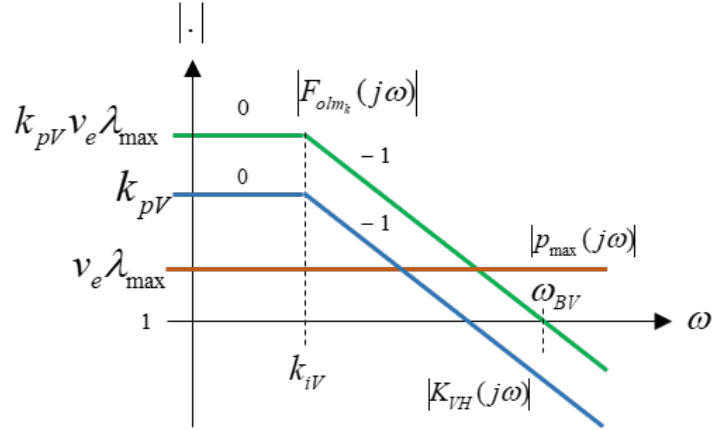
Figure 3.45: Bode diagram of p_{max}, $K_{VH}(s)$ and $F_{olmk}(s)$ of the CFBC

Based on the bode diagram of Fig. 3.45, the bandwidth ω_{BV} is:

$$v_e \lambda_{max} k_{pV} = \frac{\omega_{BV}}{k_{iV}}$$
$$k_{pV} = \frac{\omega_{BV}}{v_e \lambda_{max} k_{iV}} \tag{3.99}$$

The criterion of the selection of the bandwidth, ω_{BV} is to be ten times less than the switching frequency f_{sw}. Because the converter can work as an inverter and as a DC/DC converter, the pole p is selected 10 times less than the operating frequency of the inverter. The next subsection presents the results obtained with the implementation of the proposed controller in this topology.

3.6.2 Results

The results are obtained with a prototype that is developed at Javeriana University, with the following parameters:

Table 3.7: Parameters of the CFBMC

Parameter	Value	Parameter	Value
Number of FBs (N)	5	Load Resistance (R_o)	$60\ \Omega - 100\ \Omega$
Input Voltage (v_e)	$48\ V$	Switching frequency (f_{sw})	12.5 kHz
Input Inductance (L)	$1.8\ mH$	I_{ref} as a DC/DC converter	$1.7\ A$
ESR of L (R)	$200\ m\Omega$	I_{ref} as an inverter	$1.7\sin\left(2\pi ft\right)\ A$
Input Capacitance (C)	$4\ mF$	Frequency of the inverter (f)	60 Hz
DS ON Resistance (R_{DS})	$58\ m\Omega$		

The gains and the pole of the controllers are:

Table 3.8: Parameters of the Controllers

Parameter	Value
k_i	$1884\ A^{-1}s^{-1}$
k_{pV}	$-39\ V^{-1}s^{-1}$
k_{iV}	$37.7\ rads/s$

These results correspond to the modal response of the closed-loop system. Both simulation and experimental results are provided and discussed.

3.6.2.1 Modal response

As it is developed for the FCMC, for this case the modal response is obtained using similar Modal matrix $\mathbf{V_{eig}}$ and the diagonal matrix $\mathbf{\Lambda}$. It has to take to into account that in this case the matrix to be diagonalized is a circulant one, as it explained previously. Hence, $\mathbf{\Lambda}$ is described as:

$$\mathbf{\Lambda} = \frac{\sqrt{5}}{2}\begin{bmatrix} 0 & 0 & 0 & 0 & 0 \\ 0 & \sqrt{5}-1 & 0 & 0 & 0 \\ 0 & 0 & \sqrt{5}+1 & 0 & 0 \\ 0 & 0 & 0 & \sqrt{5}+1 & 0 \\ 0 & 0 & 0 & 0 & \sqrt{5}-1 \end{bmatrix} \tag{3.100}$$

Notice that $\lambda_2 = \lambda_5$ and $\lambda_3 = \lambda_4$, as (3.97) indicates. Hence, expressing as numerical form

$$\mathbf{\Lambda} = \begin{bmatrix} 0 & 0 & 0 & 0 & 0 \\ 0 & 1.382 & 0 & 0 & 0 \\ 0 & 0 & 3.618 & 0 & 0 \\ 0 & 0 & 0 & 3.618 & 0 \\ 0 & 0 & 0 & 0 & 1.382 \end{bmatrix} \tag{3.101}$$

And the modal matrix is:

$$\mathbf{V_{eig}} = \underbrace{\begin{bmatrix} 1.00 & 1.00 & 1.00 & 1.00 & 1.00 \\ 1.00 & -0.57 & -0.52 & -2.00 & 1.33 \\ 1.00 & -1.35 & -0.16 & 2.23 & -0.18 \\ 1.00 & -0.26 & 0.78 & -1.61 & -1.44 \\ 1.00 & 1.19 & -1.1 & 0.38 & -0.72 \end{bmatrix}}_{\mathbf{V_{eig}}(\lambda_1) \; \mathbf{V_{eig}}(\lambda_2) \; \mathbf{V_{eig}}(\lambda_3) \; \mathbf{V_{eig}}(\lambda_4) \; \mathbf{V_{eig}}(\lambda_5)} \tag{3.102}$$

Using the eigenvectors as the initial condition, Fig. 3.46 shows the modal respond of the system
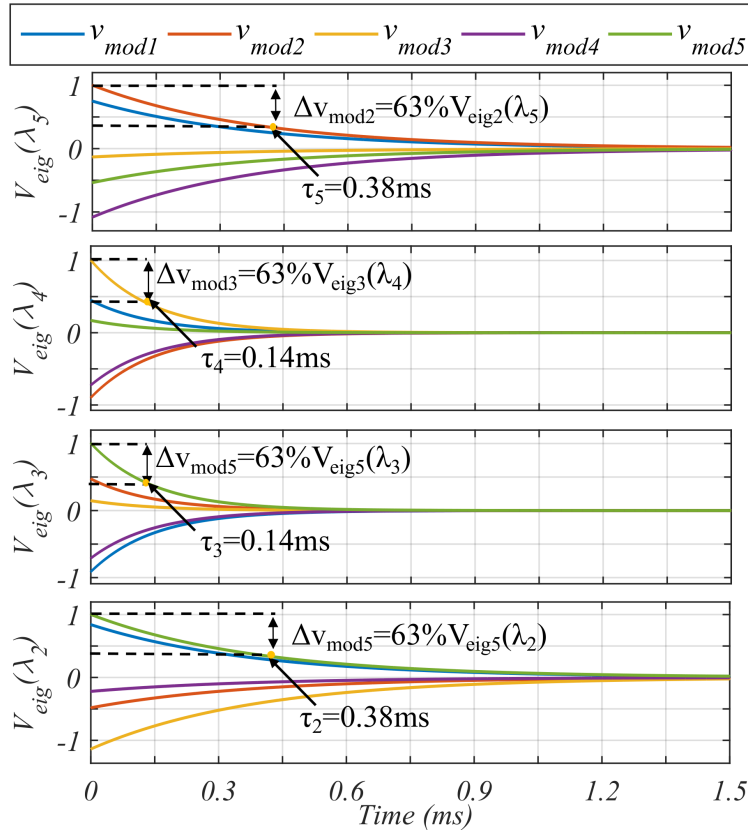
Figure 3.46: Modal response of the of the CFBMC with the decentralized controller

Based on Fig. 3.46, table 3.9 shows a comparison between the theoretical time constants and the time constants obtained by simulation.

Table 3.9: Time constants of the CFBMC

τ_k	**Theoretical (ms)**	Simulated (ms)
τ_2	0.384	0.38
τ_3	0.146	0.14
τ_4	0.146	0.14
τ_5	0.384	0.38

Notice that because there are two pairs of similar eigenvalues, there are also two pairs of two time constant, meaning that there are two double pole at these time constants. Notice that simulated and theoretical values are very similar, validating the performance of the controller.

3.6.2.2 Simulation Results

The following simulations correspond to three tests, implemented both for DC/DC mode and DC/AC mode. The first test corresponds to a load transient from 95 Ω to 70 Ω. Fig. 3.47 shows v_s and i_o when the converter works as a DC/DC.
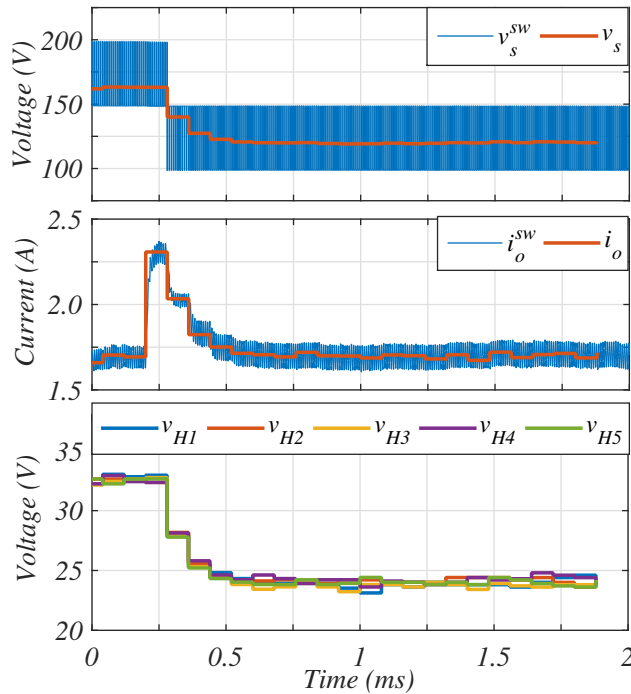
Figure 3.47: Simulation of the load transient transient response as a DC/DC

Notice that when the load is inserted, the current present an overshoot until 2.2 A, then, after 0.5 ms the current i_o and the voltages v_Hs are stabilized. This settling time is in concordance with the bandwidth imposed by the parameters of the current regulator. According to the theory, the disturbances in the current loop do not affect the balancing of the CV. Only the trajectories of the CVs are affected because the trajectory depends on the output current. This fact is validated in this simulation. Furthermore, it can be observed that when the load step occurs, v_s is adjusted from 160 V to 125 V, implying that v_s^{sw} passes from switching between 150 V and 200 V, from switching between 100 V and 150V.

The next simulation shown in Fig 3.48 corresponds to a load transient with the converter working as a DC/AC converter.
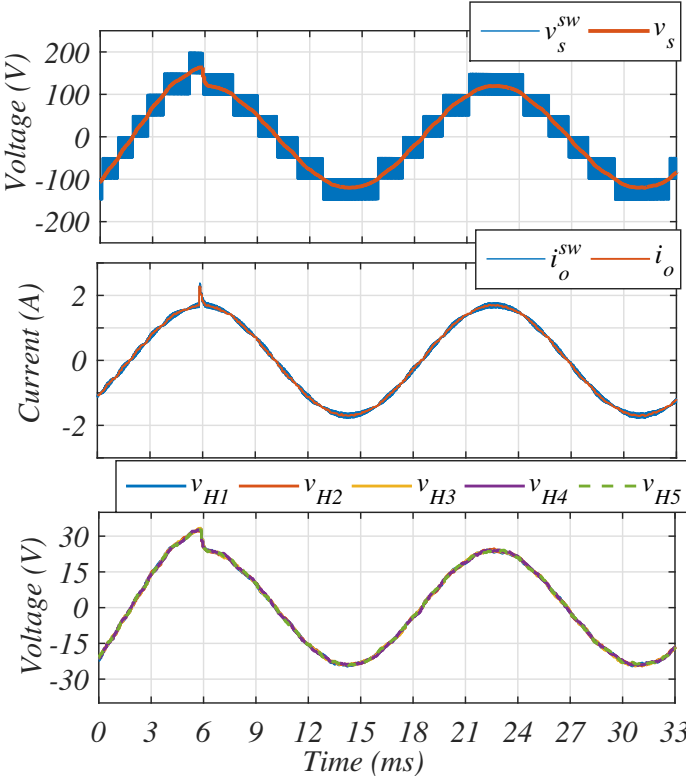
Figure 3.48: Load transient test as a DC/AC

Notice that the system presents a good response in a DC/AC mode. It can be observed that before the disturbance, the system reaches 9 levels and after the disturbance, just 7 levels are required to regulate the current, indicating that the supplied voltage has decreased for regulating the current. Notice also that the CVs are balanced during all the simulation, before and after the disturbance, validating for DC/AC mode that when a disturbance in the current occurs, the CVs are not unbalanced, only the trajectory in the CVs are affected. Furthermore, the current is stabilized in a small lapse, less than 1 ms.

The next simulation result, shown in Fig. 3.49, corresponds to an input voltage disturbance from 40 V to 50 V, working in DC/DC mode with a resistive load of 77 Ω.
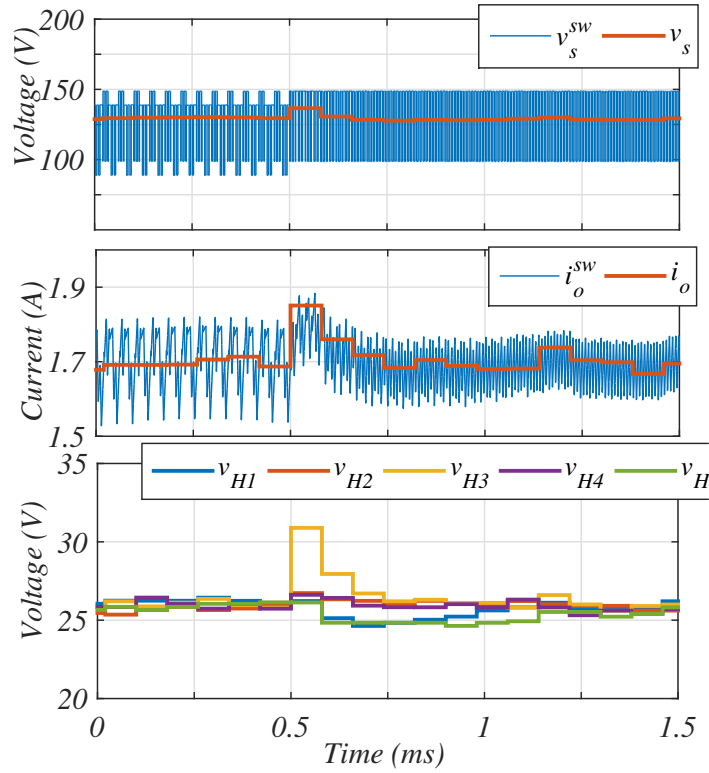
Figure 3.49: Input voltage step response simulation as a DC/DC

Note that before the voltage step, there is an asymmetric ripple in the current due to the different values in the input voltages. However, v_Hs are well balanced and the average output current is well regulated. When one of the input voltage change to 50 V, the v_{Hk}s are auto balanced, and the output current presents a small overshoot. This test validates the expected behavior of the balancing controller when a change in one source occurs.

The next simulation corresponds to a step voltage when the converter works as a DC/AC. Fig. 3.50 shows the results of this test. Notice that the voltage disturbance almost affects neither the output current i_o nor the output voltage v_s, while the CVs are auto balanced in 0.5 ms, as same as the output current. Fig. 3.50 also shows that when one of the input voltage is 40 V, there exists an asymmetric ripple in $i_o i^{sw}$ and $v_s i^{sw}$ and when the input voltage is 50 V, the ripples are equalized. However, the average output current i_o and the v_{Hk}s are well regulated and balanced, respectively.
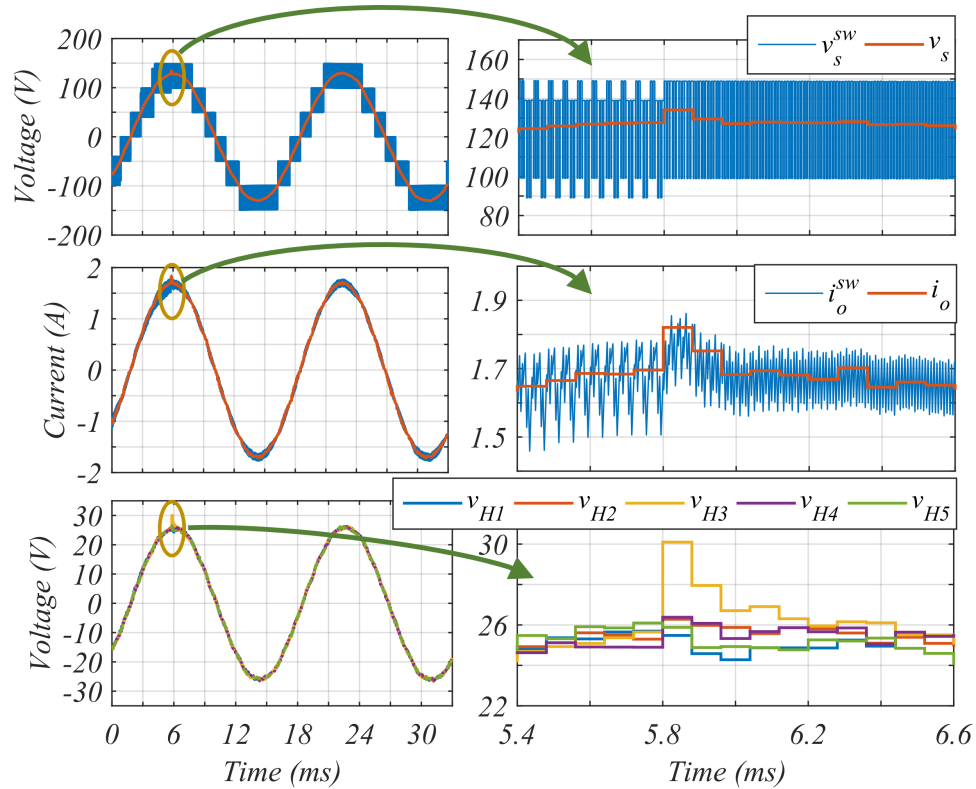
Figure 3.50: Input voltage step response simulation as a DC/AC

The next simulation corresponds to a cell insertion during operation, passing from 4 FBs to 5 FBs, when the converter works as a DC/DC. Fig. 3.51 shows the results of the v_{Hk}s, i_o and v_s. It can be noticed that before the cell insertion, i_o and v_s present a high ripple, because of there is no interleaving control in the carrier, and those are designed for 5 cells. Perhaps the ripple is high, the average of the current is regulated when there are 4 cells. When the fifth FB is inserted, i_o presents an overshoot and then it is stabilized in less than v_{Hk}s are balanced when there are 4 FBs and then, when the 5th cell is inserted, there are auto balanced, reaching a new operation point in 0.25 ms approximately. The last simulation is a cell insertion when the converter works as an inverter. Fig 3.52 shows the results. It can be observed in this test that the current presents also a high ripple before the cell insertion, because there is no interleaving control, as it is explained previously. However, the average current is regulated. After the cell insertion, the current ripple is reduced significantly and the average of the current is regulated. Furthermore, the FBs are balanced before the cell insertion and after that, there are auto balanced in a new operation point, as same as it happens in the DC/DC mode. This test validates by simulation the three functions of the controller, the balancing of the CV, the regulation of the GV, and the bypass system.
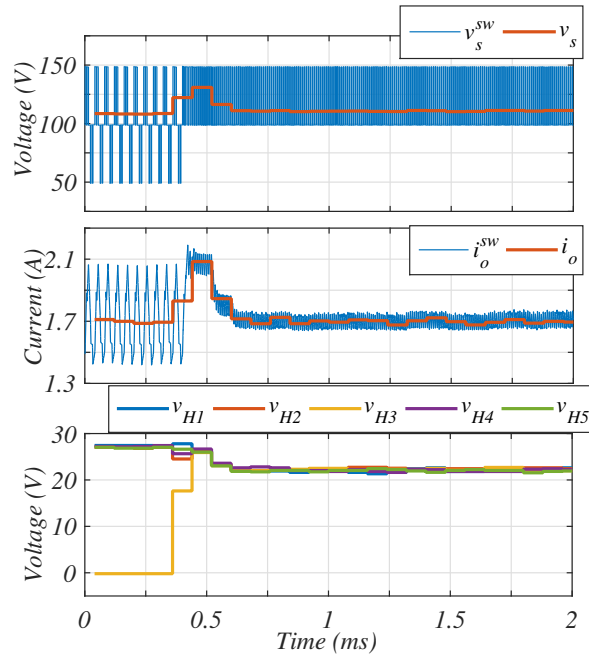
Figure 3.51:   FB insertion simulation with a DC/DC conversion
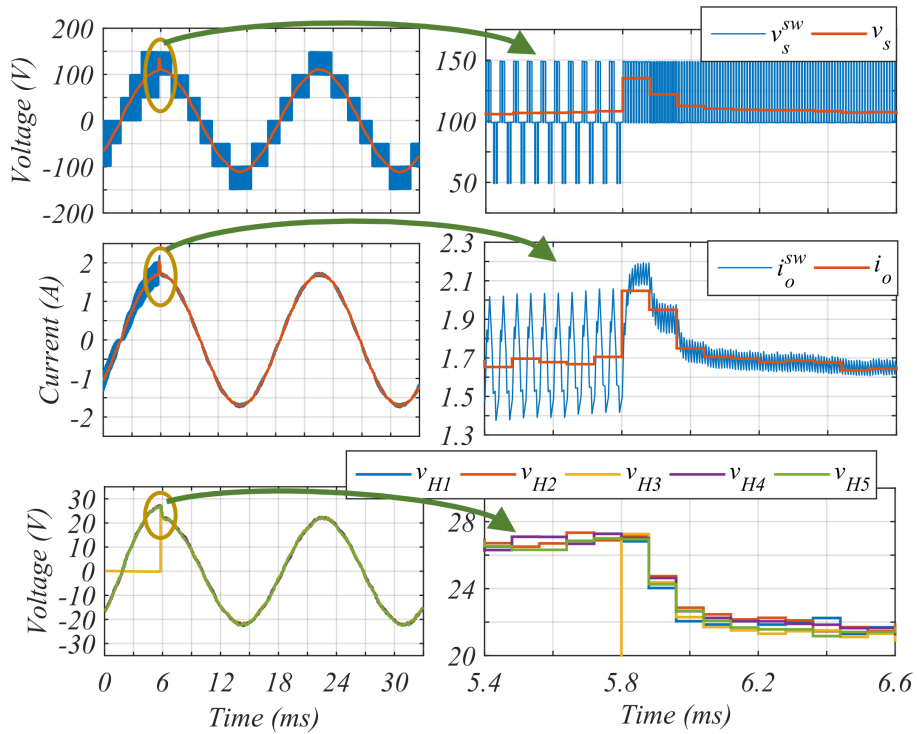
Figure 3.52:   FB insertion simulation with a DC/AC conversion

It can be inferred that all the simulation results are in concordance with the the theory developed in this chapter, producing a good performance of the controller for this topology, working either as a DC/DC or DC/AC mode.

The next stage of this subsection presents the experimental results.

3.6.2.3 Experimental Results

As it is mentioned previously, the experimental results are developed with a prototype that is implemented in Javeriana University, which is composed of a Cascaded Full Bridge Multilevel Converter of 5 FB, fed by Lithium Batteries of 48 V, with the parameters described in table 3.7. Fig. 3.53 presents the developed prototype.
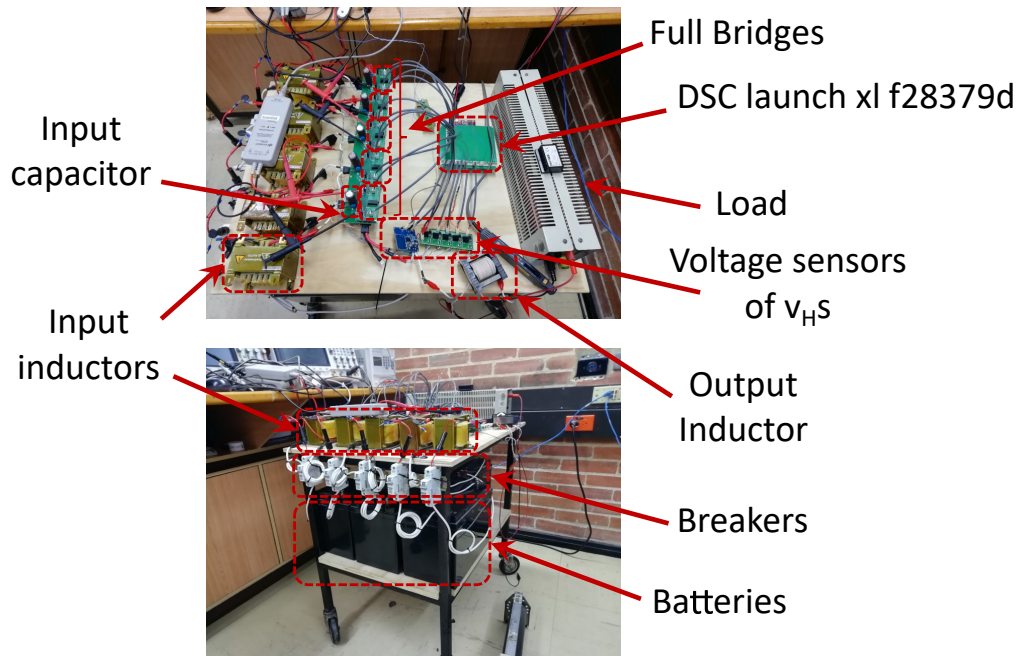
Figure 3.53: Setup of the Cascaded Full-Bridge Multilevel Inverter

In order to compare the simulation and experimental results, the tests developed here are the identical to the ones carried out in the previous simulations.

Fig. 3.54 shows the experimental results of first test corresponding to a load step (or load transient) in a DC/DC mode. It can be seen that there exists a concordance with the simulation result of this test, presenting similar overshoot in the current and similar settling time of 0.5 ms approximately. Moreover, there is a similarity in the switching levels of v_s . Furthermore, as happened in the simulation, the operation points of v_{Hk}s before and after the load transient and changing from 32 V to 22 V approximately in 0. 5 ms without unbalance them. Furthermore, it is possible to observe that after the load transient the duty-cycle of the v_H^{sw} is reduced to adjust the average of v_Hs.
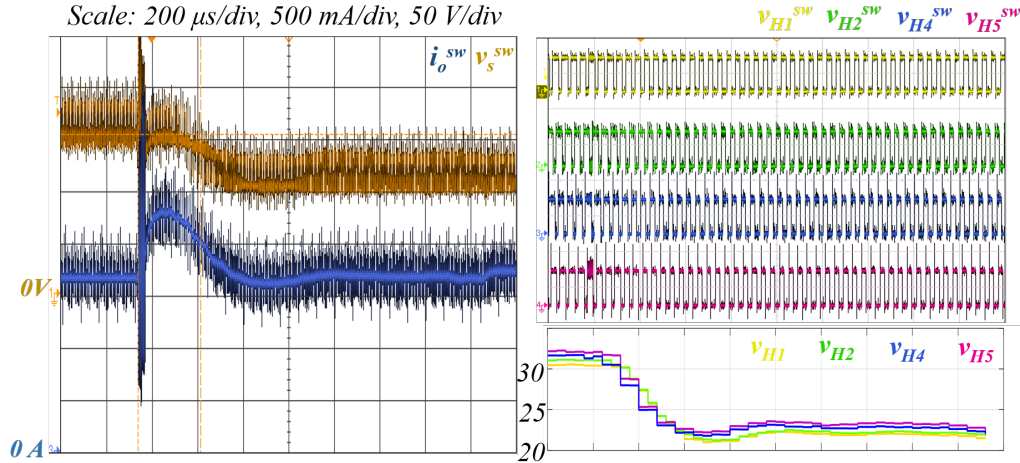
Figure 3.54: Load transient test in DC/DC mode

The next test presents the experimental results, changing the load when the converter works as an inverter.
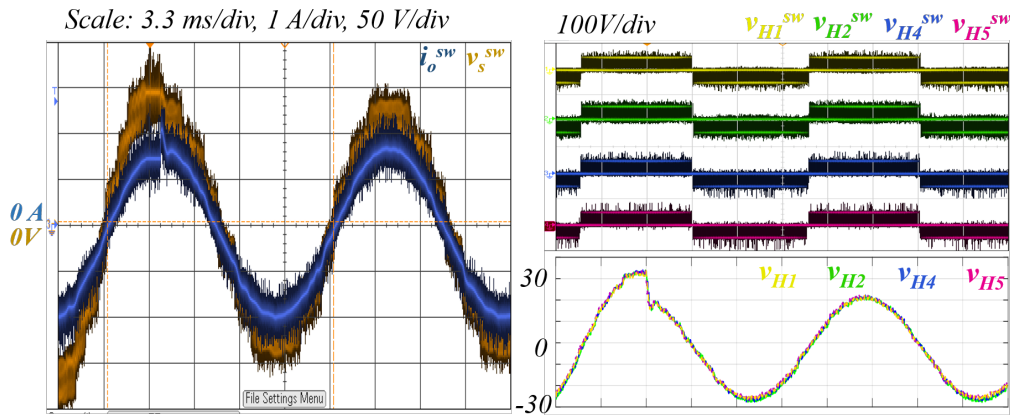
Figure 3.55: Load transient experimental test in DC/AC mode

Notice that as in the simulation test, the current and the v_Hs are stabilized in 0.5 ms and the v_{Hk}s are well balanced during all the tests. When the load transient in produced, v_{Hk}s change their trajectory without being unbalanced, validating the proposed theory. Furthermore, it can be observed that after the load transient there is a change in the switching levels of v_s as happen in the simulation test.

The next result corresponds to the disturbance in one input voltage when the system works as a DC/DC. Fig. 3.56 shows the behavior of the v_{Hk}s and Fig. shows shows the output current v_s and the output voltage v_s
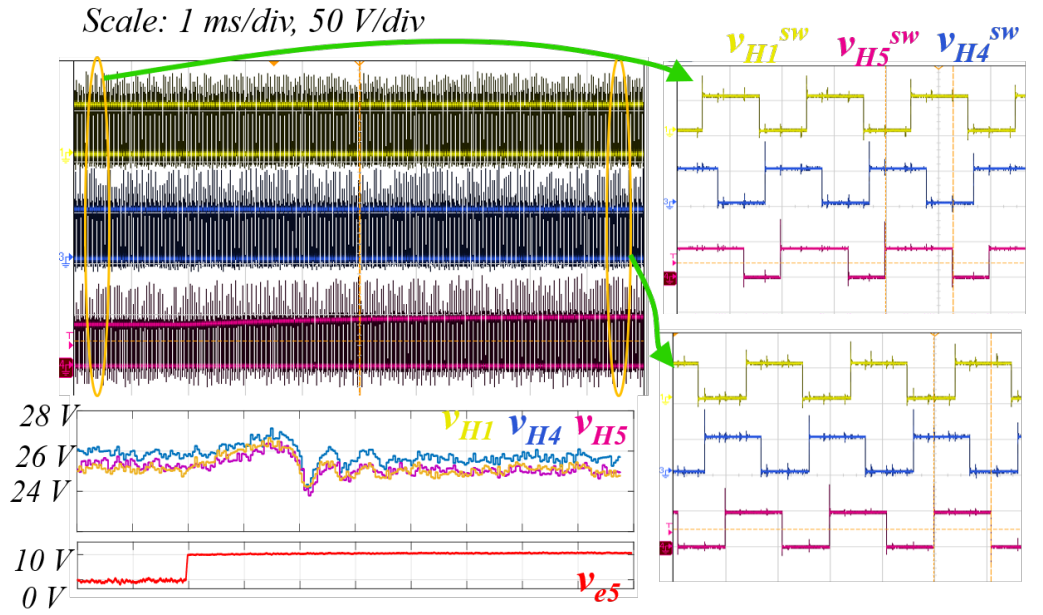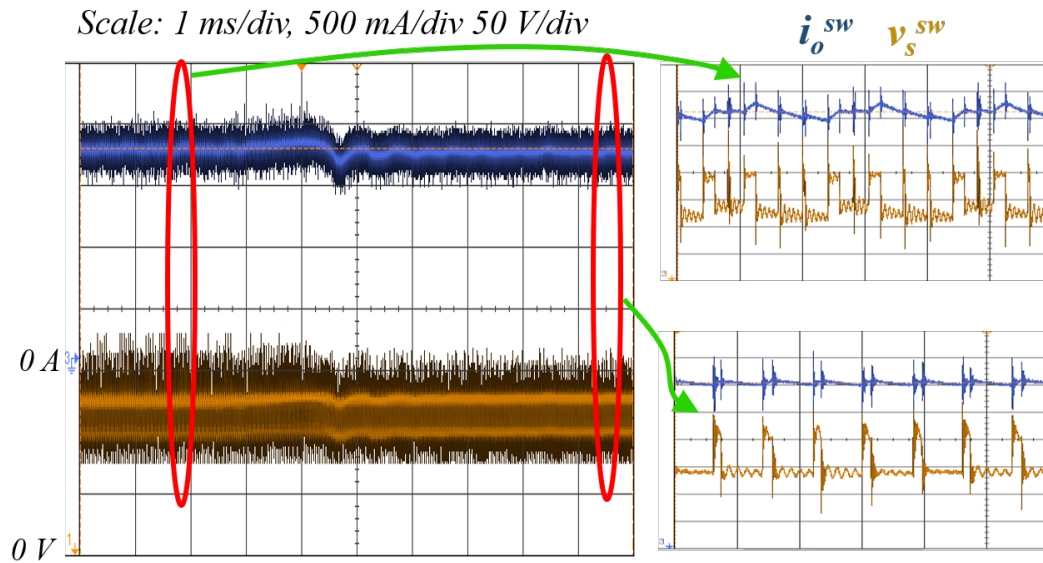
Figure 3.56: Voltage disturbance test in DC/DC mode (a) v_{Hk} and v_{Hk}^{sw}; (b) i_o^{sw} and v_s^{sw}

Notice that there are soft changes in v_Hs. This is because the input filters presented in the converter smooth the effect of the voltage disturbance. However, it can be observed the change of the duty-cycles before and after the voltage disturbance, validating the performance of the balancing controller. Furthermore, it can be observed

that during all the experiments, v_Hs are well balanced, having a small transient and going back to the same operating point. This fact also validates the balancing controller, maintaining the same output voltage of each FB even when the input voltages change. Additionally, Fig. 3.56 shows that the output current and the output voltage present an asymmetric ripple when $v_{H5} = 40$. Nevertheless, the output current is regulated. When the voltage change occurs the ripple is equalized and also reduced because all the v_{ek}s are identical.

The next experimental result corresponds to a voltage disturbance when the converter works as an inverter.
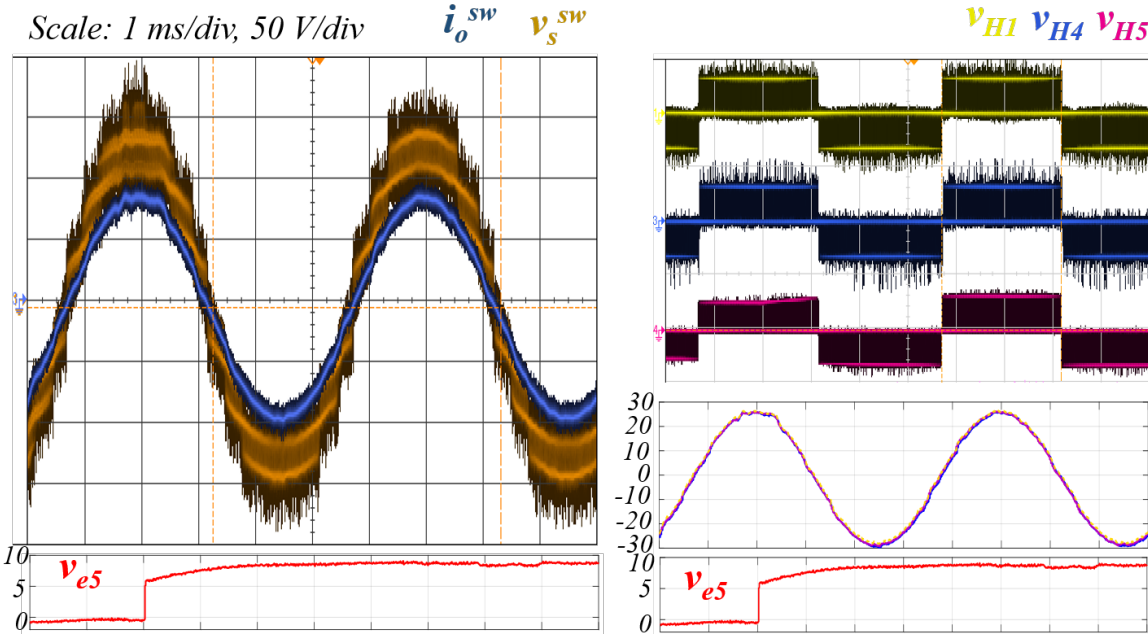
Figure 3.57: Voltage disturbance test in DC/AC mode

Notice that the step voltage is almost not detected due to the input filter, as happen in the DC/DC test. Furthermore, it can be observed that v_Hs are well balanced during the test and the output current is always regulated.

The next result corresponds to a FB insertion during operation, starting with 4 FB and inserting the 5th FB, when the system is working as a DC/DC converter. It can be observed in Fig. 3.58, that when there are 4 FBs there exists an asymmetric ripple in v_s and i_o because of the no suitable interleaving for 4 cells. However, both the output current and output voltage are regulated. After the insertion due to the interleaving is designed for 5 cells, the ripples of v_s and i_o are symmetric and it is reduced. Furthermore, it can be observed how are equalized the CVs after the insertion, reaching a new operation point with a settling time after 0.5 ms. These values are in concordance with the time constants of the system and also there exists a strong similarity with the simulation results.

Scale: 200 μs/div, 50 V/div v_{H1}^{sw} v_{H2}^{sw} v_{H4}^{sw} v_{H5}^{sw} *Scale: 20 μs/div*

Scale: 200 μs/div, 10 V/div v_{H1} v_{H2} v_{H4} v_{H5}

0 V

(a)

Scale: 200 μs/div, 50 V/div, 1A/div i_o^{sw} v_s^{sw} *Scale: 20 μs/div, 50V/div, 200mA/div*
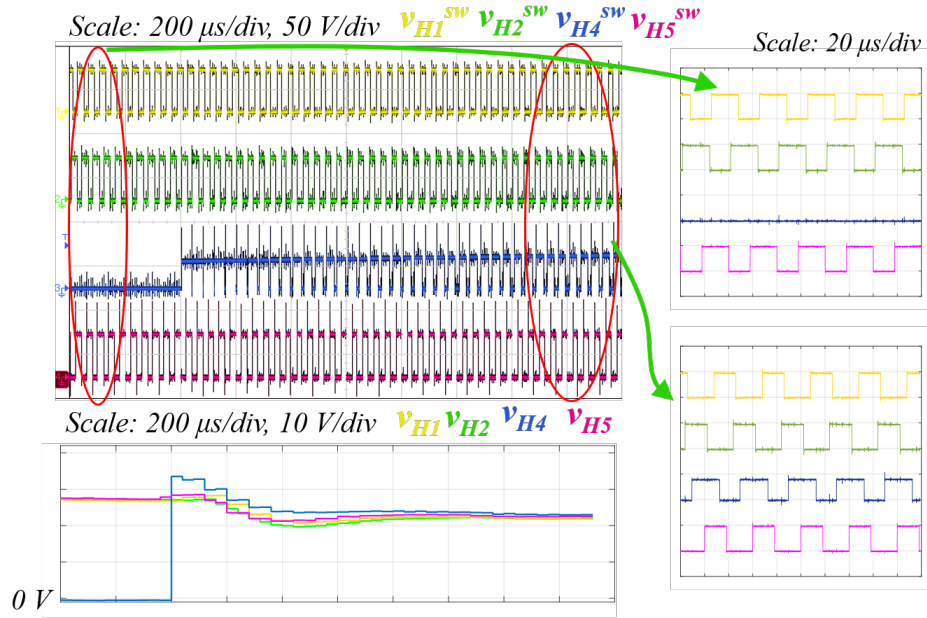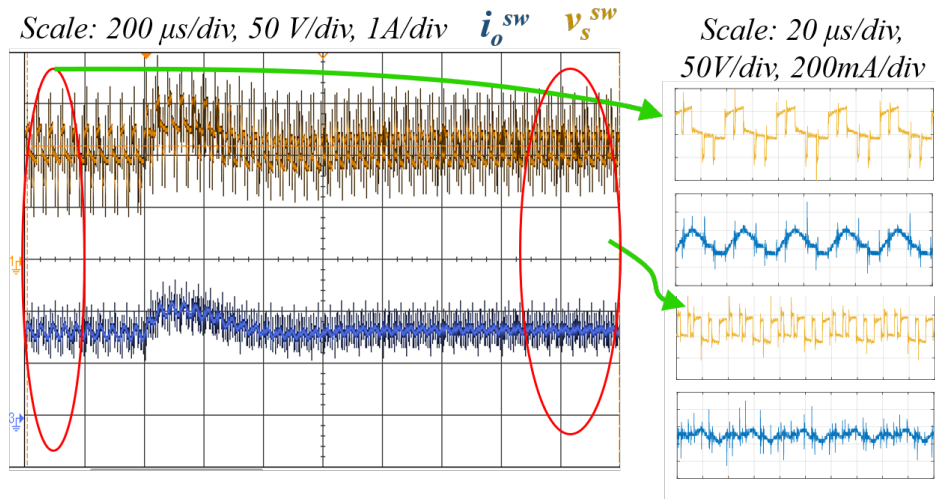
(b)

Figure 3.58: FB insertion test in DC/DC mode (a) v_{Hk} and v_{Hk}^{sw}; (b) i_o^{sw} and v_s^{sw}

The last test, shown in Fig. 3.59 presents the results of a FB insertion during operation when the converter works as a DC/AC converter. Notice that the current follows the reference during all the experiments, presenting a small transient when the FB is inserted. Furthermore, the v_Hs are balanced before and after the cell insertion, with also a small disturbance in the transient. These two last tests validate the three stages of the controller, the balancing controller, the GV regulator, and the bypass

system. It can be inferred that all the experimental tests are in concordance with the simulation test and the theory developed in this chapter, producing a good performance of the controller for this topology.
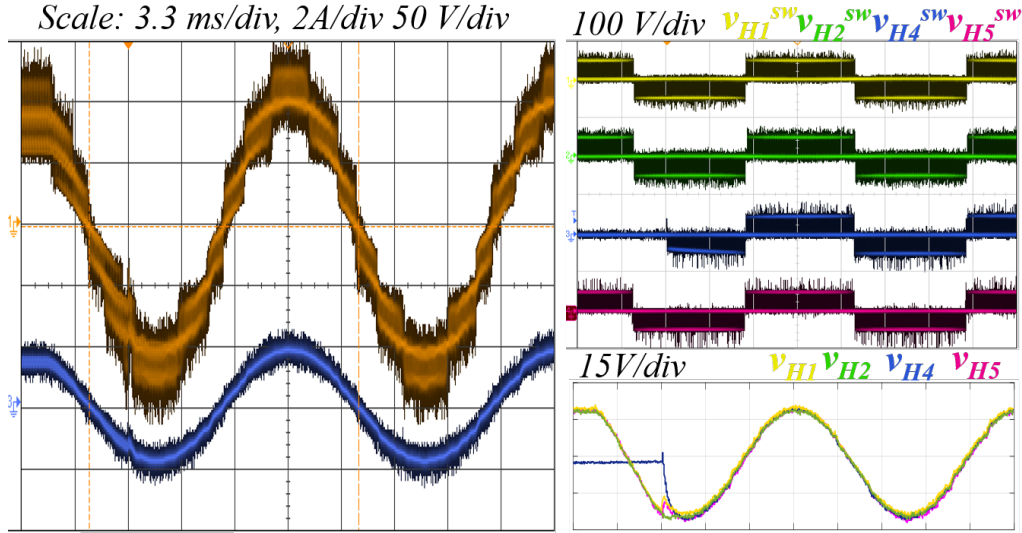
Figure 3.59: FB insertion test in DC/AC mode

3.7 Conclusions of this section

The proposed control methods allow balancing the cell variables, to regulate the output variable and gives to the MCC the ability of insertion and removal of a cell during operation if the MCC is modeled as the proposed model.

The control method is implemented in two different typologies of the multilevel converter, a cascaded full-bridge multilevel converter, and a flying-capacitor multilevel converter.

The performance of the control method is validated with simulation and experimental tests obtaining good results disturbing the input voltage, stepping the load and inserting a cell during operation, presenting concordance with the theory, the simulation and the experimentation. This control is available for any multilevel converter if it can be modeled as the proposed model. As future works, the implementation of this control method for balancing the state of charge of the batteries when those are the input voltage of a cascade full bridge multilevel converter is being developed. Another future work is the implementation of this control method in the multi-phase buck converter.

Chapter 4

Adaptive Selective Harmonic Elimination Strategies for the control of multilevel Inverters

The second core of the research deals with a control strategy for any symmetric Multilevel Inverter, modulated by the Selective Harmonic Elimination (SHE) strategy. This work is inspired by the complexity of having a feedback circuit to control the output voltage in low frequency modulation strategies. All the theory is developed, using a Cascaded Equal Full-Bridge Multilevel Inverter of 4 cells (FBs), generating 9 levels. However, it can be applied to any symmetric Multilevel Inverter of 9 levels, and also it can be extrapolated or scaled for more levels. The aim of SHE is to adjust the fundamental Fourier component to a reference, and to eliminate the N-1 most significant harmonics, switching N times per quarter of a cycle. This chapter starts explaining the obtention of the harmonics and the equations that rule SHE.

4.1 Description of the system

The system where the control is implemented corresponds to a Cascaded Equal Multilevel Inverter (CEMI) shown in Fig. 2.1(a), composed of 4 FB (N=4) and connected to a resistive load. Although the inputs are the same, it may exist some disturbances or variation in the input. Low frequency modulation strategy is based on switching a finite number times per period, adjusting the fundamental component and eliminating some significant harmonics [14, 15, 37, 41, 43, 44], or minimizing the Total Harmonic Distortion (THD) [12, 13]. In this work, each FB switches once per quarter of a cycle, and the aims are to control the fundamental component and to eliminate as many harmonics as possible. Fig.2.18 shows the waveform of the output voltage, dismissing the effects of inductors and capacitors of the input filters. Notice that the waveform is symmetric in both axes, where FB_k switches at θ_k, $\pi - \theta_k$, $\pi + \theta_k$, $2\pi - \theta_k$.

4.1.1 Modeling the system

According to Appendix A, the Fourier components of the kth FB, when its respectively sources have different values, are:

$$a_{km} = 0$$

$$b_{km} = \begin{cases} \dfrac{4v_{ek}}{m\pi} \cos\left(m\theta_k\right) & ; \quad m \ is \ odd \\ 0 & ; \quad m \ is \ even \end{cases} \tag{4.1}$$

Hence, knowing that v_s is the sum all the output voltages of the FBs, v_{Hk}, it follows:

$$v_s = \sum_{k=1}^{4} v_{H_k} \qquad\qquad k = \{1,\ 2,\ 3,\ 4\} \tag{4.2a}$$

$$v_s = \sum_{k=1}^{4} \sum_{m=1}^{\infty} \left(a_{km} \cos\left(m\omega t\right) + b_{km} \sin\left(m\omega t\right)\right) k = \{1,\ 2,\ 3,\ 4\}\,,\ m = \{1,\ 2\cdots\} \tag{4.2b}$$

$$v_s = \sum_{k=1}^{4} \sum_{m=1}^{\infty} \frac{4v_{ek}}{m\pi} \cos\left(m\theta_k\right) \sin\left(m\omega t\right) \qquad k = \{1,\ 2,\ 3,\ 4\}\,,\ m = \{1,\ 3\ \cdots\} \tag{4.2c}$$

$$v_s = \sum_{m=1}^{\infty} \underbrace{\left(\frac{4}{m\pi} \sum_{k=1}^{4} \left(v_{ek} \cos\left(m\theta_k\right)\right) \sin\left(m\omega t\right)\right)}_{h_m} k = \{1,\ 2,\ 3,\ 4\}\,,\ m = \{1,\ 3\ \cdots\} \tag{4.2d}$$

According to (4.2) the mth Fourier components (h_m) of v_s, when m is odd, is defined as:

$$h_m = \frac{4}{m\pi} \sum_{k=1}^{4} \left(v_{ek} \cos(m\theta_k)\right) \tag{4.3}$$

Considering that CEMI is symmetric, all the sources should be the same. However, in practice small differences in the input voltage sources can be considered as disturbances:

$$v_{ek} = v_e(1 + \delta_k) \tag{4.4}$$

Therefore,

$$h_m = \frac{4v_e}{m\pi} \sum_{k=1}^{4} \left((1 + \delta_k) \cos(m\theta_k)\right) \tag{4.5}$$

SHE strategy finds the switching angles that satisfies (4.5) for $m = \{1,\ 3,\ 5,\ 7\}$, for a fundamental component $h_1 = h_{ref_1}$ and $h_3 = h_5 = h_7 = 0$. Many methods find the switching angles for SHE as numeric methods [38], intelligent methods [14, 37, 41] and algebraic methods [15, 42, 44, 58]. All these methods find the switching angles with pre-processing techniques because the solving processes take considerable processing time. However, if there is a disturbance in one of the input voltages, the harmonics change. For that reason, this work proposes a control law, that uses the algebraic solving method that [43, 44, 58] describe, which consists in to transform the trigonometric equation system into a polynomial one, using the multiple-angle formula, that is $\cos(m\theta) = T_m(\cos(\theta))$, where $T_m(\bullet)$ is the Chebyshev polynomial of the first kind of mth degree

which is defined as:

$$
\begin{aligned}
T_0(x) &= 1 \\
T_1(x) &= x \\
T_{m+1}(x) &= 2xT_m(x) - T_{m-1}(x)
\end{aligned}
\tag{4.6}
$$

then:

$$
h'_m = \frac{4}{m\pi} \sum_{k=1}^{4} (1 + \delta_k) T_m(x_k)
\tag{4.7}
$$

where $x_k = \cos(\theta_k)$ and h'_m is the normalized harmonic defined as $h'_m = \dfrac{h_m}{v_e}$. Reference [59] describes in detail about Chebyshev polynomials in trigonometric equation systems. As mentioned previously, the aims of this strategy are to adjust the fundamental component and to eliminate the most significant harmonics. In this work, those harmonics correspond to the first 3 odd harmonics. Therefore, expanding $T_m(x_k)$ for $m = \{1,\ 3,\ 5,\ 7\}$:

$$
\begin{aligned}
h'_1 &= \frac{4}{\pi} \sum_{k=1}^{4} (1 + \delta_k) x_k \\
h'_3 &= \frac{4}{3\pi} \sum_{k=1}^{4} (1 + \delta_k) \left(4x_k^3 - 3x_k \right) \\
h'_5 &= \frac{4}{5\pi} \sum_{k=1}^{4} (1 + \delta_k) \left(16x_k^5 - 20x_k^3 + 5x_k \right) \\
h'_7 &= \frac{4}{7\pi} \sum_{k=1}^{4} (1 + \delta_k) \left(64x_k^7 - 112x_k^5 + 56x_k^3 - 7x_k \right)
\end{aligned}
\tag{4.8}
$$

Expressing as a matrix form:

$$
\underbrace{\begin{bmatrix} h'_1 \\ h'_3 \\ h'_5 \\ h'_7 \end{bmatrix}}_{\mathbf{H'_R}} = \frac{4}{\pi} \underbrace{\begin{bmatrix} T_1(x_1) & T_1(x_2) & T_1(x_3) & T_1(x_4) \\ \frac{1}{3}T_3(x_1) & \frac{1}{3}T_3(x_2) & \frac{1}{3}T_3(x_3) & \frac{1}{3}T_3(x_4) \\ \frac{1}{5}T_5(x_1) & \frac{1}{5}T_5(x_2) & \frac{1}{5}T_5(x_3) & \frac{1}{5}T_5(x_4) \\ \frac{1}{7}T_7(x_1) & \frac{1}{7}T_7(x_2) & \frac{1}{7}T_7(x_3) & \frac{1}{7}T_7(x_4) \end{bmatrix}}_{\mathbf{\Pi(X)}} \left(\underbrace{\begin{bmatrix} 1 \\ 1 \\ 1 \\ 1 \end{bmatrix}}_{\mathbf{V_1}} + \underbrace{\begin{bmatrix} \delta_1 \\ \delta_2 \\ \delta_3 \\ \delta_4 \end{bmatrix}}_{\mathbf{\Delta}} \right)
\tag{4.9}
$$

Where $\mathbf{X} = \begin{bmatrix} x_1 & x_2 & x_3 & x_4 \end{bmatrix}^T$. Eq. (4.9) corresponds to a static model of the system of the Fourier components as a function of the cosine of the switching angles $\mathbf{X}$.

It can be observed that (4.8) is less complicated to solve than (4.5). However, it can be complex, if the disturbances δ_ks are high. Furthermore, solving (4.8) in real-time might take considerable processing time. To solve this system, $\mathbf{H'_e}$ is defined as the estimated harmonics, corresponding to the harmonics if there are no disturbances, hence:

$$\mathbf{H'_R} = \mathbf{\Pi(X)(V_1 + \Delta)} \tag{4.10a}$$

$$\mathbf{\Pi(X)V_1} = \mathbf{H'_e} \tag{4.10b}$$

The next subsection focuses on the process to solve (4.10b). Then, with the closed-loop the disturbances in the input voltages are compensated, satisfying (4.10a).

4.1.2 Solving the Polynomial equation

Notice that (4.10b) corresponds to a polynomial equation system, which is non-linear because it is "polynomial". If the objective is to find the cosine of the switching angles, x_k, the input variables are the harmonics, h_m, and the output variables are the cosine of the switching angles, x_ks.

It can be observed in (4.9), that all the equations present all the output variables, x_ks, meaning that the equation system is coupled. Furthermore, there is no manner to leave the output variables, x_ks, as a function of the input variables, h_ms. It means that the system is implicit. Finally, it can be observed that this equation system is static because the time is not present in the equation system. It can be concluded that the equation system described in (4.9) corresponds to a static, non-linear, coupled, implicit model.

This work uses an algebraic method that converts (4.9) into its Groebner Basis, decoupling the equations, finding another polynomial equation system with the same solution set, where the coefficients are other polynomial functions of $\mathbf{H'_e}$. The polynomial obtained of the Groebner basis conversion follows the form:

$$
\begin{aligned}
p_1(x_1, \mathbf{H'_e}) &= 0 \\
p_2(x_1, x_2, \mathbf{H'_e}) &= 0 \\
&\vdots \\
p_N(x_1, x_2, \cdots x_N, \mathbf{H'_e}) &= 0
\end{aligned}
\tag{4.11}
$$

Appendix D shows the Groebner basis conversion of (4.10b). This conversion aims to decouple the output variable x_ks, simplifying the solving process of the system. References [45, 58] explain in more detail this polynomial conversion. Additionally, according to [42, 43], (4.8) is made of symmetric polynomials, meaning that if a permutation of x_ks is carried out, the polynomial equation system has the same solution set. It means that the solution set of any x_k is a permutation of the solution set of x_1. For that reason, solving $p_1(x_1, \mathbf{H'_e})$, the solutions of the others x_ks are also found. Therefore, it

is possible to define a system as:

$$q(x_1, \mathbf{H'_e}) = 0$$
$$\vdots \tag{4.12}$$
$$q(x_N, \mathbf{H'_e}) = 0$$

where $q(x_k, \mathbf{H'_e}) = p_1(x_k, \mathbf{H'_e})$. According to Appendix D, $q(x_k, \mathbf{H'_e})$, it follows:

$$p_1(x_k, \mathbf{H'_e}) \sum_{r=0}^{4} g_r(\mathbf{H'_e}) x_k^r = 0 \tag{4.13}$$

where:

$$
\begin{aligned}
g_4(\mathbf{H'_e}) =& 26.88\pi^4 {h'_{e_1}}^6 - 16128\pi^2 {h'_{e_1}}^4 - 16128\pi^2 {h'_{e_1}}^3 h'_{e_3} + 193536 {h'_{e_1}}^2 + 193536 h'_{e_1} h'_{e_3} \\
& + 193536 h'_{e_1} h'_{e_5} - 193536 {h'_{e_3}}^2
\end{aligned}
$$

$$
\begin{aligned}
g_3(\mathbf{H'_e}) =& - 67.2\pi^5 {h'_{e_1}}^7 + 4032\pi^3 {h'_{e_1}}^5 + 4032\pi^3 {h'_{e_1}}^4 h'_{e_3} - 48384\pi {h'_{e_1}}^3 - 48384\pi {h'_{e_1}}^2 h'_{e_3} \\
& - 48384\pi {h'_{e_1}}^2 h'_{e_5} + 48384\pi h'_{e_1} {h'_{e_3}}^2
\end{aligned}
$$

$$
\begin{aligned}
g_2(\mathbf{H'_e}) =& 7.2\pi^6 {h'_{e_1}}^8 - 604.8\pi^4 {h'_{e_1}}^6 - 604.8\pi^4 {h'_{e_1}}^5 h'_{e_3} + 16128\pi^2 {h'_{e_1}}^4 + 24192\pi^2 {h'_{e_1}}^3 h'_{e_3} \\
& + 8064\pi^2 {h'_{e_1}}^3 h'_{e_5} - 145152 {h'_{e_1}}^2 - 193536 h'_{e_1} h'_{e_3} - 193536 h'_{e_1} h'_{e_5} - 48384 h'_{e_1} h'_{e_7} \\
& + 145152 {h'_{e_3}}^2 + 48384 h'_{e_3} h'_{e_5}
\end{aligned}
$$

$$
\begin{aligned}
g_1(\mathbf{H'_e}) =& - 0.4\pi^7 {h'_{e_1}}^9 + 50.4\pi^5 {h'_{e_1}}^7 + 50.4\pi^5 {h'_{e_1}}^6 h'_{e_3} - 2016\pi^3 {h'_{e_1}}^5 - 3024\pi^3 {h'_{e_1}}^4 h'_{e_3} \\
& - 1008\pi^3 {h'_{e_1}}^4 h'_{e_5} + 24192\pi {h'_{e_1}}^3 + 24192\pi {h'_{e_1}}^2 h'_{e_3} + 36288\pi {h'_{e_1}}^2 h'_{e_5} \\
& + 12096\pi {h'_{e_1}}^2 h'_{e_7} - 36288\pi h'_{e_1} {h'_{e_3}}^2 - 24192\pi h'_{e_1} h'_{e_3} h'_{e_5} + 12096\pi {h'_{e_3}}^3
\end{aligned}
$$

$$
\begin{aligned}
g_0(\mathbf{H'_e}) =& + 0.01\pi^8 {h'_{e_1}}^{10} - 1.8\pi^6 {h'_{e_1}}^8 - 1.8\pi^6 {h'_{e_1}}^7 h'_{e_3} + 100.8\pi^4 {h'_{e_1}}^6 + 151.2\pi^4 {h'_{e_1}}^5 h'_{e_3} \\
& + 50.4\pi^4 {h'_{e_1}}^5 h'_{e_5} - 2016\pi^2 {h'_{e_1}}^4 - 3024\pi^2 {h'_{e_1}}^3 h'_{e_3} - 2016\pi^2 {h'_{e_1}}^3 h'_{e_5} - 1008\pi^2 {h'_{e_1}}^3 h'_{e_7} \\
& + 3024\pi^2 {h'_{e_1}}^2 h'_{e_3} h'_{e_5} - 30.24\pi^2 h'_{e_1} {h'_{e_3}}^3 + 12096 {h'_{e_1}}^2 + 24192 h'_{e_1} h'_{e_3} + 12096 h'_{e_1} h'_{e_5} \\
& + 12096 h'_{e_7} h'_{e_1} - 12096 h'_{e_3} h'_{e_5} + 12096 h'_{e_3} h'_{e_7} - 12096 {h'_{e_5}}^2
\end{aligned}
$$

Expressing (4.12) a matrix form, it follows:

$$\mathbf{Q}(\mathbf{X}, \mathbf{H'_e}) = 0 \tag{4.14}$$

The roots of (4.14) corresponds to the solution of all the cosine of the switching angles. In order to validates the equation for this application lets define $v_e = 48\ V$, a desired fundamental component (h_1) equals $155\ V$, therefore $h'_{e_1} = 3.23$ and h'_{e_5}, h'_{e_3}, $h'_{e_7} = 0$. Replacing the values of the normalized harmonics, the solutions of this equation are: $x_1 = 0.9842$, $x_2 = 0.8958$, $x_3 = 0.6187$, $x_4 = 0.0468$, then the switching angles are: $\theta_1 = 0.1780\ rads$, $\theta_2 = 0.4606\ rads$, $\theta_3 = 0.9037\ rads$ $\theta_4 = 1.5240\ rads$. Fig. 4.1(a) shows the waveform of v_s, v_{H_1}, v_{H_2}, v_{H_3} and v_{H_4} with the respective switching angles, and Fig. 4.1(b) shows the Fourier analysis of v_s. Notice that the harmonics 3rd, 5th and 7th are eliminated, while the fundamental value is the desired one.
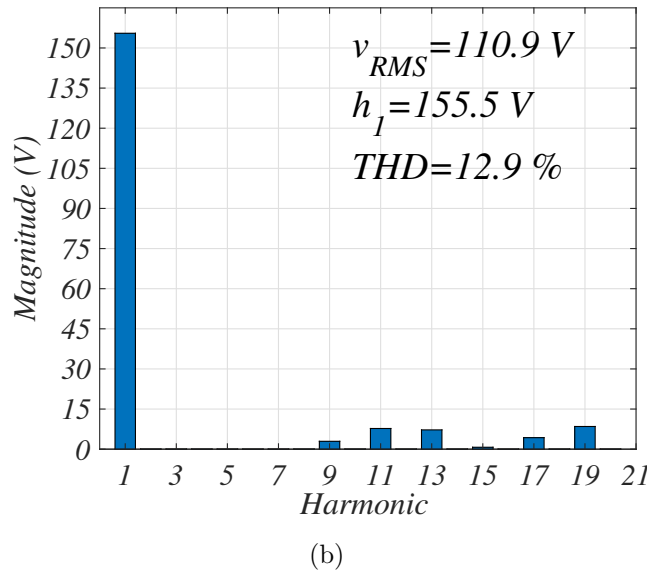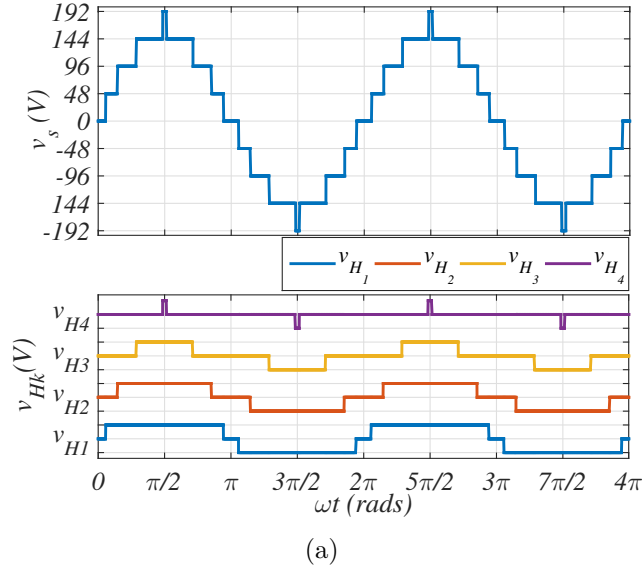
Figure 4.1: (a) Waveform of $v_s, v_{H1}, v_{H2}, v_{H3}, v_{H4}$, (b) Fourier analysis of v_s

4.2 Analyzing the solutions

This section carries out three analyses of the system described in (4.14). The first analysis corresponds to the study of the behavior of the cosine of the switching angles, $\mathbf{X}$, vs the normalized fundamental component, h'_1, when the harmonics 3, 5 and 7 are equal to 0. The second study describes the behavior of the normalized Harmonics, $\mathbf{H'_R}$ vs small changes in the cosine of the angles, $\mathbf{X}$, and the last study explains how do the harmonics, $\mathbf{H'_R}$, are, when changes in δ_k occur.

4.2.1 Behavior of the X when h'_1 changes

In Fig. 4.1 it can be seen that all the FBs present a positive step in the first quarter of a cycle. However, for different fundamental components, some x_ks can be negatives, greater than 1, lower than -1 or even complex. This subsection analyzes how does **X** change according to the fundamental component.

In order to analyze the behavior of the solution set when the system eliminates $h'_{e_3}, h'_{e_5}, h'_{e_7}$, Fig. 4.3 shows **X** vs h'_{e_1} when the harmonics 3, 5, and 7 are zero.
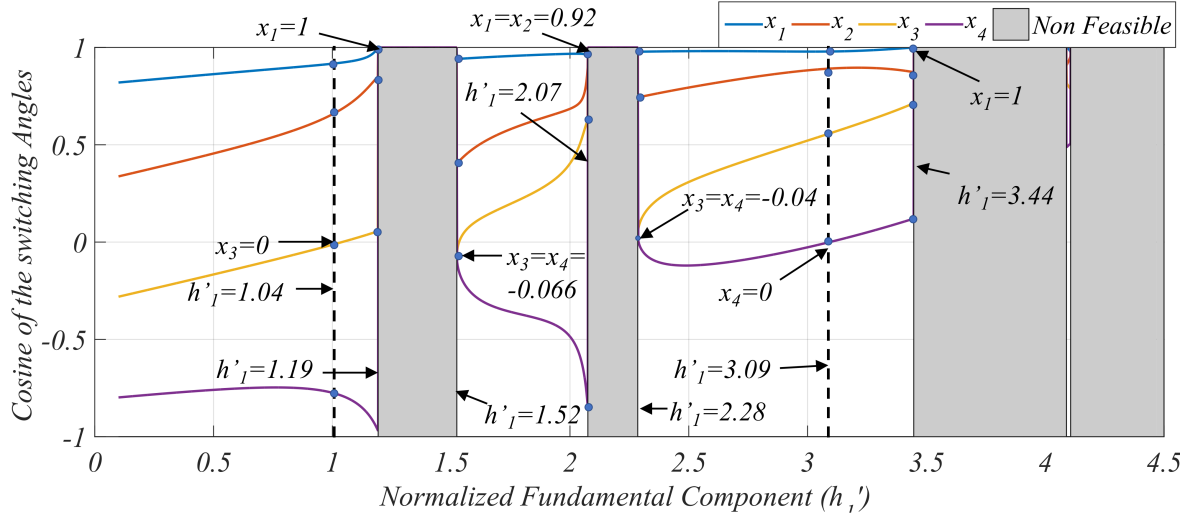
Figure 4.2: **X** vs h'_1, when h'_3, h'_5, h'_7 are 0

According to Fig. 4.3, there exists three regions where there is no feasible solution of the system ($1.19 < h'_{e1} < 1.52$; $2.07 < h'_{e1} < 2.28$ and $h'_{e1} > 3.44$). This fact is produced because one x_k is complex, higher than 1 or lower than -1. It has to remain that if $|x_k| > 1$ or if x_k is complex, the associated switching angle, θ_k, is complex.

Fig. 4.2 also shows that there are three regions where some x_ks are negatives, producing a switching angle greater than $\pi/2$ generating a negative step in v_{H_k} during the first quarter of a cycle.

In order to understand more clearly this phenomenon, Fig. 4.3 shows the behavior of the waveform if $x_k < 0$ or not.
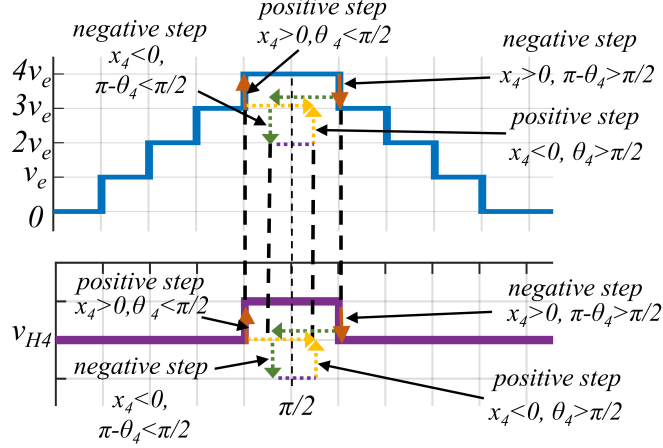
Figure 4.3: waveform of v_s and v_{H4}, displacing x_4

It can be inferred that when one x_k is negative the waveform of v_s decreases 2 levels, one for the positive part and one in the negative one, meaning that one step is negative in the positive semi cycle. Based on this analysis, applying the proposed theory, the number of levels is not important and only the number of switching per quarter of cycles is.

For the cases when **X** are complexes, lower than -1 or higher than 1, there are no switching angles that satisfy the desired h'_{e_1} and the nullity of $h'_{e_3}, h'_{e_5}, h'_{e_7}$.

All this research is validated in the feasible region $2.28 < h'_{e_1} < 3.44$. However, this theory can be implemented in the other regions. Notice that in this region the cosine of the switching angle θ_4, x_4, can be negative, while the other cosines, x_k, do not, being able to produce 7 or 9 levels, according to the fundamental component.

In order to proof that the Groebner conversion is valid for cases where $x_4 < 0$ and the step of v_{H4} in the first quarter of cycle is negative. Fig. 4.4 shows v_s and v_{H_k} when $v_e = 54\ V$ and $h_1 = 155.5\ V$. With these parameters $h'_{e_1} = 2.88$ and the solution set of **X** is: $x_1 = 0.9797$, $x_2 = 0.8661$, $x_3 = 0.4744$, $x_4 = -0.0582$, generating a switching angles of: $\theta_1 = 0.2020\ rads$, $\theta_2 = 0.5235\ rads$, $\theta_3 = 1.0765\ rads$, $\theta_4 = 1.629\ rads$, being the last commutation a negative step in FB_4 during the first quarter of cycle. Notice that v_{H_4} starts with a negative step and v_s has 2 levels less than the v_s previously shown in Fig. 4.1. In order to validate these results, Fig. 4.4(b) shows the Fourier analysis of Fig. 4.4(a), where the fundamental component does not change and the harmonics h'_{e_3}, h'_{e_5}, h'_{e_7} are eliminated again. This result indicates that it is possible to analyze mathematically this system according to the number of switching angles without taking into account the number of FBs, knowing that $x_k > 0$ produces a positive step in the first quarter of cycle and $x_k < 0$ produces a negative step in the first quarter of cycle. Nevertheless, the THD is higher than when v_s has 7 levels than when v_s has 9 levels. Additionally, the harmonics 9 and 15 are lower for v_s of 9 levels than v_s for 7 levels.

(a)

v_{RMS}=111.44 V

h_1=155.51 V

THD=16.45 %
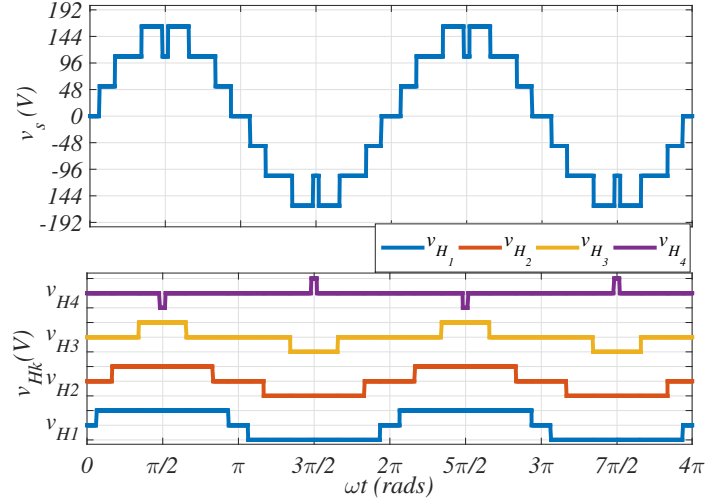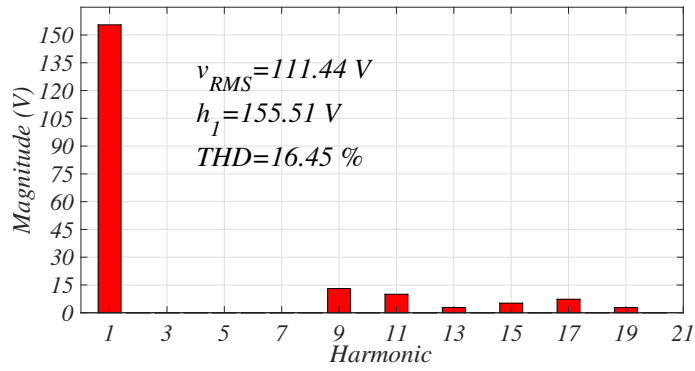
(b)

Figure 4.4: (a) Waveform of $v_s, v_{H1}, v_{H2}, v_{H3}, v_{H4}$, when $\theta_4 > \pi/2$ (b) Fourier analysis of v_s when $\theta_4 > \pi/2$

4.2.2 Sensitivity of the system

This subsection analyzes the changes of the outputs, produced by changes in the cosine of the switching angles, x_k for $k = \{1, 2, 3, 4\}$. Fig.4.5 shows the changes of h'_1, and Fig. 4.6 shows the changes in the harmonics h_m, $m = \{1, 3, 5, 7\}$. Notice that the fundamental component are linear with respect to all the cosine of the switching angles, x_k. In contrast, the harmonics are nonlinear with respect to the cosine of the switching angles, even having locals maximum and minimum.
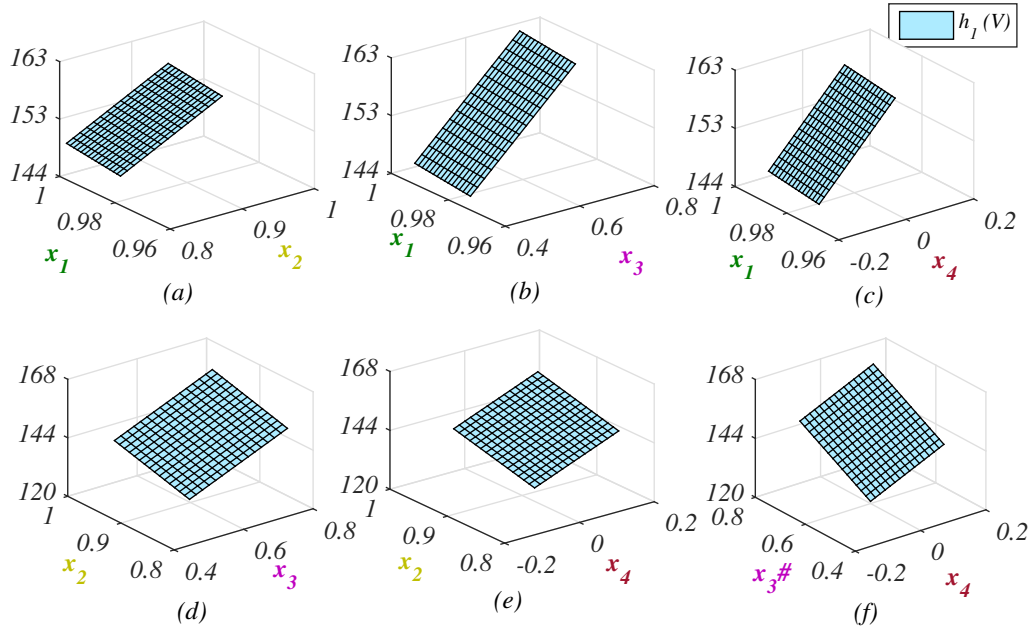
Figure 4.5: Behavior of h_1 vs cosine of switching angles x_k. (a) h_1 vs x_1 and x_2 (b) h_1 vs x_1 and x_3 (c) h_1 vs x_1 and x_4 (d) h_1 vs x_2 and x_3 (e) x_2 and x_4 (f) h_1 vs x_4 and x_3
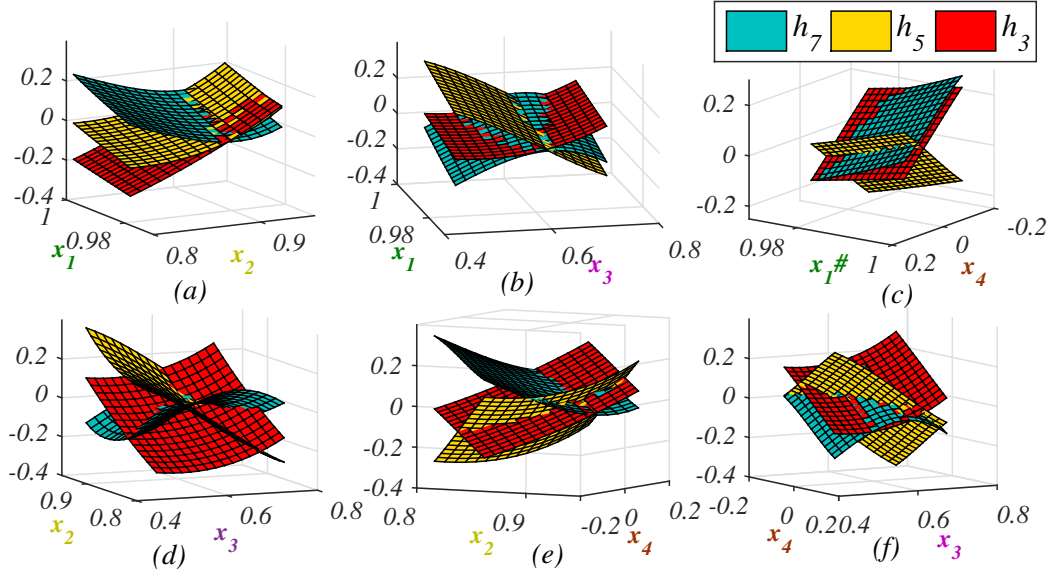
Figure 4.6: Behavior of the harmonics h_3, h_5, h_7 vs cosine of switching angles x_k. (a) harmonics vs x_1 and x_2 (b) harmonics vs x_1 and x_3 (c) harmonics vs x_1 and x_4 (d) harmonics vs x_2 and x_3 (e) harmonics vs x_2 and x_4 (f) harmonics vs x_4 and x_3

It can be seen in Figs. 4.6b, 4.6d, 4.6f that h_3 is nonlinear with respect to x_3, while in Figs. 4.6a, 4.6d, 4.6e, h_5 is nonlinear with respect to x_2. Finally, in Figs. 4.6a, 4.6b, 4.6d, 4.6e and 4.6f, h_7 is highly nonlinear respect to x_2 and x_3. It can be inferred that there is a linear relationship between all the harmonics and x_1, x_4, meaning that x_4 and x_1 are linear with respect to all the harmonics. This conclusion can be very useful to simplify any control method. Furthermore, a maximum or minimum point of the harmonics in the graphics means that the sensitivity changes its sing. This fact has to be taken into account in the design of the controller, because a typical linear controller without anything else produces that the system turns unstable.

4.2.3 Behavior of the harmonics with changes in v_{ek}

This subsection shows the effects produced in the harmonics when changes in the input voltages are carried out. The gradient of (4.10a) with respect to $\mathbf{\Delta}$ is:

$$\frac{\partial \mathbf{H_R}}{\partial \mathbf{\Delta}} = \mathbf{\Pi}(\mathbf{X}^*) \tag{4.15}$$

where $\mathbf{X}^*$ are the solution set that satisfies the desired estimated harmonics $\mathbf{H'_e}$, meaning that the changes in the harmonics produced by changes in the sources are linear.

Based on all these analyses, the control loop is proposed in the next section.

4.3 Closing the loop

Based on the three analyses, this section proposes a control law to ensure a desired fundamental component and the nullity of some predefined harmonics, if a disturbance in the sources occurs or if a voltage drop in the output exists due to a change in the load. According to (4.5) and (4.10) the system is modeled as static one as:

$$\mathbf{Q}(\mathbf{X}, \mathbf{H'_e}) = 0 \tag{4.16a}$$

$$\mathbf{H'_R} = \mathbf{\Pi}(\mathbf{X})(\mathbf{V_1} + \mathbf{\Delta}) \tag{4.16b}$$

The system is composed of two parts. The first stage, (4.16a), that based on $\mathbf{Q}(\mathbf{X}, \mathbf{H'_e})$ obtains a solution set of $\mathbf{X}$, receiving the estimated harmonics, $\mathbf{H'_e}$, as input. The second stage of the system, described by (4.16b), corresponds to the computation of the switching angles based on its cosines, $\mathbf{X}$, and applying them to the inverter, generating the output voltage, v_s, which is captured in the Digital Signal Processor (DSP). Then the harmonics of v_s are computed and normalized, dividing them by the nominal value of the input voltages, v_e, obtaining the normalized harmonics components, $\mathbf{H'_R}$. Fig. 4.7 shows the schematics of the implemented system and the static model that represents it.
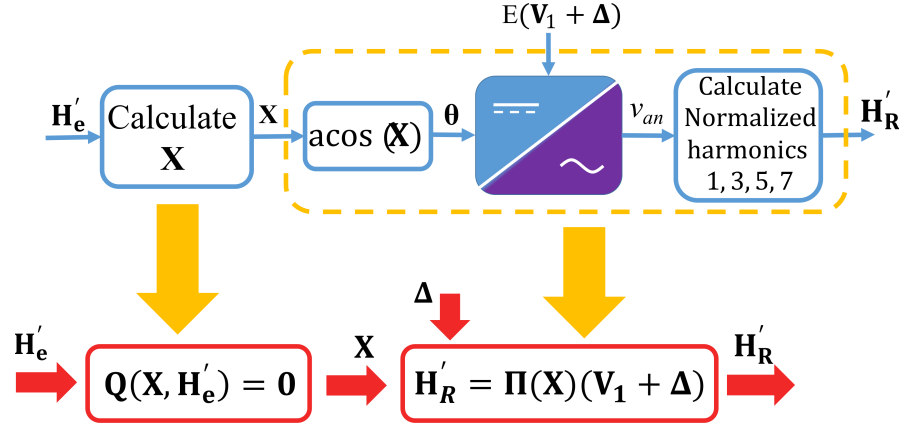
Figure 4.7: static model and block diagram of the system

In Fig. 4.7, the input of the system is $\mathbf{H'_e}$, the output is $\mathbf{H'_R}$ and the internal variable is $\mathbf{X}$. Furthermore, the model obtained in (4.16) is a static one and also is non-linear because it is composed of $\mathbf{Q}(\mathbf{X}, \mathbf{H'_e})$, which is a polynomial system. Additionally, $\mathbf{Q}(\mathbf{X}, \mathbf{H'_e}) = 0$ is an implicit system equation. For designing a controller it is necessary to obtain an explicit and dynamical model. For converting this model into an explicit one, $\mathbf{X}$ is found from $\mathbf{Q}$ applying the same principle of the Newton Rapson (NR) method, for solving nonlinear system equation, with adaptations, because $\mathbf{H'_e}$ behaves as a variable parameter and not as a fixed one. Therefore:

$$\mathbf{Q_t}^{\cancel{0}} = \mathbf{Q_{t-1}} + \left(\left. \frac{\partial \mathbf{Q}}{\partial \mathbf{X}} \right|_{t-1} \right) (\mathbf{X}_t - \mathbf{X}_{t-1}) + \left(\left. \frac{\partial \mathbf{Q}}{\partial \mathbf{H'_e}} \right|_{t-1} \right) \left(\mathbf{H'_{et}} - \mathbf{H'_{et-1}} \right) \qquad (4.17)$$

Hence,

$$\mathbf{X_t} = \underbrace{\mathbf{X_{t-1}} - \left(\left. \frac{\partial \mathbf{Q}}{\partial \mathbf{X}} \right|_{t-1} \right)^{-1} \left(\mathbf{Q_{t-1}} + \left(\left. \frac{\partial \mathbf{Q}}{\partial \mathbf{H'_e}} \right|_{t-1} \right) \left(\mathbf{H'_{et}} - \mathbf{H'_{et-1}} \right) \right)}_{\mathbf{F}(\mathbf{X}_{t-1}, \mathbf{H'_{et}}, \mathbf{H'_{et-1}})} \qquad (4.18)$$

According to (4.18), if the harmonics do not change, the equation corresponds to the solving process of the NR method. Hence, the new system corresponds to a *virtual dynamical system* composed of the equation system that finds the cosine of the switching angles, $\mathbf{X}$, by the adaptation of NR; and the static and explicit system equation that represents the obtention of the switching angles, θ_ks, based on its cosines, x_ks, the sensed of the output voltage, v_s, of the inverter, and the computation of the normalized harmonics, $\mathbf{H'_R}$, of the output voltage, v_s. Equation (4.19) shows the proposed dynamical model of the system.

$$\begin{bmatrix} \mathbf{X}_t \\ \mathbf{H'_{R}}_t \end{bmatrix} = \begin{bmatrix} \mathbf{F}(\mathbf{X}_{t-1}, \mathbf{H'_{et}}, \mathbf{H'_{et-1}}) \\ \Pi(\mathbf{X}_t)(\mathbf{V_1} + \boldsymbol{\Delta}) \end{bmatrix} \qquad (4.19)$$

Fig.4.8 expresses as a block diagram of (4.19)
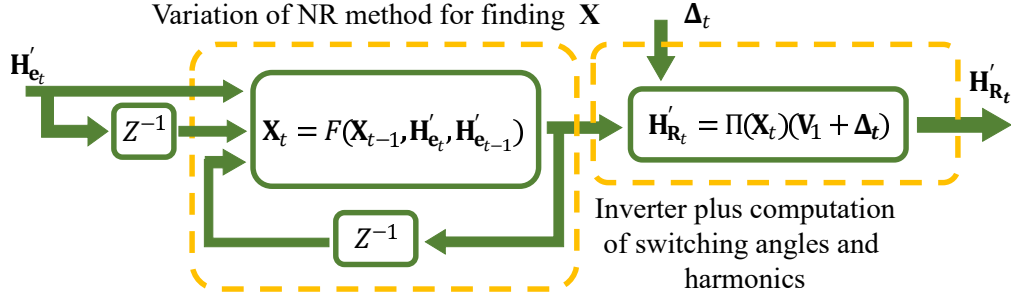
Figure 4.8: *virtual* dynamic model of the system

According to Fig. 4.8, the input of the dynamic system is the normalized estimated harmonic, $\mathbf{H'_e}$, and the output of the system is the sensed normalized harmonics, $\mathbf{H'_R}$. Based on this model, the proposed control law is composed of the desired normalized harmonics plus a discrete PI controller, as (4.20) shows.

$$\mathbf{H'_{et}} = \mathbf{H'_{ref}} + a_1\boldsymbol{\xi}_t - a_0\boldsymbol{\xi}_{t-1} \tag{4.20}$$

where $\boldsymbol{\xi}_t = \mathbf{H_{ref}} - \mathbf{H_R}t$. Fig. 4.9 shows the block diagram of the closed-loop system.
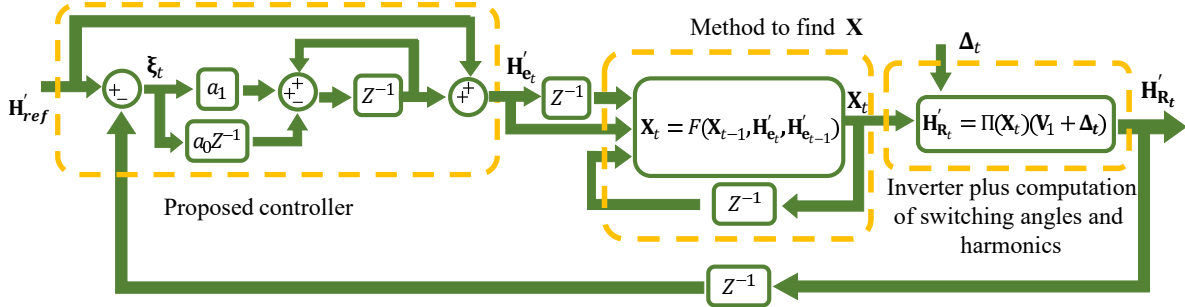
Figure 4.9: System in closed-loop system

Based on the closed-loop diagram represented in Fig. 4.9, inserting the control law in (4.18), it follows:

$$\mathbf{X_t} = \mathbf{X_{t-1}} - \left(\left.\frac{\partial \mathbf{Q}}{\partial \mathbf{X}}\right|_{t-1}\right)^{-1}\left(\mathbf{Q}_{t-1} + \left(\left.\frac{\partial \mathbf{Q}}{\partial \mathbf{H'_e}}\right|_{t-1}\right)\left(\cancel{\mathbf{H'_{ref}}} + a_1\boldsymbol{\xi}_t - a_0\boldsymbol{\xi}_{t-1}\right.\right.$$
$$\left.\left. - \cancel{\mathbf{H'_{ref}}} - a_1\boldsymbol{\xi}_{t-1} + a_0\boldsymbol{\xi}_{t-2}\right)\right)$$

$$\mathbf{X_t} = \mathbf{X_{t-1}} - \left(\left.\frac{\partial \mathbf{Q}}{\partial \mathbf{X}}\right|_{t-1}\right)^{-1}\left(\mathbf{Q}_{t-1} + \left(\left.\frac{\partial \mathbf{Q}}{\partial \mathbf{H'_e}}\right|_{t-1}\right)\left(\cancel{a_1\mathbf{H'_{ref}}} - a_1\mathbf{H'_{R}}_t\right.\right. \tag{4.21}$$
$$\left.\left. - \cancel{a_0\mathbf{H'_{ref}}} + a_0\mathbf{H'_{R}}_{t-1} - \cancel{a_1\mathbf{H'_{ref}}} + a_1\mathbf{H'_{R}}_{t-1} + \cancel{a_0\mathbf{H'_{ref}}} - a_0\mathbf{H'_{R}}_{t-2}\right)\right)$$

Hence, the closed-loop system is:

$$\mathbf{X_t} = \mathbf{X_{t-1}} - \left(\left.\frac{\partial \mathbf{Q}}{\partial \mathbf{X}}\right|_{t-1}\right)^{-1}\left(\mathbf{Q}_{t-1} - \left(\left.\frac{\partial \mathbf{Q}}{\partial \mathbf{H'_e}}\right|_{t-1}\right)\left(a_1\mathbf{H'_{R}}_t - (a_1 + a_0)\,\mathbf{H'_{R}}_{t-1}\right.\right.$$
$$\left.\left. + a_0\mathbf{H'_{R}}_{t-2}\right)\right) \tag{4.22}$$
$$\mathbf{H_{R_t}} = \mathbf{\Pi}(\mathbf{X}_t)(\mathbf{V_1} + \boldsymbol{\Delta})$$

Notice that, when the angles are found, $\mathbf{Q}_t = 0$ and the harmonics do not change. Hence, $\mathbf{X}$ does not change, meaning that the system reaches the steady-state. Note, that this controller works only in feasible regions of Fig.4.2 and is not able to pass from one feasible region to another one.

To validate this control law, the next section shows the simulation and experimental tests.

4.4 Results

The results correspond to simulation and experimental tests, developed with a prototype with the parameters described in table 4.1.

Table 4.1: Parameters of the inverter

Parameter	Value	Parameter	Value
v_e	48 V	R_x	100 mΩ
L_k	1.8 mH	R_o	52 Ω
R_{L_k}	200 mΩ	$h_{1_{ref}}$	145 V
R_s	200 mΩ	P_o	200 W
C_k	4 mF	a_1	0.12
R_{DS}	58 mΩ	a_0	0.012

where R_{L_k} is the DC Resistance (DCR) of the inductance L_k. P_o is the output power, R_{DS} is the series ON resistance of the MOSFETs (IRFI4212). R_s and R_x are the resistances associated with the wires in the input of each FB, and in the output of the inverter, respectively. Fig. 4.10 shows the prototype where the experimental tests are developed.
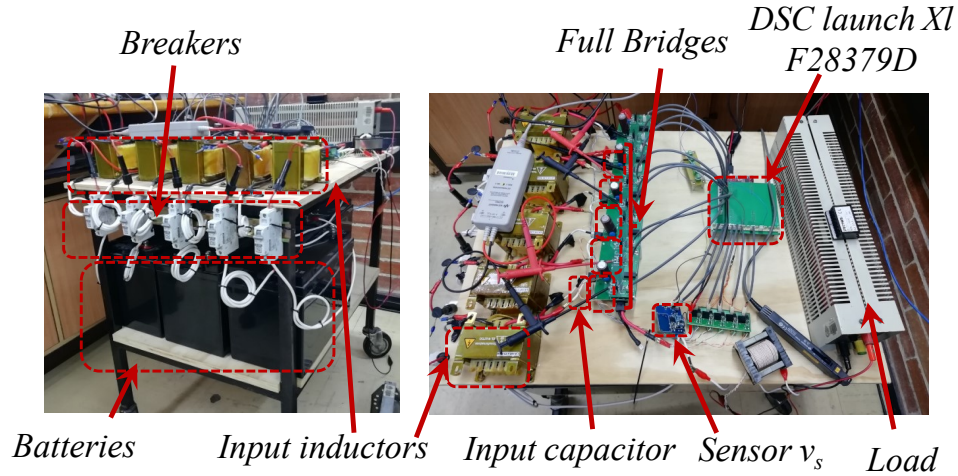
Figure 4.10: Prototype of 200 W, $v_e = 48V$, 5 cells

The sampling frequency of the acquisition of the output voltage, v_s, is 15 kHz and the frequency of the fundamental component is 60 Hz. To obtain the harmonics, the output voltage is captured during 20 periods of v_s, meaning that the time of the acting of the controller is 3 Hz. This is carried out because according to the signal processing theory shown in [60], for having a good accuracy, the acquisition frequency of a periodic signal, must be 10 times less than the minimum frequency of the Fourier components to be obtained.

The tests developed in simulation and experimental correspond to an insertion of a load and a disturbance in one of the input voltages, as will be shown in the following subsections.

4.4.1   Insertion of a 200 W load

These tests show the simulation and experimental results of the system, starting with no load and inserting a load of 200W at t=7.5 seconds. Fig. 4.11 shows the simulation result. Notice that before the load insertion, there is a negative step in the output voltage of FB_4, v_{H4}, during the positive semi-cycle of v_s, meaning that x_4 must be negative and $\theta_4 > \pi/2$. When the load is inserted, there is a drop in the amplitude of the waveform because the impedance of the system starts to generate losses. Due to this action, the controller compensates the amplitude of v_s, adjusting the $\mathbf{X}$, especially x_4, passing from a negative value to a positive one.
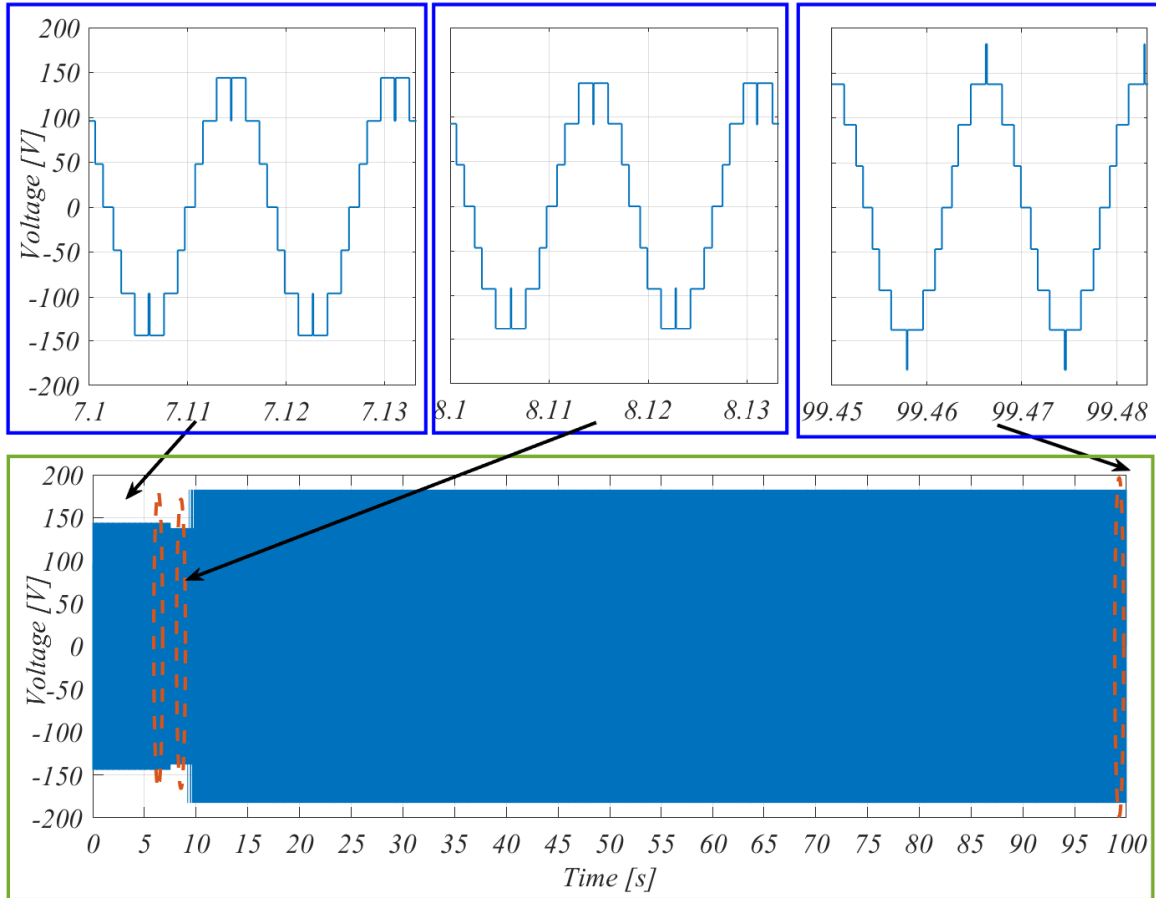
Figure 4.11: Simulation result of 200 W load insertion

To validate the result of the controller, Fig. 4.12 shows the behavior of the harmonics 3, 5, 7 and the fundamental component. In Fig. 4.12, it can be observed that h_1 presents an undershoot due to the load insertion, and a settling time of 12.5 seconds, approximately. Additionally, Fig. 4.12 shows that h_3 presents a small overshoot during the load insertion. However, it maintains a low value during the test. h_5 and h_7 are not affected by the load insertion and are maintained close to 0 during the test. Note that all the harmonics are between 0 and 0.5 V, which represents less than 0.34% of the fundamental component.
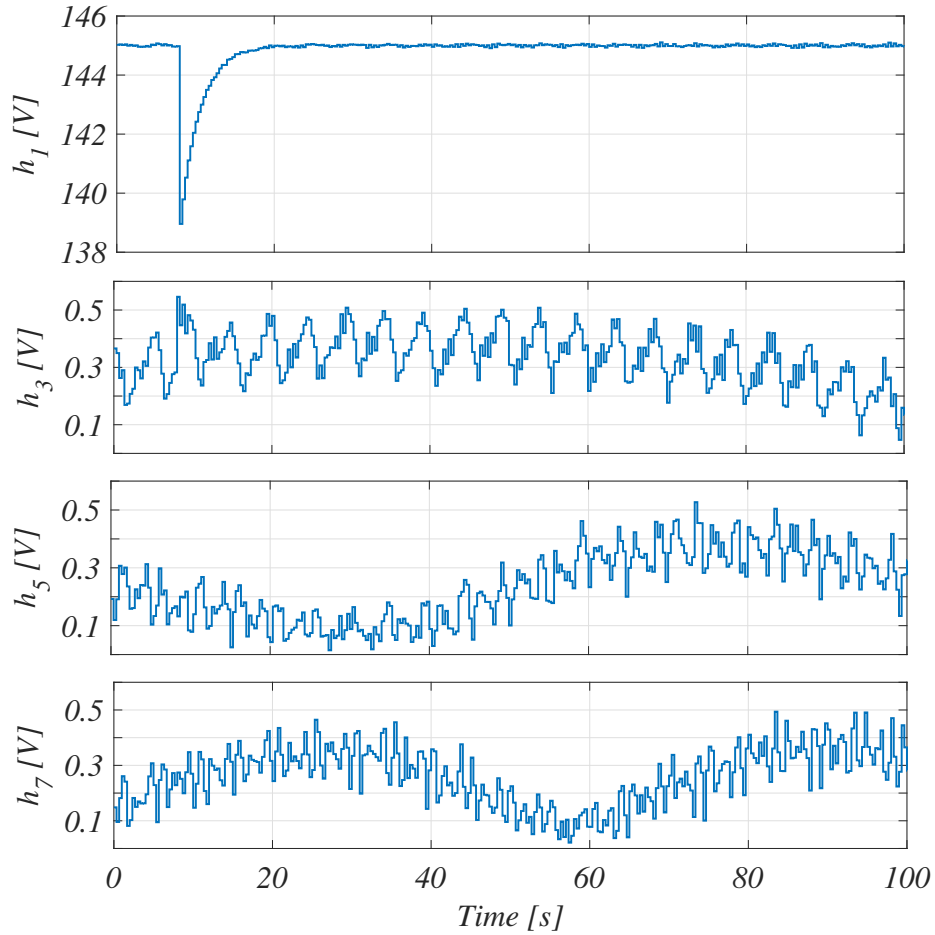
Figure 4.12: Harmonics behavior of the 200 W load simulation test

To validate the behavior of the cosine of the switching angles, Fig. 4.13 shows $\mathbf{X}$ during the simulation. As mentioned previously, before the load insertion, x_4 is negative and after the insertion, x_4 is positive, producing a negative step in v_{H_4} before the load insertion and a positive step after the load insertion. Furthermore, as predicted, if there is a voltage drop in the wires, the system has to produce more voltage in all v_{H_k}, being more time turned on. It means that the switching angles, θ_ks have to decrease and the cosine of the switching angles, $\mathbf{X}$, have to increase their values. Fig. 4.14 shows v_s of the experimental test, developed with the prototype, inserting the load of 200 W.
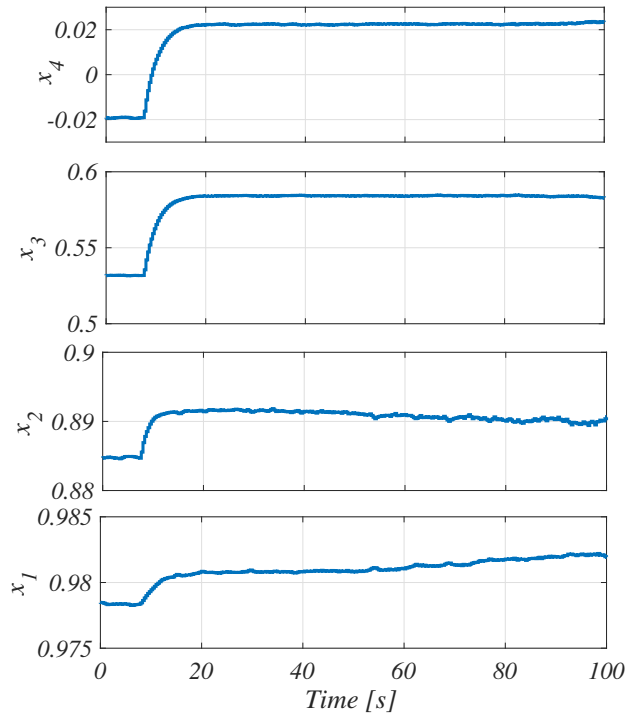
Figure 4.13: Simulation of the cosine of the switching angles, x_ks
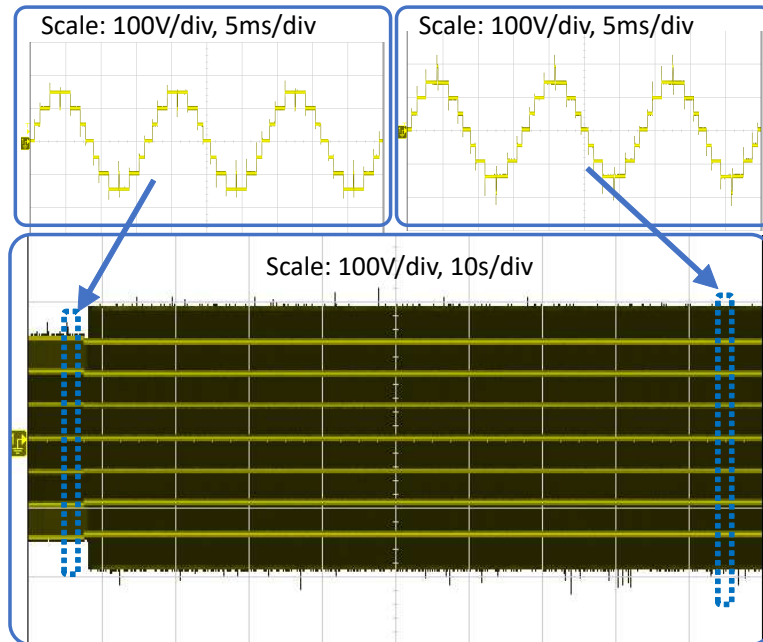
Figure 4.14: Experimental result of 200 W load insertion

Notice that the same waveform produced in the simulation is obtained in the experimental result, starting with a negative step in v_{H_4} and passing to a positive step when the load is inserted, to increase the voltage in v_s.

Fig. 4.15 shows the behavior of the harmonics of the experimental result. Notice that the fundamental component presents an undershoot similar to the simulation test with a faster transient response than the simulation test. Furthermore, Fig. 4.15 shows that the harmonics are also affected by the disturbances. However, all of them are stabilized after 50 seconds. Harmonic 3 presents a remaining oscillation between 0 and 0.15, which represents less than 0.1% of the fundamental component. This experimental test shows that the harmonics do not have similarity with the simulation test. Despite the behavior of the harmonics differs from the simulation, variations are always below 0.4 %
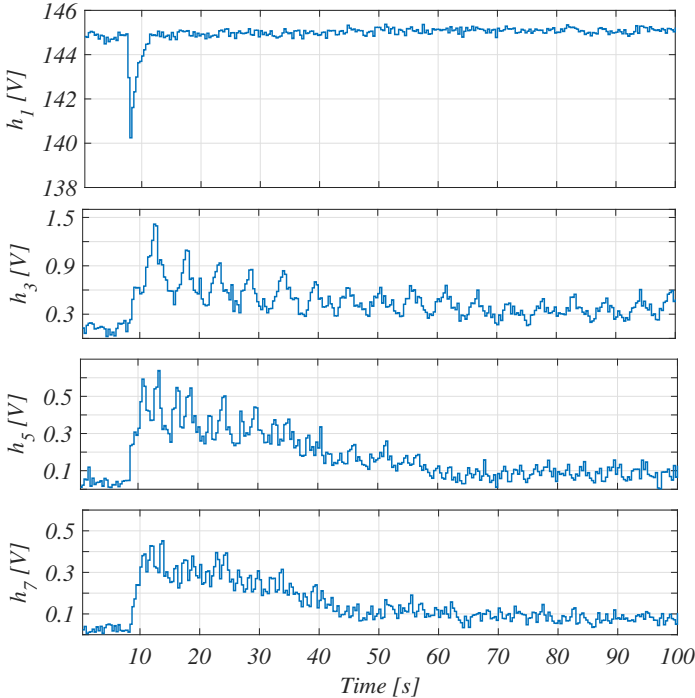
Figure 4.15: Harmonics behavior of the 200 W load experimental test

4.4.2   Changes in one source

The test describes the system connected to 200 W load with a change in v_{e1} from 55 V to 50 V at t=7.5 seconds. It is important to mention that v_{e1} is the source that supplies the majority of power because θ_1 is the smallest switching angle. Fig. 4.16 shows the waveform of v_s in this test. It can be seen that before the voltage change, the 4th FB presents a negative step, and after the disturbance, this FB produces a positive step.
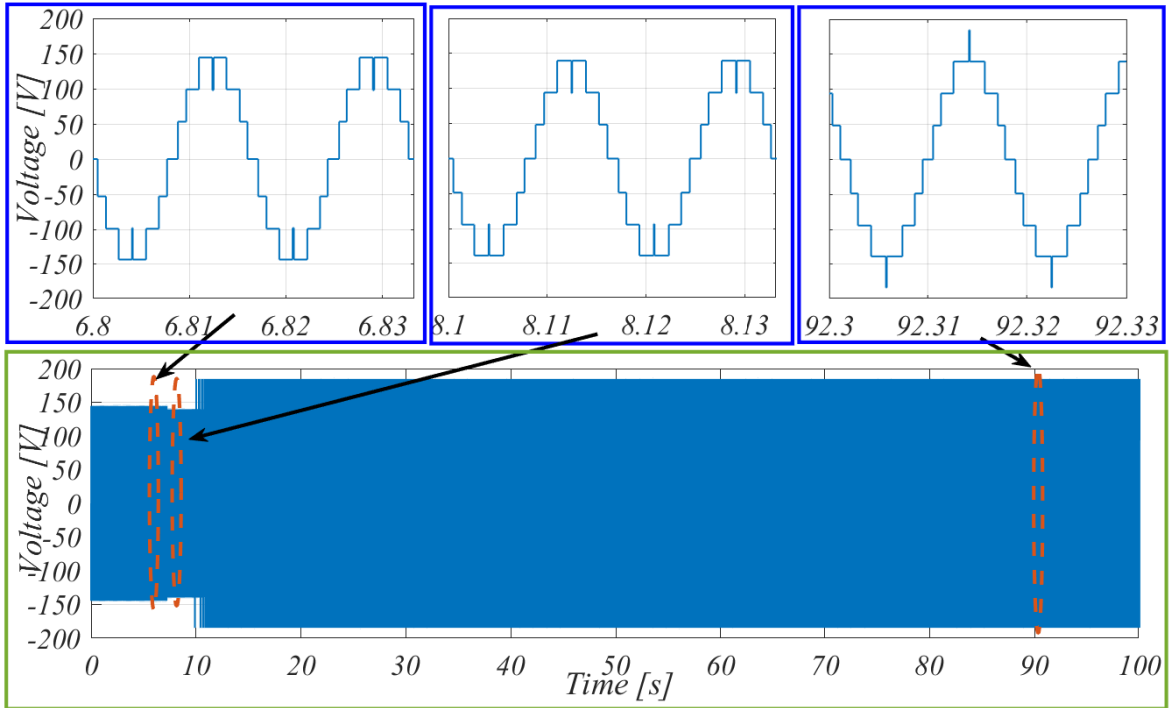
Figure 4.16: Simulation result of v_{e1} disturbance

For validating the result of this experiment, Fig. 4.17 shows the behavior of the harmonics. Notice that there are overshoots in h_1, h_3, h_5, representing the 4%, 1.1% and 0.4% of the reference of h_1, respectively, and h_7 is almost not affected. h_1 is stabilized after 12.5 seconds. In this test the harmonics present a very low oscillation that represents 0.34% of the fundamental component in the worst case, validating the robustness of the controller. Fig. 4.18 shows the action of $\mathbf{X}$ when one of the input voltages is disturbed. It can be seen that before the voltage disturbance, x_4 is negative, validating the negative step produced in v_{H_4} during the test. When the input voltage change, all the x_ks start to increase their values to increase the fundamental component of v_s, and x_4 passes from a negative to a positive value. Fig. 4.19 shows the experimental results of the output voltage v_s when the disturbance in v_{e1} is produced, and Fig. 4.20 shows the behavior of the harmonics of v_s.
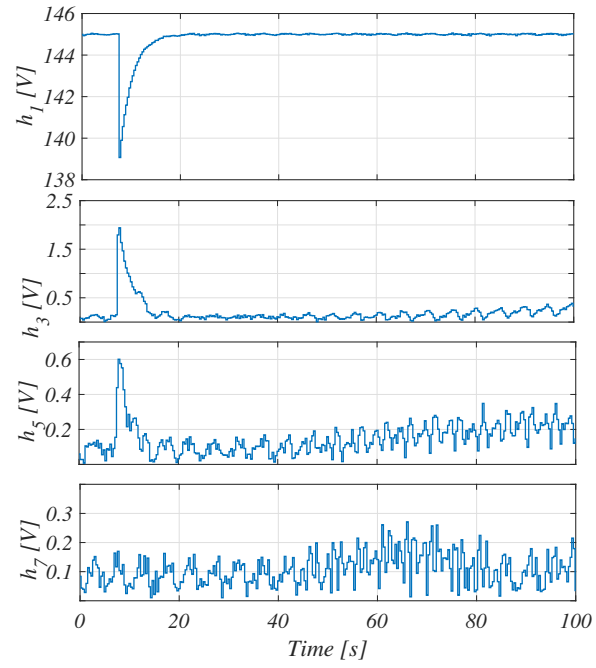
Figure 4.17: Simulation of the transient of the harmonics after a disturbance in the v_{e1}
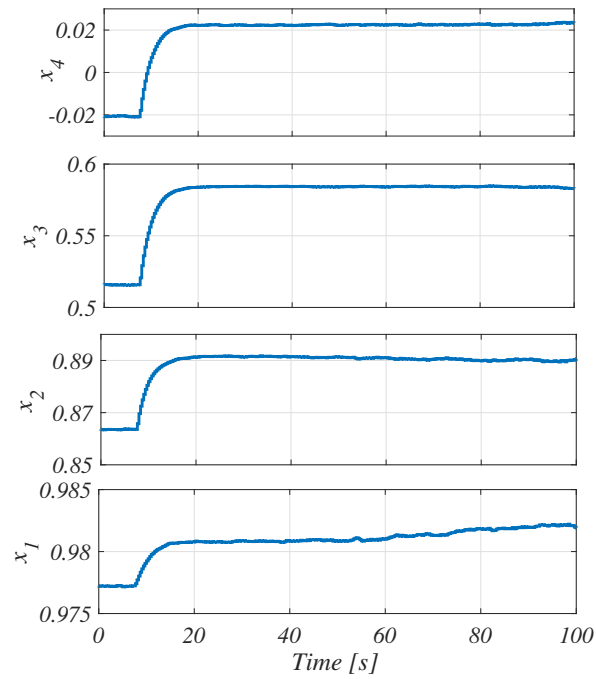
Figure 4.18: Simulation of the transient of $\mathbf{X}$ when a disturbance of v_{e1} is produced
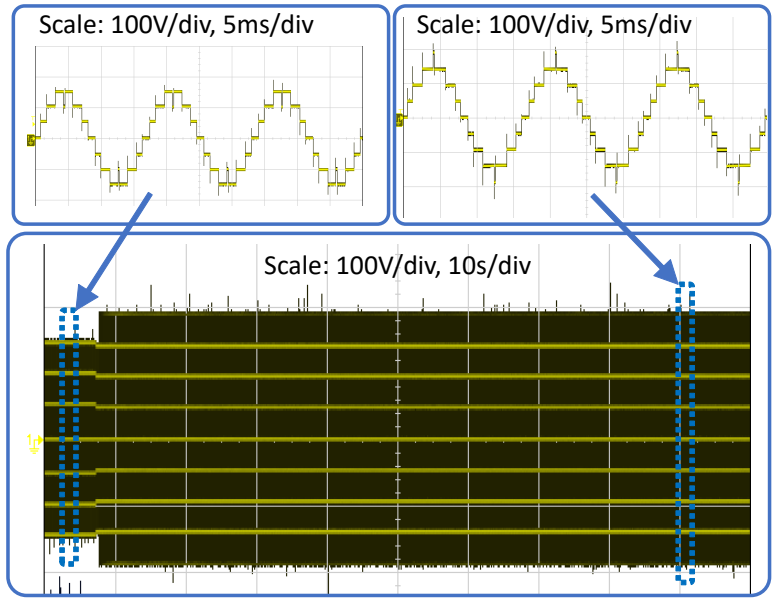
Figure 4.19: Experimental result of v_{e1} disturbance
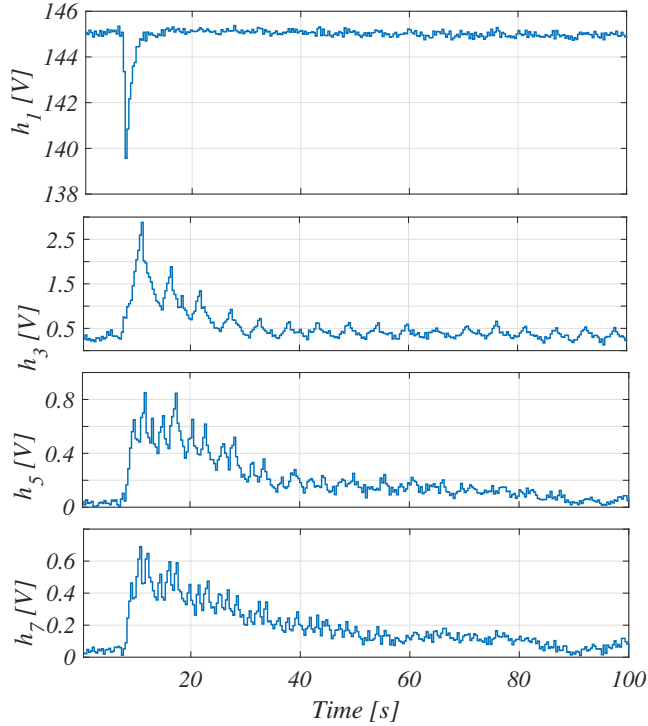
Figure 4.20: Harmonics behavior of v_{e1} disturbance experimental test

Notice that the experimental result presents a similarity to the simulation one, before and after the change of the input source, starting with a negative step in x_4, and changing to a positive value after the voltage change. Fig. 4.20 describes that h_1 has an undershoot and a settling time of 12 s approximately. Furthermore, all the harmonics present an overshoot, stabilizing the system after some seconds.

4.5   Conclusions of the chapter

The chapter presents a deep analysis of the behavior of the harmonics and the switching angles, using SHE and also a control law applied to SHE, is proposed, regulating the fundamental component and eliminating harmonics 3, 5 and 7.

Three analyses of the system are carried out. The first one corresponds to the behavior of the cosine of the switching angles vs the fundamental components, while the harmonics 3, 5 and 7 are 0, showing the regions which the system has or not a solution. Furthermore, this analysis shows that it is not important the number of FBs and only the number of switching cares. The second analyses correspond to the sensitivity of the harmonics vs the cosine of the switching angles, showing that some cosines of the angles have a quasi-linear relationship with the harmonics. This fact allows in the future to improve the algorithm to find the solution of the angles. The last analysis corresponds to the behavior of the harmonics when a disturbance in the input voltage is produced, concluding that there is a linear relationship between the input voltages and the harmonics.

The controller is composed of a PI controller and a virtual dynamical system. The original model corresponds to a trigonometric equation system which is converted to a polynomial equation system. Then, a transformation to its Groebner Basis is carried out, generating a decoupled equation system. Finally, an adaption of the Newton Raphson solving Method is applied for finding the roots of the polynomial system, converting the static polynomial equation system into a virtual dynamical one. Then the classical PI controller is implemented.

The experimental tests and simulations validate the good performance of this proposed controller. Those tests correspond to a 200 W load insertion and a disturbance in one of the input sources. Concerning the future works, the optimization of the algorithm to find the cosine of the switching angles is being studied.

Chapter 5

Conclusions

Multicellular converters offer a large number of advantages as the increment of the output frequency and the distribution of the power in the cells. Furthermore, these converters present the capability to manage high voltage and high power because they have a modular structure. Because of that, there are some challenges to improves some functions of these topologies such as the balancing of the cell variables, the management of several variables, fault tolerance ability and the improvement of efficiency. This research proposes two solutions to these challenges and it is divided into two cores.

The first core proposes a control method that has three functions: To balance a cell variable, to regulate a global variable and to implement a bypass system that allows to insert or remove cells during operation. This control method is designed for a wide range of multi-cellular converters that can be modeled as a proposed general model. This control is implemented in two different converters, the flying-capacitor multilevel converter, and the cascaded full bridge multilevel converter, obtaining good results in simulation and experimentation. For the cases of the flying-capacitor multilevel converter, the control method aims to balance the cell voltage and to regulate the output current. The theory of the controller applied to the flying capacitor multilevel converter indicates that the cell voltage and the output current are completely decoupled. This is validated in simulation and experimental tests, with a prototype developed in the LAPLACE lab, stepping the load, disturbing the input voltage and inserting a cell during operation, obtaining good performances in all the tests, balancing the cell voltage, regulating the output current in all the tests. For the case of the cascaded full-bridge multilevel converter, the proposed controller aims to balances the output voltage of the FBs and to regulate the output current. The theory for this topology indicates that the output current is decoupled from the output voltage of the FBs, while the output voltage of the FBs depends on the balancing stage and the GV regulator stage. The GV regulator fixes the trajectory of the cell variables while the balancing controller compensates for the differences between the cell variables. The control method is validated in a prototype, that was carried out in Javeriana University, working as a DC/DC and as a DC/AC converter, in simulation and experiments, stepping the load, disturbing the input voltages and inserting a FB during operation, having good responses in all the tests. Two future works are in mind with this control method. The first one is the implementation of this controller for balancing the state of charge of the batteries that are the input sources of a cascaded full bridge multilevel converter, and the second future work is the implementation of this control method in a multi-phase buck converter.

The second core of this research deals with an adaptive control method for a mul-

tilevel inverter using Selective Harmonic Elimination modulation. This modulation is a low frequency modulation technique that improves significantly the efficiency of the inverter. However, the complexity of math computation makes difficult to implement this technique online. This adaptive control is based on polynomials conversions and iterative methods that convert the static system into a virtual dynamical one, that also decouples the equation for finding the switching angles. Furthermore, the theory indicates that it is not important the number of FBs, caring only the number of switching angles. Additionally, this part of the research shows three analyses of this modulation technique, which helps to understand the behavior of the harmonics according to the switching angles. The theory is designed for a system of 4 switching angles, which can produce a maximum of 9 levels. However, it is possible to extrapolate this theory to more number of switching angles. The adaptive control method is validated in a cascaded full-bridge multilevel inverter of 9 levels, that was developed in Javeriana University, disturbing one of the input voltage and inserting a load, presenting good responses in all the tests. A future work of this stage of the research is the optimization of the algorithm to readjust the switching angles.

Appendix A
Fourier components of v_{ek}

Given the following waveform:
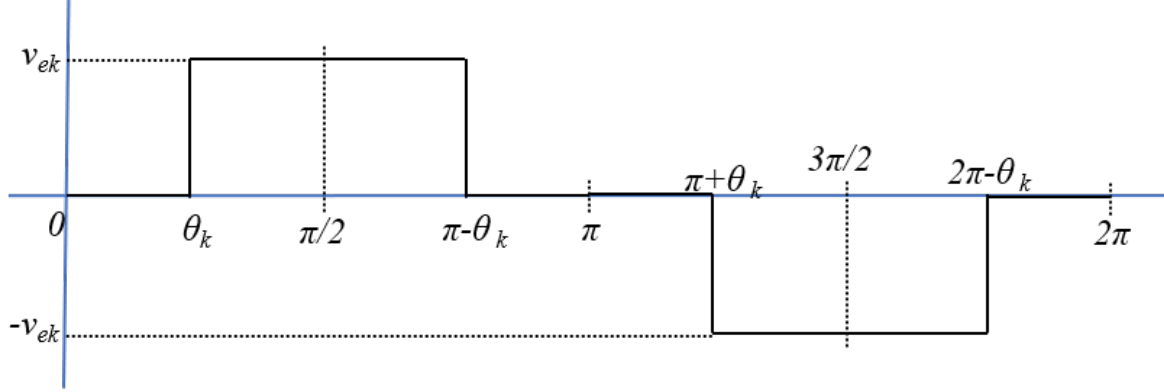
$$v_{Hk} = \begin{cases} v_{ek} & ; \theta_k < \omega t < \pi - \theta_k \\ -v_{ek} & ; \pi + \theta_k < \omega t < 2\pi - \theta_k \\ 0 & ; 0 < \omega t < \theta_k \lor \pi - \theta_k < \omega t < \pi + \theta_k \lor 2\pi - \theta_k < \omega t < 2\pi \end{cases} \tag{A.1}$$

Expressing as the Fourier coefficients

$$v_{Hk} = \sum_{m=1}^{\infty} a_{mk} \cos(m\omega t) + b_{mk} \sin(m\omega t) \tag{A.2}$$

where:

$$a_{mk} = \frac{2}{T} \int_0^T f(\omega t) \cos(m\omega t)$$
$$b_{mk} = \frac{2}{T} \int_0^T f(\omega t) \sin(m\omega t) \tag{A.3}$$

Hence:

$$a_{mk} = \frac{1}{\pi} \int_0^{2\pi} v_{Hk} \cos(m\omega t)$$
$$b_{mk} = \frac{1}{\pi} \int_0^{2\pi} v_{Hk} \sin(m\omega t) \tag{A.4}$$

Therefore a_{mk} is:

$$a_{mk} = \frac{1}{\pi} \left(\int_{\theta_k}^{\pi - \theta_k} v_{ek} \cos(m\omega t) - \int_{\pi + \theta_k}^{2\pi - \theta_k} v_{ek} \cos(m\omega t) \right)$$

$$a_{mk} = \frac{1}{\pi} \left(\frac{v_{ek}}{m} \sin(m\omega t) \Big|_{\theta_k}^{\pi - \theta_k} - \frac{v_{ek}}{m} \sin(m\omega t) \Big|_{\pi + \theta_k}^{2\pi - \theta_k} \right)$$

$$a_{mk} = \frac{v_{ek}}{m\pi} \left(\sin(m\pi - m\theta_k) - \sin(m\theta_k) - \sin(2m\pi - m\theta_k) \right.$$
$$\left. + \sin(m\pi + m\theta_k) \right)$$

$$a_{mk} = \frac{v_{ek}}{m\pi} \left(\underline{\sin(m\pi)}^{\;0} \cos(m\theta_k) - \cos(m\pi) \underline{\sin(m\theta_k)} - \underline{\sin(m\theta_k)} \right.$$
$$- \underline{\sin(2m\pi)}^{\;0} \cos(m\theta_k) + \underline{\cos(2m\pi)}^{\;1} \underline{\sin(m\theta_k)} + \underline{\sin(m\pi)}^{\;0} \cos(m\theta_k)$$
$$\left. + \underline{\cos(m\pi) \sin(m\theta_k)} \right)$$

$$\boxed{a_{mk} = 0}$$

Analogously, b_{mk} is:

$$b_{mk} = \frac{1}{\pi} \left(\int_{\theta_k}^{\pi - \theta_k} v_{ek} \sin(m\omega t) - \int_{\pi + \theta_k}^{2\pi - \theta_k} v_{ek} \sin(m\omega t) \right)$$

$$b_{mk} = \frac{1}{\pi} \left(- \frac{v_{ek}}{m} \cos(m\omega t) \Big|_{\theta_k}^{\pi - \theta_k} + \frac{v_{ek}}{m} \cos(m\omega t) \Big|_{\pi + \theta_k}^{2\pi - \theta_k} \right)$$

$$a_{mk} = \frac{v_{ek}}{m\pi} \left(- \cos(m\pi - m\theta_k) + \cos(m\theta_k) + \cos(2m\pi - m\theta_k) \right.$$
$$\left. - \cos(m\pi + m\theta_k) \right)$$

$$b_{mk} = \frac{v_{ek}}{m\pi} \left(- \cos(m\pi)\cos(m\theta_k) - \underline{\sin(m\pi)}^{\;0} \sin(m\theta_k) + \cos(m\theta_k) \right.$$
$$+ \underline{\cos(2m\pi)}^{\;1} \cos(m\theta_k) + \underline{\sin(2m\pi)}^{\;0} \sin(m\theta_k) - \cos(m\pi)\cos(m\theta_k)$$
$$\left. + \underline{\sin(m\pi)}^{\;0} \sin(m\theta_k) \right)$$

$$b_{mk} = \frac{v_{ek}}{m\pi} \left(-2\cos(m\pi)\cos(m\theta_k) + 2\cos(m\theta_k) \right)$$

$$b_{mk} = \frac{2v_{ek}}{m\pi} (1 - \cos(m\pi)) \cos(m\theta_k)$$

$$\cos(m\pi) = \begin{cases} 1 & ; m = even \\ -1 & ; m = odd \end{cases}$$

$$\boxed{b_{mk} = \begin{cases} 0 & ; m = even \\ \dfrac{2v_{ek}}{m\pi} \cos(m\theta_k) & ; m = odd \end{cases}}$$

Appendix B

Proof that a product of a graph and a linear combination of a graph and the identity matrix is also a graph

Lets define $\mathbb{I}$ as the identity matrix of $n \times n$, and $\mathbf{A}$ and $\mathbf{B}$, two matrices that represents the laplacian of a Graph

$$\mathbf{A} = \begin{bmatrix} a_{11} & a_{12} & \cdots & a_{1n} \\ a_{21} & a_{22} & \ddots & a_{2n} \\ \vdots & \ddots & \ddots & \vdots \\ a_{n1} & a_{2n} & \cdots & a_{nn} \end{bmatrix} \quad \mathbf{B} = \begin{bmatrix} b_{11} & b_{12} & \cdots & b_{1n} \\ b_{21} & b_{22} & \ddots & b_{2n} \\ \vdots & \ddots & \ddots & \vdots \\ b_{n1} & b_{2n} & \cdots & b_{nn} \end{bmatrix}$$

Hence, if $\mathbf{A}$ and $\mathbf{B}$ are laplacian of a graph, $\mathbf{C} = \mathbf{A}\left(\text{ff}\mathbb{I} + \text{fl}\mathbf{B}\right)$ is also a laplacian of a graph.

If $\mathbf{A}$ and $\mathbf{B}$ are laplacians of a graph, the sum of the elements of its columns and its rows are zero, hence:

$$\sum_{i=1}^{n} a_{ij} = 0 \quad ; \sum_{j=1}^{n} a_{ij} = 0$$
$$\sum_{i=1}^{n} b_{ij} = 0 \quad ; \sum_{j=1}^{n} b_{ij} = 0$$

Expressing as a matrix form it follows:

$$\mathbf{AV_1} = \mathbf{0} \quad ; \mathbf{V_1^T A} = \mathbf{0^T}$$
$$\mathbf{BV_1} = \mathbf{0} \quad ; \mathbf{B_1^T A} = \mathbf{0^T}$$

where $\mathbf{V_1} = \begin{bmatrix} 1 & 1 & \cdots & 1 \end{bmatrix}^T$, $\mathbf{0} = \begin{bmatrix} 0 & 0 & \cdots & 0 \end{bmatrix}^T$ Therefore the sum of the elements of the rows and the sum of the elements of the columns of of $\mathbf{C}$ can be represented as $\mathbf{CV_1}$ and $\mathbf{V_1^T C}$, respectively. Hence,

$$\mathbf{CV_1} = \mathbf{A}\left(\alpha\mathbb{I} + \gamma\mathbf{B}\right)\mathbf{V_1}$$
$$= \alpha\mathbf{AV_1} + \gamma\mathbf{ABV_1}$$
$$= \alpha\mathbf{AV_1}^{\nearrow\mathbf{0}} + \gamma\mathbf{A(BV_1)}^{\nearrow\mathbf{0}}$$

$$\boxed{\mathbf{CV_1} = \mathbf{0}}$$

and

$$\mathbf{V_1^T C} = \mathbf{V_1^T A} \left(\alpha \mathbb{I} + \gamma \mathbf{B} \right)$$
$$= \alpha \mathbf{V_1^T A} + \gamma \mathbf{V_1^T A B}$$
$$= \alpha \underbrace{\mathbf{V_1^T A}}_{\mathbf{0^T}} + \gamma \left(\mathbf{B^T} \underbrace{\left(\mathbf{A V_1^T} \right)}_{\mathbf{0^T}} \right)$$

$$\boxed{\mathbf{V_1^T C} = \mathbf{0^T}}$$

Appendix C

Proof of stability of the control law in the Flying-Capacitor Multilevel Converter with the nonlinear model

According to 3.13, the nonlinear model is:

$$
\begin{bmatrix} \dot{\mathbf{V}} \\ \dot{i_o} \end{bmatrix} = \begin{bmatrix} \dfrac{i_o}{C_o}\mathbf{A_T D} + \mathbf{E}\dot{v}_e \\ \dfrac{1}{L_o}\mathbf{D}^T\mathbf{V} - \dfrac{R_o}{L_o}i_o \end{bmatrix}
$$

Defining the new variables as $e = i_o - I_{ref}$, $z = \int e\,dt$, and $\mathbf{Q} = \int \mathbf{V}\,dt$. Hence, the new system is:

$$
\begin{bmatrix} \dot{\mathbf{V}} \\ \dot{\mathbf{Q}} \\ \dot{e} \\ \dot{z} \end{bmatrix} = \begin{bmatrix} \frac{e+I_{ref}}{C_o}\mathbf{A_T D} + \mathbf{E}\dot{v}_e \\ \mathbf{V} \\ \frac{1}{L_o}\mathbf{D}^T\mathbf{V} - \frac{R_o}{L_o}\left(e + I_{ref}\right) \\ e \end{bmatrix}
$$

The control law expressed in time domain is:

$$
\mathbf{D} = k_{pV}\mathbf{D_{iff}V} + k_{iV}\mathbf{D_{iff}Q} - k_{pi}e\mathbf{V_1} - k_{ii}z\mathbf{V_1}
$$

Inserting the control law expressed in time domain into the nonlinear model, remaining that $\mathbf{D_{iff}V_1} = 0$ and $\mathbf{V_T V_1} = v_e$, is:

$$
\begin{bmatrix} \dot{\mathbf{V}} \\ \dot{\mathbf{Q}} \\ \dot{e} \\ \dot{z} \end{bmatrix} = \begin{bmatrix} \frac{k_{pV}\left(e+I_{ref}\right)}{C_o}\mathbf{A_T D_{iff}V} + \frac{k_{iV}\left(e+I_{ref}\right)}{C_o}\mathbf{A_T D_{iff}Q} + \mathbf{E}\dot{v}_e \\ \mathbf{V} \\ \frac{k_{pV}}{L_o}\mathbf{V^T D_{iff}V} + \frac{k_{iV}}{L_o}\mathbf{V^T D_{iff}Q} - k_{pi}v_e e - k_{ii}v_e z - \frac{R_o}{L_o}\left(e + I_{ref}\right) \\ e \end{bmatrix}
$$

Let's defining a Lyapunov function:

$$
L = \frac{1}{2}\left(\alpha_1\mathbf{V^T V} + \mathbf{Q^T P_2 Q} + e^2 + f(z)\right) > 0
$$

where, $f(z) > 0, z \neq = 0$, $\alpha_1 > 0$ and P_2 is positive semi definitive and $f(0) = 0$. Hence;

assuming that v_e is constant and grater than 0:

$$\dot{L} = \alpha_1 \mathbf{V^T \dot{V}} + \mathbf{Q^T P_2 \dot{Q}} + e\dot{e} + \frac{\partial f}{\partial z}\dot{z} < 0$$

$$\dot{L} = \frac{k_{pV}\alpha_1\left(e+I_{ref}\right)}{C_o}\mathbf{V^T A_T D_{iff} V} + \frac{k_{iV}\alpha_1\left(e+I_{ref}\right)}{C_o}\mathbf{V^T A_T D_{iff} Q} + \mathbf{Q^T P_2 V} + \frac{k_{pV}e}{L_o}\mathbf{V^T D_{iff} V}$$

$$+ \frac{k_{iV}e}{L_o}\mathbf{V^T D_{iff} Q} - k_{pi}v_e e^2 - k_{ii}v_e ez - \frac{R_o}{L_o}e\left(e + I_{ref}\right) + \frac{\partial f}{\partial z}e < 0$$

$$k_{pV}\mathbf{V^T}\underbrace{\left(\frac{\alpha_1\left(e+I_{ref}\right)}{C_o}\mathbf{A_T} + \frac{e}{L_o}\mathbb{I}\right)}_{\mathbf{M}}\mathbf{D_{iff} V} + \mathbf{V^T}\left(k_{iV}\underbrace{\left(\frac{\alpha_1\left(e+I_{ref}\right)}{C_o}\mathbf{A_T} + \frac{e}{L_o}\mathbb{I}\right)}_{\mathbf{M}}\mathbf{D_{iff}} + \mathbf{P_2^T}\right)\mathbf{Q} < 0(1)$$

$$- k_{pi}v_e e^2 - k_{ii}v_e ez - \frac{R_o}{L_o}e^2 - \frac{R_o}{L_o}eI_{ref} + \frac{\partial f}{\partial z}e < 0(2)$$

For (1), knowing that $\mathbf{A_T}$ is semi definite because one eigenvalue is $=0$ and the others are less than 0, and $\mathbf{D_{iff}}$ is positive semi definite because one eigenvalue is 0 and the others are greater than 0:

$$s = \left(\frac{\alpha_1\left(e+I_{ref}\right)}{C_o}\lambda + \frac{e}{L_o}\right) < 0$$

where s are the eigenvalues of $\mathbf{M}$ and λ are the eigenvalues of $\mathbf{A_T}$. Hence, it must be an α_1 that

$$\alpha_1 < -\frac{eC_o}{L_o\lambda\left(e + I_{ref}\right)}$$

Taking into account that $\lambda < 0$ because $\mathbf{A_T}$ is negative semi definite, $\alpha_1 > 0$, that is in concordance with the first statement. Hence:

$$0 < \alpha_1 < -\frac{eC_o}{L_o\lambda\left(e + I_{ref}\right)}$$

and

$$\mathbf{P_2} = -k_{iV}\mathbf{D_{iff}M^T}$$

Due to $\mathbf{M}$ is negative semi definite and $\mathbf{D_{iff}}$ is positive semi definite, $\mathbf{P_2}$ is positive semi definite.

For (2)

$$e\left(-k_{ii}v_e z - \frac{R_o}{L_o}I_{ref} + \frac{\partial f}{\partial z}\right) < 0$$

$$e > 0 \quad \wedge \quad \left(-k_{ii}v_e z - \frac{R_o}{L_o}I_{ref} + \frac{\partial f}{\partial z}\right) < 0$$

$$e < 0 \quad \wedge \quad \left(-k_{ii}v_e z - \frac{R_o}{L_o}I_{ref} + \frac{\partial f}{\partial z}\right) > 0$$

Solving the differential inequality

$$e > 0 \quad \wedge \quad f < k_{ii}v_e z^2 + 2\frac{R_o}{L_o}I_{ref}z$$

$$e < 0 \quad \wedge \quad f > k_{ii}v_e z^2 + 2\frac{R_o}{L_o}I_{ref}z$$

Hence, if f, α_1 and P_2 have the proposed form, a Lyapunov function that satisfies stability for this system is obtained

Appendix D

Groebner basis conversion of $\mathbf{\Pi(X)V_1}$

$p_1(x_1, \mathbf{H_e}) = (26880\pi^4 {h'_{e1}}^6 - 1612800\pi^2 {h'_{e1}}^4 - 1612800\pi^2 {h'_{e1}}^3 h'_{e3} + 19353600 {h'_{e1}}^2$

$+ 19353600 h'_{e1} h'_{e3} + 19353600 h'_{e1} h'_{e5} - 19353600 {h'_{e3}}^2) \mathbf{x_1^4} + (-6720\pi^5 {h'_{e1}}^7 + 403200\pi^3 {h'_{e1}}^5$

$+ 403200\pi^3 {h'_{e1}}^4 h'_{e3} - 4838400\pi {h'_{e1}}^3 - 4838400\pi {h'_{e1}}^2 h'_{e3} - 4838400\pi {h'_{e1}}^2 h'_{e5}$

$+ 4838400\pi h'_{e1} {h'_{e3}}^2) \mathbf{x_1^3} + (720\pi^6 {h'_{e1}}^8 - 60480\pi^4 {h'_{e1}}^6 - 60480\pi^4 {h'_{e1}}^5 h'_{e3} + 1612800\pi^2 {h'_{e1}}^4$

$+ 2419200\pi^2 {h'_{e1}}^3 h'_{e3} + 806400\pi^2 {h'_{e1}}^3 h'_{e5} - 14515200 {h'_{e1}}^2 - 19353600 h'_{e1} h'_{e3} - 19353600 h'_{e1} h'_{e5}$

$- 4838400 h'_{e1} h'_{e7} + 14515200 {h'_{e3}}^2 + 4838400 h'_{e3} h'_{e5}) \mathbf{x_1^2} + (-40\pi^7 {h'_{e1}}^9 + 5040\pi^5 {h'_{e1}}^7$

$+ 5040\pi^5 {h'_{e1}}^6 h'_{e3} - 201600\pi^3 {h'_{e1}}^5 - 302400\pi^3 {h'_{e1}}^4 h'_{e3} - 100800\pi^3 {h'_{e1}}^4 h'_{e5} + 2419200\pi {h'_{e1}}^3$

$+ 2419200\pi {h'_{e1}}^2 h'_{e3} + 3628800\pi {h'_{e1}}^2 h'_{e5} + 1209600\pi {h'_{e1}}^2 h'_{e7} - 3628800\pi h'_{e1} {h'_{e3}}^2$

$- 2419200\pi h'_{e1} h'_{e3} h'_{e5} + 1209600\pi {h'_{e3}}^3) \mathbf{x_1} + \pi^8 {h'_{e1}}^{10} - 180\pi^6 {h'_{e1}}^8 - 180\pi^6 {h'_{e1}}^7 h'_{e3} + 10080\pi^4 {h'_{e1}}^6$

$+ 15120\pi^4 {h'_{e1}}^5 h'_{e3} + 5040\pi^4 {h'_{e1}}^5 h'_{e5} - 201600\pi^2 {h'_{e1}}^4 - 302400\pi^2 {h'_{e1}}^3 h'_{e3} - 201600\pi^2 {h'_{e1}}^3 h'_{e5}$

$- 100800\pi^2 {h'_{e1}}^3 h'_{e7} + 302400\pi^2 {h'_{e1}}^2 h'_{e3} h'_{e5} - 302400\pi^2 h'_{e1} {h'_{e3}}^3 + 1209600 {h'_{e1}}^2 + 2419200 h'_{e1} h'_{e3}$

$+ 1209600 h'_{e1} h'_{e5} + 1209600 h'_{e7} h'_{e1} - 1209600 h'_{e3} h'_{e5} + 1209600 h'_{e3} h'_{e7} - 1209600 {h'_{e5}}^2 = 0$

$p_2(x_1, x_2, \mathbf{H_e}) = (672\pi^4 {h'_{e1}}^6 - 40320\pi^2 {h'_{e1}}^4 - 40320\pi^2 {h'_{e1}}^3 h'_{e3} + 483840 {h'_{e1}}^2 + 483840 h'_{e1} h'_{e3}$

$+ 483840 h'_{e1} h'_{e5} - 483840 {h'_{e3}}^2) \mathbf{x_2^3} + (672\pi^4 {h'_{e1}}^6 - 40320\pi^2 {h'_{e1}}^4 - 40320\pi^2 {h'_{e1}}^3 h'_{e3}$

$+ 483840 {h'_{e1}}^2 + 483840 h'_{e1} h'_{e3} + 483840 h'_{e1} h'_{e5} - 483840 {h'_{e3}}^2) \mathbf{x_2^2 x_1} + (-168\pi^5 {h'_{e1}}^7$

$+ 10080\pi^3 {h'_{e1}}^5 + 10080\pi^3 {h'_{e1}}^4 h'_{e3} - 120960\pi {h'_{e1}}^3 - 120960\pi {h'_{e1}}^2 h'_{e3} - 120960\pi {h'_{e1}}^2 h'_{e5}$

$+ 120960\pi h'_{e1} {h'_{e3}}^2) \mathbf{x_2^2} + (672\pi^4 {h'_{e1}}^6 - 40320\pi^2 {h'_{e1}}^4 - 40320\pi^2 {h'_{e1}}^3 h'_{e3} + 483840 {h'_{e1}}^2$

$+ 483840 h'_{e1} h'_{e3} + 483840 h'_{e1} h'_{e5} - 483840 {h'_{e3}}^2) \mathbf{x_1^2 x_2} + (-168\pi^5 {h'_{e1}}^7 + 10080\pi^3 {h'_{e1}}^5$

$+ 10080\pi^3 {h'_{e1}}^4 h'_{e3} - 120960\pi {h'_{e1}}^3 - 120960\pi {h'_{e1}}^2 h'_{e3} - 120960\pi {h'_{e1}}^2 h'_{e5} + 120960\pi h'_{e1} {h'_{e3}}^2) \mathbf{x_2 x_1}$

$+ (18\pi^6 {h'_{e1}}^8 - 1512\pi^4 {h'_{e1}}^6 - 1512\pi^4 {h'_{e1}}^5 h'_{e3} + 40320\pi^2 {h'_{e1}}^4 + 60480\pi^2 {h'_{e1}}^3 h'_{e3} + 20160\pi^2 {h'_{e1}}^3 h'_{e5}$

$- 362880 {h'_{e1}}^2 - 483840 h'_{e1} h'_{e3} - 483840 h'_{e1} h'_{e5} - 120960 h'_{e1} h'_{e7} + 362880 {h'_{e3}}^2 + 120960 h'_{e3} h'_{e5}) \mathbf{x_2}$

$+ (672\pi^4 {h'_{e1}}^6 - 40320\pi^2 {h'_{e1}}^4 - 40320\pi^2 {h'_{e1}}^3 h'_{e3} + 483840 {h'_{e1}}^2 + 483840 h'_{e1} h'_{e3} + 483840 h'_{e1} h'_{e5}$

$- 483840 {h'_{e3}}^2) \mathbf{x_1^3} + (-168\pi^5 {h'_{e1}}^7 + 10080\pi^3 {h'_{e1}}^5 + 10080\pi^3 {h'_{e1}}^4 h'_{e3} - 120960\pi {h'_{e1}}^3$

$- 120960\pi {h'_{e1}}^2 h'_{e3} - 120960\pi {h'_{e1}}^2 h'_{e5} + 120960\pi h'_{e1} {h'_{e3}}^2) \mathbf{x_1^2} + (18\pi^6 {h'_{e1}}^8 - 1512\pi^4 {h'_{e1}}^6$

$- 1512\pi^4 {h'_{e1}}^5 h'_{e3} + 40320\pi^2 {h'_{e1}}^4 + 60480\pi^2 {h'_{e1}}^3 h'_{e3} + 20160\pi^2 {h'_{e1}}^3 h'_{e5} - 362880 {h'_{e1}}^2$

$$- 483840h'_{e1}h'_{e3} - 483840h'_{e1}h'_{e5} - 120960h'_{e1}h'_{e7} + 362880h'^{2}_{e3} + 120960h'_{e3}h'_{e5})\mathbf{x_1} - \pi^7 h'^{9}_{e1}$$

$$+ 126\pi^5 h'^{7}_{e1} + 126\pi^5 h'^{6}_{e1}h'_{e3} - 5040\pi^3 h'^{5}_{e1} - 7560\pi^3 h'^{4}_{e1}h'_{e3} - 2520\pi^3 h'^{4}_{e1}h'_{e5} + 60480\pi h'^{3}_{e1}$$

$$+ 60480\pi h'^{2}_{e1}h'_{e3} + 90720\pi h'^{2}_{e1}h'_{e5} + 30240\pi h'^{2}_{e1}h'_{e7} - 90720\pi h'_{e1}h'^{2}_{e3} - 60480\pi h'_{e1}h'_{e3}h'_{e5}$$

$$+ 30240\pi h'^{3}_{e3} = 0$$

$$p_3(x_1, x_2, x_2, \mathbf{H_e}) = (112\pi^4 h'^{6}_1 - 6720\pi^2 h'^{4}_1 - 6720\pi^2 h'^{3}_1 h'_3 + 80640h'^{2}_1 + 80640h'_1 h'_3$$

$$+ 80640h'_1 h'_5 - 80640h'^{2}_3)\mathbf{x_3^2} + (112\pi^4 h'^{6}_1 - 6720\pi^2 h'^{4}_1 - 6720\pi^2 h'^{3}_1 h'_3 + 80640h'^{2}_1$$

$$+ 80640h'_1 h'_3 + 80640h'_1 h'_5 - 80640h'^{2}_3)\mathbf{x_3 x_2} + (112\pi^4 h'^{6}_1 - 6720\pi^2 h'^{4}_1 - 6720\pi^2 h'^{3}_1 h'_3$$

$$+ 80640h'^{2}_1 + 80640h'_1 h'_3 + 80640h'_1 h'_5 - 80640h'^{2}_3)\mathbf{x_3 x_1} + (-28\pi^5 h'^{7}_1 + 1680\pi^3 h'^{5}_1$$

$$+ 1680\pi^3 h'^{4}_1 h'_3 - 20160\pi h'^{3}_1 - 20160\pi h'^{2}_1 h'_3 - 20160\pi h'^{2}_1 h'_5 + 20160\pi h'_1 h'^{2}_3)x_2$$

$$+ (112\pi^4 h'^{6}_1 - 6720\pi^2 h'^{4}_1 - 6720\pi^2 h'^{3}_1 h'_3 + 80640h'^{2}_1 + 80640h'_1 h'_3 + 80640h'_1 h'_5$$

$$- 80640h'^{2}_3)\mathbf{x_2^2} + (112\pi^4 h'^{6}_1 - 6720\pi^2 h'^{4}_1 - 6720\pi^2 h'^{3}_1 h'_3 + 80640h'^{2}_1 + 80640h'_1 h'_3$$

$$+ 80640h'_1 h'_5 - 80640h'^{2}_3)\mathbf{x_2 x_1} + (-28\pi^5 h'^{7}_1 + 1680\pi^3 h'^{5}_1 + 1680\pi^3 h'^{4}_1 h'_3$$

$$- 20160\pi h'^{3}_1 - 20160\pi h'^{2}_1 h'_3 - 20160\pi h'^{2}_1 h'_5 + 20160\pi h'_1 h'^{2}_3)\mathbf{x_2} + (112\pi^4 h'^{6}_1 - 6720\pi^2 h'^{4}_1$$

$$- 6720\pi^2 h'^{3}_1 h'_3 + 80640h'^{2}_1 + 80640h'_1 h'_3 + 80640h'_1 h'_5 - 80640h'^{2}_3)\mathbf{x_1^2} + (-28\pi^5 h'^{7}_1$$

$$+ 1680\pi^3 h'^{5}_1 + 1680\pi^3 h'^{4}_1 h'_3 - 20160\pi h'^{3}_1 - 20160\pi h'^{2}_1 h'_3 - 20160\pi h'^{2}_1 h'_5$$

$$+ 20160\pi h'_1 h'^{2}_3)\mathbf{x_1} + 3\pi^6 h'^{8}_1 - 252\pi^4 h'^{6}_1 - 252\pi^4 h'^{5}_1 h'_3 + 6720\pi^2 h'^{4}_1 + 10080\pi^2 h'^{3}_1 h'_3$$

$$+ 3360\pi^2 h'^{3}_1 h'_5 - 60480h'^{2}_1 - 80640h'_1 h'_3 - 80640h'_1 h'_5 - 20160h'_7 h'_1 + 60480h'^{2}_3$$

$$+ 20160h'_3 h'_5 = 0$$

$$p_4(x_1, x_2 x_3, x_4, \mathbf{H_e}) = 4\mathbf{x_1} + 4\mathbf{x_2} + 4\mathbf{x_3} + 4\mathbf{x_4} - \pi h'_1 = 0$$

Bibliography

[1] N. Mohan, T. Undeland, and W. P. Robbins, "Power electronics: Converters, applications and design," 1989.

[2] M. H. Rashid, *Power electronics: devices, circuits and applications*. Pearson, 2014.

[3] M. Vivert, M. Cousineau, P. Ladoux, and J. Fabre, "Decentralized controller for the cell-voltage balancing of a multilevel flying cap converter," in *PCIM Europe 2019; International Exhibition and Conference for Power Electronics, Intelligent Motion, Renewable Energy and Energy Management*, May 2019, pp. 1–8.

[4] J. Fabre, P. Ladoux, E. Solano, G. Gateau, and J. Blaquière, "Full sic multilevel chopper for three-wire supply systems in dc electric railways," in *2016 International Conference on Electrical Systems for Aircraft, Railway, Ship Propulsion and Road Vehicles International Transportation Electrification Conference (ESARS-ITEC)*, Nov 2016, pp. 1–7.

[5] ——, "Mvdc three-wire supply systems for electric railways: Design and test of a full sic multilevel chopper," *IEEE Transactions on Industry Applications*, vol. 53, no. 6, pp. 5820–5830, Nov 2017.

[6] J. Fabre and P. Ladoux, "Parallel connection of 1200-v/100-a sic-mosfet half-bridge modules," *IEEE Transactions on Industry Applications*, vol. 52, no. 2, pp. 1669–1676, March 2016.

[7] B. Xu, H. Tu, Y. Du, H. Yu, H. Liang, and S. Lukic, "A distributed control architecture for cascaded h-bridge converter," in *2019 IEEE Applied Power Electronics Conference and Exposition (APEC)*, March 2019, pp. 3032–3038.

[8] R. D. D. B. M. Vivert, D. Patino and M. Cousineau, "Decentralized controller for a grid tied cascade multilevel invert," in *IEEE 3rd Colombian Conference on Automatic Control (CCAC)*, 2019.

[9] P. K. Achanta, D. Maksimovic, and M. Ilic, "Decentralized control of series stacked bidirectional dc-ac modules," in *2018 IEEE Applied Power Electronics Conference and Exposition (APEC)*, March 2018, pp. 1008–1013.

[10] J. He, Y. Li, B. Liang, and C. Wang, "Inverse power factor droop control for decentralized power sharing in series-connected-microconverters-based islanding microgrids," *IEEE Transactions on Industrial Electronics*, vol. 64, no. 9, pp. 7444–7454, Sep. 2017.

[11] M. Le Bolloch, M. Cousineai, and T. Meynard, "New masterless modular current-sharing technique for dc/dc parallel converters," in *Proceedings of 14th International Power Electronics and Motion Control Conference EPE-PEMC 2010*, Sep. 2010, pp. T3–73–T3–80.

[12] Y. Liu, H. Hong, and A. Q. Huang, "Real-time algorithm for minimizing thd in multilevel inverters with unequal or varying voltage steps under staircase modulation," *IEEE Transactions on Industrial Electronics*, vol. 56, no. 6, pp. 2249–2258, June 2009.

[13] M. Srndovic, A. Zhetessov, T. Alizadeh, Y. L. Familiant, G. Grandi, and A. Ruderman, "Simultaneous selective harmonic elimination and thd minimization for a single-phase multilevel inverter with staircase modulation," *IEEE Transactions on Industry Applications*, vol. 54, no. 2, pp. 1532–1541, March 2018.

[14] A. Kavousi, B. Vahidi, R. Salehi, M. K. Bakhshizadeh, N. Farokhnia, and S. H. Fathi, "Application of the bee algorithm for selective harmonic elimination strategy in multilevel inverters," *IEEE Transactions on Power Electronics*, vol. 27, no. 4, pp. 1689–1696, April 2012.

[15] K. Yang, Q. Zhang, R. Yuan, W. Yu, J. Yuan, and J. Wang, "Selective harmonic elimination with groebner bases and symmetric polynomials," *IEEE Transactions on Power Electronics*, vol. 31, no. 4, pp. 2742–2752, April 2016.

[16] M. Cousineau and B. Cougo, "Interleaved converter with massive parallelization of high frequency gan switching-cells using decentralized modular analog controller," in *2015 IEEE Energy Conversion Congress and Exposition (ECCE)*, Sep. 2015, pp. 4343–4350.

[17] T. A. Meynard and H. Foch, "Multi-level conversion: high voltage choppers and voltage-source inverters," in *PESC '92 Record. 23rd Annual IEEE Power Electronics Specialists Conference*, June 1992, pp. 397–403 vol.1.

[18] T. A. Meynard, M. Fadel, and N. Aouda, "Modeling of multilevel converters," *IEEE Transactions on Industrial Electronics*, vol. 44, no. 3, pp. 356–364, June 1997.

[19] M. F. Negash and U. B. Manthati, "Development of 7-level cascaded H-bridge inverter topology for PV applications," in *International Conference on Electrical, Electronics, and Optimization Techniques, ICEEOT 2016*. Chennai, Tamil Nadu, India: IEEE, 2016, pp. 1847–1852.

[20] Q. Huang and A. Q. Huang, "Feedforward proportional carrier-based pwm for cascaded h-bridge pv inverter," *IEEE Journal of Emerging and Selected Topics in Power Electronics*, vol. 6, no. 4, pp. 2192–2205, Dec 2018.

[21] R. D. G. P. Diego Bernal Cobaleda, Miguel Vivert, "Low-voltage cascade multilevel inverter with gan devices for energy storage system," in *13th IEEE International Conference on Power Electronics and Drive Systems (PEDS 2019)*, 2019.

[22] D. G. B. Coblaeda, M. Vivert, R. D. Medina, F. Ruíz, D. Patiño, and G. Perilla, "A current controller for a grid-tied, cascade multilevel inverter," in *2019 IEEE Workshop on Power Electronics and Power Quality Applications (PEPQA)*, May 2019, pp. 1–5.

[23] F. L. Luo and H. Ye, "Multilevel DC/AC Inverters," in *Advanced DC/AC Inverters: Aplications in Renewable Energy*. Boca Raton, FL: CRC Press, 2013, ch. 8, pp. 137–154.

[24] P. Jana, S. Chattopadhyay, S. Maiti, P. Bajpai, and C. Chakraborty, "Hybrid Modulation Technique for Binary Asymmetrical Cascaded Multilevel Inverter for PV Application," in *International Conference on Power Electronics, Drives and Energy Systems (PEDES)*. Trivandrum. India: IEEE, 2016, pp. 1–6.

[25] S. Chattopadhyay and C. Chakraborty, "Three-phase hybrid cascaded multilevel inverter using topological modules with 1:7 ratio of asymmetry," *IEEE Journal of Emerging and Selected Topics in Power Electronics*, vol. 6, no. 4, pp. 2302–2314, Dec 2018.

[26] M. Vivert, D. Patino, and R. Diez, "Modulation strategy and controller for grid-tied trinary hybrid multilevel inverter," *IEEE Journal of Emerging and Selected Topics in Power Electronics*, pp. 1–1, 2019.

[27] D. P. Miguel Vivert, Rafael Diez, "Multicarrier modulation strategy for a trinary hybrid multilevel inverter," in *ELECTRIMACS 2017, The International Conference on Modeling and Simulation of Electric Machines, Converters and Systems*, July 2017.

[28] F. L. Liu Yu, "Trinary hybrid 81-level multilevel inverter for motor drive with zero common-mode voltage," *IEEE Transactions on Industrial Electronics*, vol. 55, no. 3, pp. 1014–1021, 2008.

[29] F. L. Luo and H. Ye, "Trinary Hybrid Multilevel Inverters," in *Advanced DC/AC Inverters: Aplications in Renewable Energy*. Boca Raton, FL: CRC Press, 2013, ch. 9, pp. 155–205.

[30] C. Rech, H. Pinheiro, H. A. Griindling, H. L. Hey, and J. R. Pinheiro, "Analysis and Comparison of Hybrid Multilevel Voltage Source Inverters," in *Power Electronics Specialists Conference. Proceedings*. IEEE, 2002, pp. 491–496.

[31] S. K. Sahoo and T. Bhattacharya, "Phase-shifted carrier-based synchronized sinusoidal pwm techniques for a cascaded h-bridge multilevel inverter," *IEEE Transactions on Power Electronics*, vol. 33, no. 1, pp. 513–524, Jan 2018.

[32] Q. Huang and A. Q. Huang, "Feedforward proportional carrier-based pwm for cascaded h-bridge pv inverter," *IEEE Journal of Emerging and Selected Topics in Power Electronics*, vol. 6, no. 4, pp. 2192–2205, Dec 2018.

[33] E. T. Renani, M. F. M. Elias, and N. A. Rahim, "Performance evaluation of multicarrier pwm methods for cascaded h-bridge multilevel inverter," in *3rd IET International Conference on Clean Energy and Technology (CEAT) 2014*, Nov 2014, pp. 1–5.

[34] Tengfei Wang and Yongqiang Zhu, "Analysis and comparison of multicarrier pwm schemes applied in h-bridge cascaded multi-level inverters," in *2010 5th IEEE Conference on Industrial Electronics and Applications*, June 2010, pp. 1379–1383.

[35] S. Arazm, H. Vahedi, and K. Al-Haddad, "Phase-shift modulation technique for 5-level packed

u-cell (puc5) inverter," in *2018 IEEE 12th International Conference on Compatibility, Power Electronics and Power Engineering (CPE-POWERENG 2018)*, April 2018, pp. 1–6.

[36] R. A. Vargas, A. Figueroa, S. E. Deleon, J. Aguayo, L. Hernandez, and M. A. Rodriguez, "Analysis of Minimum Modulation for the 9-Level Multilevel Inverter in Asymmetric Structure," *IEEE Latin America Transactions*, vol. 13, no. 9, pp. 2851–2858, 2015.

[37] A. Routray, R. Kumar Singh, and R. Mahanty, "Harmonic minimization in three-phase hybrid cascaded multilevel inverter using modified particle swarm optimization," *IEEE Transactions on Industrial Informatics*, vol. 15, no. 8, pp. 4407–4417, Aug 2019.

[38] N. Sahu and N. D. Londhe, "Optimization based selective harmonic elimination in multi-level inverters," in *2017 National Power Electronics Conference (NPEC)*, Dec 2017, pp. 325–329.

[39] S. Rao, *Engineering Optimization: Theory and Practice: Fourth Edition.* John Wiley and Sons, 6 2009.

[40] M. Ahmed, A. Sheir, and M. Orabi, "Real-time solution and implementation of selective harmonic elimination of seven-level multilevel inverter," *IEEE Journal of Emerging and Selected Topics in Power Electronics*, vol. 5, no. 4, pp. 1700–1709, Dec 2017.

[41] K. Haghdar and H. A. Shayanfar, "Selective harmonic elimination with optimal dc sources in multilevel inverters using generalized pattern search," *IEEE Transactions on Industrial Informatics*, vol. 14, no. 7, pp. 3124–3131, July 2018.

[42] J. N. Chiasson, L. M. Tolbert, K. J. McKenzie, and Zhong Du, "Elimination of harmonics in a multilevel converter using the theory of symmetric polynomials and resultants," *IEEE Transactions on Control Systems Technology*, vol. 13, no. 2, pp. 216–223, March 2005.

[43] K. Yang, Q. Zhang, R. Yuan, W. Yu, and J. Wang, "Harmonic elimination for multilevel converter with Groebner bases and symmetric polynomials," *2015 IEEE Energy Conversion Congress and Exposition, ECCE 2015*, vol. 31, no. 4, pp. 689–694, 2015.

[44] K. Yang, Q. Zhang, J. Zhang, R. Yuan, Q. Guan, W. Yu, and J. Wang, "Unified selective harmonic elimination for multilevel converters," *IEEE Transactions on Power Electronics*, vol. 32, no. 2, pp. 1579–1590, Feb 2017.

[45] D. Cox, J. Little, and D. O'Shea, *Ideals, varieties, and algorithms. An introduction to computational algebraic geometry and commutative algebra. 2nd ed*, 03 2015.

[46] H. Zhao, T. Jin, S. Wang, and L. Sun, "A real-time selective harmonic elimination based on a transient-free inner closed-loop control for cascaded multilevel inverters," *IEEE Transactions on Power Electronics*, vol. 31, no. 2, pp. 1000–1014, Feb 2016.

[47] R. Stala, "The switch-mode flying-capacitor dc–dc converters with improved natural balancing," *IEEE Transactions on Industrial Electronics*, vol. 57, no. 4, pp. 1369–1382, April 2010.

[48] E. Kolbasi and M. Seker, "Nonlinear robust backstepping control method approach for single phase inverter," in *International Conference on Methods and Models in Automation and Robotics (MMAR).* Miedzyzdroje, Poland: IEEE, 2016, pp. 954–958.

[49] R.-J. Wai, C.-Y. Lin, H.-N. Huang, and W.-C. Wu, "Design of backstepping control for high-performance inverter with stand-alone and grid-connected power-supply modes," *IET Power Electronics*, vol. 6, no. 4, pp. 752–762, 2013. [Online]. Available: http://digital-library.theiet.org/content/journals/10.1049/iet-pel.2012.0579

[50] R.-J. Wai, C.-Y. Lin, Y.-C. Huang, and Y.-R. Chang, "Design of High-Performance Stand-Alone and Grid-Connected Inverter for Distributed Generation Applications," *IEEE Transactions on Industrial Electronics*, vol. 60, no. 4, pp. 1542–1555, 2013. [Online]. Available: http://ieeexplore.ieee.org/lpdocs/epic03/wrapper.htm?arnumber=6290376

[51] M. Vivert, D. Patino, and R. Diez, "Variation of a sliding mode control applied to a trinary hybrid multilevel inverter," in *2017 IEEE 3rd Colombian Conference on Automatic Control (CCAC)*, Oct 2017, pp. 1–6.

[52] A. M. Llor and E. Solano, "Direct model-predictive control with variable commutation instant: Application to a parallel multicell converter," *IEEE Transactions on Industrial Electronics*, vol. 63, no. 8, pp. 5293–5300, Aug 2016.

[53] M. Mesbahi and M. Egerstedt, *Graph Theoretic Methods in Multiagent Networks*, ser. Princeton

Series in Applied Mathematics. Princeton University Press, vol. 1.

[54] F. Lewis, H. Zhang, K. Hengster, and A. Das, *Coopertive Control of Multiagent system*, 1st ed., ser. Communications and Control Engineering. Springer-Verlag London, vol. 1.

[55] F. Zhang, *The Schur Complement and its Applications*, ser. Numerical Methods and Algorithms. New York: Springer, 2005, vol. 4.

[56] R. A. Horn and C. R. Johnson, *The Hadamard product.* Cambridge University Press, 1991, p. 298–381.

[57] R. M. Gray, *Toeplitz and circulant matrices: a review.* Now Publishers, 2006.

[58] K. Yang, Z. Yuan, R. Yuan, W. Yu, J. Yuan, and J. Wang, "A groebner bases theory-based method for selective harmonic elimination," *IEEE Transactions on Power Electronics*, vol. 30, no. 12, pp. 6581–6592, Dec 2015.

[59] J. C. Mason and D. C. Handscomb, "Trigonometric definitions and recurrences," in *Chebyshev polynomials.* Boca Raton, FL: Chapman & Hall/Crc, 2003, ch. 1.2.

[60] J. G. Proakis and D. K. Manolakis, *Digital Signal Processing (4th Edition)*, 4th ed. Prentice Hall, 2006.